

Modeling and simulation of flash-boiling of cryogenic liquids

von der
Fakultät Energie-, Verfahrens- und Biotechnik
der Universität Stuttgart
zur Erlangung der Würde eines
Doktors der Ingenieurwissenschaften
(Dr.-Ing.) genehmigte Abhandlung

vorgelegt von
Dirk Reinhold Dietzel
aus Naumburg (Saale), Germany

Hauptberichter: Prof. Dr. Andreas Kronenburg
Mitberichter: Prof. Dr. rer. nat. Claus-Dieter Munz
Tag der mündlichen Prüfung: 19.05.2020

Institut für Technische Verbrennung
der Universität Stuttgart
2020

Erklärung

Hiermit versichere ich:

1. dass ich meine Arbeit selbständig verfasst habe,
2. dass ich keine anderen als die angegebenen Quellen benutzt und alle wörtlich oder sinngemäss aus anderen Werken übernommenen Aussagen als solche gekennzeichnet habe,
3. dass die eingereichte Arbeit weder vollständig noch in wesentlichen Teilen Gegenstand eines anderen Prüfungsverfahrens gewesen ist,
4. dass ich die Arbeit weder vollständig noch in Teilen bereits veröffentlicht habe und,
5. dass das elektronische Exemplar mit den anderen Exemplaren übereinstimmt.

Stuttgart, July 10, 2020

Dirk Dietzel

In der Thermo-Fluidodynamik ist es wie im wahren Leben:

„Es hängt alles irgendwie zusammen. Sie können sich am Hintern ein Haar ausreißen, dann trönt das Auge.“

Dettmar Cramer

Preface

Parts of this thesis have been presented at conferences and published in the archival literature. The background and theoretical developments given in chapters 3-7 have been modified with respect to the originally published texts and been significantly extended to ensure completeness, coherence and consistency of the present manuscript.

The relevant papers are:

1. D. Dietzel, T. Hitz, C.-D. Munz, A. Kronenburg, Single vapour bubble growth under flash boiling conditions using a modified HLLC Riemann solver, *International Journal of Multiphase flows*, 116:250-269, 2019.
 - Data and results discussed herein are presented in chapters 5 and 6.
 - Author's contribution: Programming (40%), data generation (100%), scientific originality (60%)
2. D. Dietzel et al., Numerical simulation of the growth and interaction of vapour bubbles in superheated liquid jets, *International Journal of Multiphase flows*, 121:103112, 2019.
 - Data and results discussed herein are presented in chapters 7.
 - Author's contribution: Programming (50%), data generation (100%), scientific originality (60%)

Acknowledgements

The present dissertation is the result of my research at the Institute of Combustion Technology at the University of Stuttgart. I would not have been able to conduct my investigations and to submit this thesis without the support of several people.

At first, I would like to thank my supervisor, Prof. Dr. Andreas Kronenburg, for giving me the opportunity to be part of his research group. He provided great support to my work throughout the entire time and his numerous critical comments helped to improve the quality of the present work. This dissertation could not have been finalised without his support and I greatly appreciate the time he spent in doing so.

In addition, I would like to acknowledge Prof. Dr. rer. nat. Claus-Dieter Munz for being the second examiner and more importantly for providing me the numerical tools that have been used for my work. He gave me the chance to directly collaborate with his research group and provided valuable input to my studies.

I would also like to thank Dr. Oliver Stein, Gregor Olenik, Niko Seubert, Gizem Inci, Satoshi Ukai, Son Vo, Gianluigi Tufano, Gregor Neuber, Carmen Straub, Milena Smiljanic, Bosen Wang, Daniel Loureiro, Jonas Kirchmann, Jan Gärtner and Marvin Sontheimer - my colleagues from ITV - for sharing this exciting time and the experiences they made with their projects. In particular, the discussions with Daniel and Jan on flash boiling, bubble dynamics and two-phase DNS always conveyed new ideas and perspectives. A great THANK YOU goes to Gianluigi for his outstanding friendship and to Son for whatever it is he calls friendship. We shared so many great moments which I will always keep in mind. Special thanks goes to Ricarda Schubert as well for her great and patient support in all organisational questions.

The collaboration with the numerical research group at the Institute of Aerodynamics and Gasdynamics of the University of Stuttgart is also gratefully acknowledged. In particular, Stefan Fechter, Timon Hitz, Fabian Föll, Matthias Sonntag and Christoph Müller helped me to understand and to use the simulation tool *Flexi*. I want to thank

Andreas Rees from the DLR in Lampoldshausen for sharing the experiences he made with flash boiling experiments.

Moreover, a huge thank you goes to our IT assistants Benedikt Heine and Felix Bühler. They were more than mere assistants. Both developed the IT infrastructure from the scratch and were always available whenever needed.

Most importantly I want to say thank you to my parents, my brother and his family for supporting me throughout the whole time and keeping me motivated. The most important thank you goes to my girlfriend Frauke. There are no words that would describe how much you supported me and how much I owe you.

Contents

Table of Contents	VII
Nomenclature	XI
Kurzfassung	XVII
Summary	XIX
1 Introduction	1
1.1 Goals of the present work	3
1.2 Thesis outline	4
2 Theoretical background	5
2.1 Thermodynamic fundamentals	5
2.1.1 Thermodynamic states of liquids and gases	5
2.1.2 Nucleation of vapour bubbles	7
2.2 Nozzle flow and liquid jets	9
2.3 Phenomenological description of flash boiling	10
2.4 Numerical simulation of flash boiling	14
2.4.1 Macroscopic models for flash boiling	14
2.4.2 Direct Numerical simulation of compressible two-phase flows	20
3 Governing equations	23
3.1 Conservation laws in the bulk phases	24
3.2 Conservation laws at the interface	25
3.3 Vaporisation model	28
3.4 Equation of state	31
3.5 Level-set equation	33
4 Numerical Approach	35
4.1 Discontinuous Galerkin spectral element method	36
4.2 Finite volume sub-cell approach	44

4.2.1	Criteria to switch between DG and FV	47
4.3	Riemann solvers	48
4.3.1	HLLC single phase Riemann solver	48
4.3.2	HLLP two phase Riemann solver	50
4.4	Time discretization	54
5	Determination of reference conditions	57
5.1	Vaporisation modeling with the HLLP Riemann solver	57
5.1.1	Setup shock tube	58
5.1.2	Results shock tube	59
5.2	Generation of a reference data base	64
5.2.1	Physical aspects of single vapour bubble growth	65
5.2.2	Reference model	65
5.2.3	Physical conditions	68
5.2.4	Results of the reference model and conclusions for the DNS of vapour bubbles	69
5.3	Numerical tests	77
5.3.1	Base case setup	78
5.3.2	Mesh resolution and time step restriction	80
5.3.3	Discretisation order and HLLP approximation at the interface	81
5.3.4	Initial condition for the vapour in the bubble	83
5.3.5	Equation of state	84
5.3.6	3D simulation of single bubble growth	86
6	DNS of single vapour bubble growth	91
6.1	Calibration of vaporisation models	91
6.1.1	Hertz-Knudsen relation	92
6.1.2	Kinetic relation and sub-grid scale heat flux	96
6.2	Prediction of model coefficients	98
6.3	Sensitivity analysis for the model coefficients and DNS results	102
7	Bubble expansion in superheated jets	105
7.1	General setup	105
7.2	Results	109
7.2.1	Setup 1, C5-120	110
7.2.2	Geometry and bubble number variation	111
7.2.3	Reference case: Setup 2, C5-120	113
7.2.4	Parameter study	117
7.3	Derivation of model equations for the LES of flash boiling jets	120
7.3.1	Limitations of the proposed SGS-model	124

8 Conclusion & Outlook	125
8.1 Conclusion	125
8.2 Outlook	127
Appendix	131
A Derivation of the Hertz-Knudsen relation and the kinetic relation	131
B Analytical equations for the HLLP Riemann solver	135
C Derivation of the Rayleigh-Plesset equation	137
D Coefficients of the different vaporisation models	141
E Dependency of c_{ent} and C_δ on initial conditions and characteristic numbers	143
F Derivation of the expansion equation for cylindrical volumes containing spherical bubbles.	147
G Data storage	149
Bibliography	153

Nomenclature

Roman Symbols

a	thermal diffusivity	$[\text{m}^2/\text{s}]$
A	surface area	$[\text{m}^2]$
A	coefficient dimensionless bubble radius	$[(\text{N}/\text{m}^2)^{1/2}]$
\mathbf{a}_i	covariant basis vector	$[-]$
\mathbf{a}^i	contravariant basis vector	$[-]$
b	NASG coefficient	$[\text{m}^3/\text{kg}]$
B	coefficient dimensionless bubble radius	$[(\text{m}^2/\text{s})^{1/2}]$
c	speed of sound	$[\text{m}/\text{s}]$
c_{ent}	entropy production coefficient	$[\text{m}^4/(\text{kg}\cdot\text{s})]$
c_p	specific heat capacity at constant pressure	$[\text{J}/(\text{kg}\cdot\text{K})]$
c_v	specific heat capacity at constant volume	$[\text{J}/(\text{kg}\cdot\text{K})]$
C_δ	coefficient of the SHFM	$[-]$
C_v	NASG coefficient	$[\text{J}/(\text{kg}\cdot\text{K})]$
CFL	Courant-Friedrichs-Lewy number	$[-]$
D_{bub}	bubble distance	$[\text{m}]$
DFL	diffusive CFL number	$[-]$
e	specific internal energy	$[\text{J}/\text{kg}]$
E	specific total energy	$[\text{J}/\text{kg}]$
E_{tot}	total energy	$[\text{J}]$
\mathcal{E}	reference element	$[-]$
\mathbf{F}	physical flux vector	$[\text{J}/\text{kg}]$
\mathcal{F}	reference flux vector	$[\text{J}/\text{kg}]$
h	specific enthalpy	$[\text{J}/\text{kg}]$
h_{fg}	specific latent heat	$[\text{J}/\text{kg}]$
\mathcal{I}	indicator DG-FV switching	$[-]$
\mathcal{J}	Jacobian determinate	$[-]$
Ja	Jakob number	$[-]$
k	heat conductivity	$[\text{W}/(\text{m}\cdot\text{K})]$

l	Lagrange polynomial	[-]
L	length scale	[m]
m	mass	[kg]
m_{tot}	total mass	[kg]
\dot{m}''	mass flux	[kg/(m ² ·s)]
M	molar mass	[kg/mol]
\mathbf{n}_{int}	interface normal vector	[-]
N	polynomial degree	[-]
N_{bub}	number of bubbles	[-]
p	pressure	[Pa]
P_{∞}	NASG coefficient	[Pa]
q	heat flux	[W/m ²]
\tilde{q}	NASG coefficient	[J/kg]
\tilde{q}'	NASG coefficient	[Pa ^{$\gamma-1$}]
r	radial coordinate	[m]
R	bubble radius	[m]
R^*	normalised bubble radius	[-]
R^+	dimensionless bubble radius	[-]
R_{crit}	critical radius	[m]
R_p	superheat ratio	[-]
\mathcal{R}	specific gas constant	[J/(kg·K)]
\mathcal{R}_g	general gas constant	[J/(mol·K)]
s	specific entropy	[J/(kg·K)]
S	signal velocity	[m/s]
\mathbf{S}	source term vector	[-]
t	time	[s]
t^+	dimensionless time	[-]
T	temperature	[K]
$\mathbf{u} = (u, v, w)^T$	velocity	[m/s]
\mathbf{U}	vector of conservative variables	[-]
v	specific volume	[m ³ /kg]
\mathbf{v}	vector of primitive variables	[-]
V	volume	[m ³]
$\mathbf{x} = (x_1, x_2, x_3)^T$	Cartesian coordinate vector	[m]
\mathcal{X}	mass fraction in HRM	[-]
Y	volume fraction in Σ - Y -model	[-]

Greek Symbols

α	volume fraction	[-]
γ	NASG coefficient	[-]
δ	boundary layer thickness	[m]
$\delta_{i,j}$	Kronecker delta	[-]
ϕ	level-set	[-]
κ	curvature	[1/m]
$\lambda_{\text{vap}}, \lambda_{\text{cond}}$	coefficients in the HKR	[-]
μ	dynamic viscosity	[Pa·s]
ρ	density	[kg/m ³]
σ	surface tension coefficient	[N/m]
Σ	surface density	[m ² /m ³]
τ	viscous stress tensor	[Pa]
Θ	relaxation time in HRM	[s]
ψ	DG basis function	[-]
Ψ_{bub}	dimensionless bubble distance	[-]
Ψ_{buffer}	size factor buffer zone	[-]
$\xi = (\xi^1, \xi^2, \xi^3)^T$	reference coordinate vector	[m]

Superscripts

L, R	left and right state of Riemann problem
$(\dot{\cdot})$	first time derivative
$(\ddot{\cdot})$	second time derivative
$(\widetilde{\cdot})$	auxilliary variable

Subscripts

bub	bubble
buf	buffer zone
dom	domain
i, j, k, l	indices for space directions
int	interface
liq	liquid
LS	level-set
sat	saturation conditions
vap	vapour
0	initial conditions
∞	ambient conditions

Acronyms

CFD	Computational Fluid Dynamics
DG	discontinuous Galerkin
DGSEM	discontinuous Galerkin spectral element method
DLR	Deutsches Zentrum für Luft- und Raumfahrt (German Aerospace Centre)
DNS	direct numerical simulation
EOS	equation of state
FV	finite-volume
HKR	Hertz-Knudsen relation
HLLC	Harten-Lax-van-Leer contact discontinuity
HLLP	Harten-Lax-van-Leer phase transition
HRM	Homogeneous relaxation model
KR	kinetic relation
LES	large-eddy simulation
LOX	liquid oxygen
NASG	Noble-Abel stiffened gas
OMS	orbital maneuvering system
RCS	reaction control system
RPE	Rayleigh-Plesset equation
SHFM	sub-grid heat flux model

Kurzfassung

Toxische Treibstoffe in Lageregeltriebwerken werden zukünftig durch umweltfreundliche Alternativen ersetzt. Flüssigsauerstoff (LOX, von engl. Liquid Oxygen) kann als Oxidator verwendet werden, aber die vakuum-nahen Bedingungen des Weltalls führen zu einer schnellen Expansion in einen überhitzten Zustand wenn LOX in die Brennkammer gespritzt wird. Der Zerfall des Flüssigstrahls durch die resultierende Nukleation und das Wachstum von Dampfblasen wird Flashverdampfung genannt. Die relevanten Prozesse treten typischerweise bei kleinen Längen- und Zeitskalen auf und müssen in makroskopischen Strömungssimulationen der gesamten Brennkammer modelliert werden. Die Eigenschaften des erzeugten Sprays hängen sowohl von den Blaseninteraktionen als auch von der Strömungsform in der Einspritzdüse und im Jet stark ab. Die aktuellen Modelle zur Beschreibung der Flashverdampfung berücksichtigen diese Effekte nicht explizit. Das am häufigsten verwendete Modell ist das Homogeneous Relaxation Modell (HRM). Eine zusätzliche Erhaltungsgleichung beschreibt den Massenbruch der Dampfphase und der Phasenwechsel wird als Relaxation der überhitzten Flüssigkeit in den Sättigungszustand modelliert. Durch die Dampfentstehung kommt es zur für Flashverdampfung typischen schnellen Strahlexpansion. Alternativ kann das Spray auch mit einem Euler-Lagrange-Ansatz modelliert werden, bei dem die Tropfen als Massepunkte betrachtet werden. Dabei müssen alle relevanten Sprayeigenschaften, wie Tropfengrößen- und Geschwindigkeitsverteilungen, vorab bekannt sein. Beide Simulationsstrategien liefern keine Information über Blasendichten und -größen. Mit Hilfe detaillierterer Modelle (z.B. Zweigleichungsmodelle) können diese Eigenschaften abgeleitet und damit der Informationsgehalt makroskopischer Simulationen erhöht werden. Die erforderlichen Schließungsbedingungen müssen die räumlich und zeitlich nicht aufgelöste Blasenexpansion im Strahlkern modellieren. Das Hauptziel der vorliegenden Arbeit ist deshalb eine Quantifizierung der Wachstumsraten und der Interaktion von Dampfblasen, die zur Entwicklung der Feinstrukturmodelle z.B. in Zweigleichungsmodellen verwendet werden können. Die zugrundeliegenden Prozesse können mit direkten numerischen Simulationen (DNS) analysiert werden, wenn der Strömungslöser Phasenwechsel bei extremen Umgebungsbedingungen erfassen kann. In dieser Arbeit wird ein voll-kompressibler Code verwendet, der die diskontinuierliche Galerkin-Methode zur räumlichen Diskretisierung

der Erhaltungsgleichungen verwendet. Die Level-set-Methode erfasst die Phasengrenze und Riemann-Löser bestimmen die numerischen Flussfunktionen zwischen benachbarten Rechenzellen.

Im ersten Teil der Arbeit werden Schließungsbedingungen für die Modellierung der Verdampfungsmassenflüsse im Hinblick auf das Blasenwachstum beurteilt. Das Wachstum einer einzelnen Blase dient als Referenzfall für die Kalibrierung der Verdampfungsmodelle und die Validierung des DNS-Lösers. Drei verschiedene Verdampfungsmodelle werden verglichen. Die Herz-Knudsen-Relation und eine kinetische Relation sagen die Volumenexpansion einzelner Blasen gut voraus, können aber den zeitlichen Verlauf des Massenflusses nicht widerspiegeln. Ein Feinstrukturmodell für den Wärmestrom liefert qualitativ bessere Ergebnisse für den Massenfluss, aber die volumetrische Expansion stimmt nur am Ende der Simulation mit der Referenzlösung überein. Die Abhängigkeit der Modellkoeffizienten von den physikalischen Bedingungen ist für die verschiedenen Verdampfungsmodelle ähnlich.

Im zweiten Teil der Arbeit wurden DNS von Blasengruppen durchgeführt und die resultierenden Wachstumsraten mit den Standardmodellen für Einzelblasenwachstum verglichen. Die Berechnungen zeigen, dass Dampfblasen im inneren des Strahls langsamer wachsen als an der Oberfläche. Die Blasenradien fallen mit zunehmendem Abstand von der Strahloberfläche ab. Das Wachstum im Strahlkern ist um 70% reduziert und hat damit einen vernachlässigbaren Einfluss auf die Gesamtexpansion. Das reduzierte Wachstum ist eine Folge der wechselwirkenden Druckfelder um benachbarte Blasen. Die Ergebnisse sind in einem weiten Parameterbereich qualitativ vergleichbar und eine empirische Gleichung wird vorgeschlagen, die die lokalen Blasenwachstumsraten als Funktion des lokalen Drucks abschätzt.

Summary

Toxic propellants used in orbital manoeuvring systems are to be replaced by environmentally less harmful alternatives. Liquid oxygen (LOX) can be used as oxidizer but the near vacuum conditions of outer space lead to a fast expansion into a superheated state when LOX is injected into the combustion chamber. The disintegration of the liquid jet is driven by bubble nucleation and growth, which is - under given conditions - called flash boiling. These processes typically occur at small length and time scales and need to be modelled in macroscopic simulations of the entire combustion chamber. The properties of the generated spray strongly depend on the dynamics of the interacting bubbles as well as the flow patterns in the nozzle and in the jet. The state-of-the-art models for flash boiling do not explicitly account for these effects. The most commonly used model in the context of Euler-Euler simulations is the homogeneous relaxation model (HRM). An additional transport equation represents the vapour mass fraction and the phase transition is modeled as a relaxation of the superheated liquid to saturation conditions. The vapour generation yields the fast expansion typical for flash boiling jets. Alternatively, the spray can be modeled with an Euler-Lagrange simulation directly accounting for the droplets as point mass. Here, all relevant properties such as droplet sizes and velocity distributions have to be known a priori. In both simulation strategies information on bubble densities and bubble sizes is not available. With the aid of more detailed models (e.g. two equation models) these properties can be derived increasing the data content of macroscopic simulations. The required closure conditions need to model the spatially and temporally unresolved bubble expansion in the jet core. Therefore, the main objective of the present work is a quantification of bubble growth rates and bubble-bubble interactions that can be used to develop sub-models e.g. for two equation models. Direct numerical simulations (DNS) can be used to analyse the underlying processes if the solver handles phase transition effects at extreme ambient conditions. This work uses a fully compressible discontinuous Galerkin solver for space discretisation. The level-set method captures the phase interface and Riemann solvers determine the numerical fluxes between adjacent computational cells.

In the first part of the work closure conditions for the mass transfer models are

assessed with respect to vapour bubble growth. The growth of isolated bubbles serves as a reference case to calibrate the vaporisation models and to validate the DNS solver. Three different vaporisation models are compared. The Hertz-Knudsen relation and a kinetic relation predict the volumetric expansion of a single bubble well but cannot represent the instantaneous mass flux. A sub-grid scale heat flux model predicts the mass flux qualitatively better but the volumetric bubble expansion matches only at late time intervals. The dependency of the calibrated coefficients on the physical conditions is similar for the different vaporisation models.

In the second part, DNS of bubble clusters are conducted and the resulting growth rates are compared to the standard models for single bubble growth. The computations show that vapour bubbles grow more slowly in the center of a jet than at its surface. The bubble radii exponentially decrease with distance from the liquid jet interface and growth rates are reduced by more than 70% in the centre of the jet such that their volumetric growth can be neglected for the computation of the jet expansion. The reduced growth can be associated with the interactions of the pressure fields surrounding the bubbles as the liquid pressure increases due to bubble growth and vaporisation. The degree of superheat is locally reduced and bubbles grow at a smaller rate. The results are qualitatively comparable across a wide parameter range and an empirical correlation is derived estimating the local growth rates based on the local pressure field.

CHAPTER 1

Introduction

In the digital era earth orbiting satellites affect the daily life of most people to a great extent. Mobile internet coverage, television signals, navigation and weather forecast are only few examples for the use of orbit satellites [75]. Starting in 1957 the number of satellite launches continuously increased. Following the database of the Union of Concerned Scientists (UCS) a total number of 1886 satellites are currently operating in the earth orbit [1], 389 of them launched in 2017 [2]. Important components of all satellites are the reaction control system (RCS) and the orbital maneuvering system (OMS) responsible for attitude control, reboost or re-entrance into the atmosphere [108]. Depending on the demands to total thrust and life time different types of thruster can be used as RCS or OMS. One thruster type relies on chemical propulsion where the exhaust gases of a combustion process provide the necessary impulse to the space device. Hypergolic substances are popular propellants because fuel and oxidizer spontaneously react and burn at a high rate. The thruster does therefore not require an ignition system reducing its weight and complexity. However, hypergolic propellants are toxic resulting in high ground handling costs and environmental hazards. For this reason current research focusses on the replacement of fuel and oxidizer by environmentally more friendly alternatives [67]. One possible combination is gaseous methane and liquid oxygen (LOX). Besides the nontoxicity the high specific impulse performance I_{sp} is beneficial [67]. However, using LOX as the oxidizer yields challenges in the design of the injection system and the control of the combustion in the chamber: The cryogenic oxygen is still liquid when it is injected into the combustion chamber, the disintegration of the LOX jet controls the mixture with the fuel and determines the prospects of successful ignition events. Satellite thrusters operate under the near vacuum conditions of outer space. The pressure in the combustion chamber will be

below the saturation pressure of the LOX causing a spontaneous phase transition from liquid to vapour. This process is called *flash boiling* and it controls the disintegration of the LOX jet and its break-up into small droplets. Designing the injection system of a satellite thruster with an efficient and well-defined combustion requires a precise prediction of the spray properties (droplet size distribution, velocity fields, penetration depth). However, universal models for flash boiling do not exist because it depends on a variety of parameters and the involved physical processes interact in multiple ways. Several flash boiling regimes exist and the characteristic properties of the generated sprays vary significantly. The development of injection systems which optimally exploit the advantages of flash boiling in the spray generation process is therefore extremely difficult.

Computational Fluid Dynamics (CFD) can aid the design process but the requirements to the flow solver are high. The major aspects of flash boiling are the nucleation and the growth of vapour bubbles [102]. The change from liquid to vapour results in a strong expansion because the ratio between liquid density and vapour density is typically high. The jet volume strongly increases and the liquid core will burst once the vapour bubbles merge [103]. Despite the ever-increasing computational resources a full resolution of all these processes on an industrial scale will not be possible in the near future. Lamanna et al. [58] conducted experiments on flash boiling of LOX jets and the test conditions at 113 K illustrate the challenges for the computation: The radius of the smallest bubbles at these conditions is of the order of 20 nm. If a bubble is initially resolved with ten cells across its diameter, 250.000^3 cells are required to discretize a cube of 1 mm^3 with an equidistant mesh. Even with mesh stretching or adaptive mesh refinement strategies a simulation of the entire combustion chamber of a satellite thruster is unfeasible and suitable models for the unresolved dynamics of vapour bubbles are to be found. Models for single bubble growth exist [80, 81, 85] but they are not necessarily applicable to cases where multiple bubbles can interact. This was, e.g., observed by Kitamura et al. [53]. They defined a criteria for the onset of flashing based on bubble growth rates but they found that measured growth rates deviate from the theoretical growth rates. Therefore, a better understanding and a quantification of bubble interaction effects can improve the existing models.

1.1 Goals of the present work

This work is part of the Collaborative Research Centre SFB-TRR 75 „Droplet Dynamics Under Extreme Ambient Conditions“ of the German Research Foundation. Within one of the sub-projects the German Aerospace Centre (DLR) in Lampoldshausen is conducting experiments on LOX jets under flash boiling conditions. The present work is part of the numerical partner project. The mid-term goal of the numerical investigation is the simulation of flash boiling with the aid of large-eddy simulations (LES). An LES of flash boiling requires, however, suitable sub-scale models that account for the expansion of the vapour bubbles. Therefore, the main goal of the present thesis is a quantification of the bubble-bubble interactions in superheated LOX jets. For this purpose direct numerical simulations (DNS) of the vapour bubble growth in the jet are conducted. This configuration inherently requires a flow solver which is able to treat two-phase flows and phase change. Moreover, compressibility can affect flash boiling and needs to be taken into account for the computation. This yields the following objectives for the present investigation:

1. *The assessment of simulation strategies for the DNS of vapour bubbles with a fully compressible solver.* The simulation of single bubble growth serves as a reference case for the code validation. The sensitivity of the DNS to numerical parameters is investigated. Two different equations of state and three vaporisation models are evaluated. The parameters of the vaporisation models are calibrated comparing the growth rates to analytical models for bubble growth using several physical conditions.
2. *Design and assessment of suitable simulation setups.* The previous section discussed the computational demands for the simulation of bubble growth in liquid jets. The use of simplified geometries and generic configurations reduces the computational cost. These geometries need to capture the essential physical aspects and allow to cover a wide parameter range. Therefore the influence of the computational domain on the resulting bubble growth rates is compared for three different setups with an increasing level of detail.
3. *Quantification of expansion rates of multiple interacting bubbles.* One geometrical setup is used to quantify bubble growth rates for a wide range of physical parameters. Thereby, the deviation to the single bubble solution is evaluated as functions of the distance to the jet surface and of the local pressure. Finally, these results are used to suggest an alternative model for flash boiling jets.

1.2 Thesis outline

Chapter 2 provides the theoretical background including fundamental thermodynamic and fluidmechanical aspects, a literature survey on flash boiling along with a phenomenological description of the underlying processes. Moreover, Ch. 2 summarises the state-of-the-art simulation strategies for flash boiling and for compressible two-phase flows with phase transition. The governing equations as well as the physical models used for the present computations are discussed in Ch. 3 and the numerical methods are introduced in Ch 4. Chapter 5 contains results from case studies using simple geometries. They are important to analyse fundamental characteristics of the flow solver and to define the reference conditions of the investigation. Firstly, the properties of compressible two-phase flows are discussed using the example of a half-open shock tube. Secondly, a semi-analytical model is used to investigate the growth of single spherical bubbles and to quantify the growth rates for the present operating conditions. This reference solution is used to validate the numerical solver in the last section of Ch. 5. A detailed investigation of possible closure conditions for the vaporisation modeling in the DNS of single bubbles follows in Ch. 6 and the findings are used to analyse the growth of multiple interacting bubbles with the aid of DNS in Ch. 7. The thesis is concluded with a summary on the conducted work and an outlook on future research goals in Ch. 8.

CHAPTER 2

Theoretical background

The present work deals with the physical phenomenon called flash boiling, its modeling and simulation. The term *boiling* indicates that at least two distinct phases are involved – a liquid phase and its vapour – where the liquid undergoes a phase transition. Section 2.1 summarises the thermodynamic fundamentals which characterise the processes involved in flash boiling. Section 2.2 describes some important aspects of nozzle flows and jet break-up. On the basis of these theories and by reviewing experimental observations Sec. 2.3 describes flash boiling phenomenologically. Section 2.4 presents the state-of-the-art models for the macroscopic simulation of flash boiling and deduces the simulation strategy for the present work.

2.1 Thermodynamic fundamentals

2.1.1 Thermodynamic states of liquids and gases

Several properties characterise the thermodynamic state of a fluid. Important thermodynamic state variables are the pressure p and the temperature T . They define the ambient conditions of a thermodynamic system and allow to determine further state variables from equations of state (EOS) [7]. Generally, only two state variables might be set independently and all other properties are coupled by the EOS. The thermal EOS correlates p and T with the density ρ or the specific volume $v = 1/\rho$. Phase diagrams help to assign the thermodynamic state of a substance to certain regimes. Figure 2.1(a) depicts a schematic p - v -diagram. The saturation curve is shown in red with the liquid saturation line on the left and the vapour saturation line on the right. The area below the saturation curve represents the two-phase mixture generated when the liquid vaporises. Stable subcooled liquid and stable

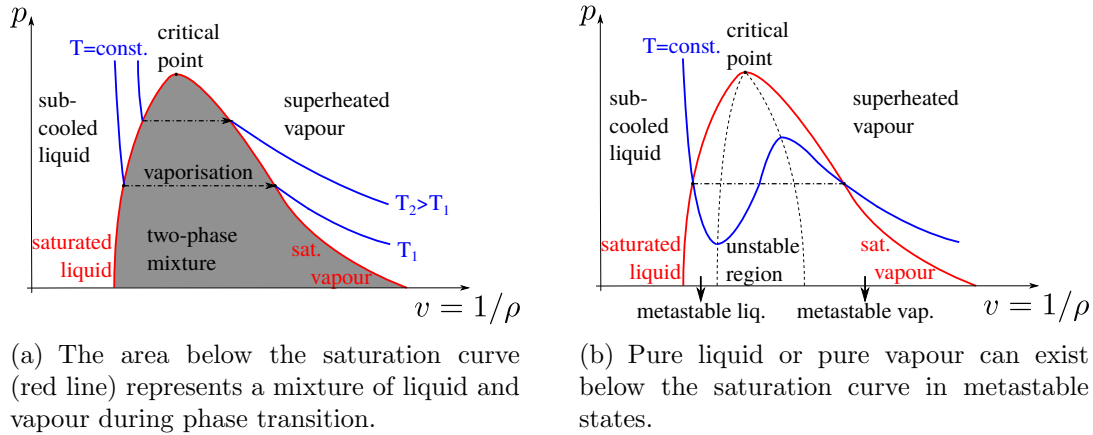


Figure 2.1: Vapour pressure diagram for different regimes.

superheated vapour exist on the left and right side of the saturation curve, respectively. The saturation temperature $T_{\text{sat}} = f(p)$ or equivalently the saturation pressure $p_{\text{sat}} = g(T)$ define the saturation curve and represent the threshold for the onset of a phase transition. The two-phase zone in Fig. 2.1(a) represents a mixture of boiling saturated liquid and saturated vapour.

The specific internal energy e is another important state variable and describes the energy of a quiescent fluid without potential energy [7]. For a given pressure and temperature a caloric EOS determines the internal energy e according to a certain reference state. The absolute value of e depends on the choice of this reference point and only changes in e can be determined exactly. The specific enthalpy h was introduced for the description of open systems and it is defined by

$$h = e + pv. \quad (2.1)$$

When the thermodynamic state of a fluid changes during an open flow process the change in the term pv accounts for the volume work [7]. If the boiling liquid and the saturated vapour of a two-phase system share the same temperature and pressure, the system is in thermodynamic equilibrium. The specific enthalpy h is thereby higher in the vapour than in the liquid. This difference is called the latent heat of vaporisation and it is defined by

$$h_{\text{fg}} = h_{\text{vap}} - h_{\text{liq}}. \quad (2.2)$$

The vaporisation of a liquid needs an energy supply allowing for the enthalpy rise

and increasing the total energy of the vaporised fluid. In technological processes the energy is supplied, e.g., in form of heat. During the vaporisation the temperature is then constant because the supplied heat solely increases the enthalpy (see the dash-dotted arrows in Fig. 2.1(a)).

Under certain conditions a pure liquid or a pure vapour state can be found below the saturation curve. These states are then called metastable because they seek a phase transition for returning into stable conditions. Figure 2.1(b) shows a corresponding phase diagram. The metastable states are enclosed by the saturation and spinodal lines (dashed black lines). The spinodals define the limit for the maximum superheat and subcooling on the liquid and vapour sides, respectively. The area enclosed by the spinodals represents thermodynamic unstable states which cannot exist. Vaporisation of a superheated liquid may also occur without a further external energy supply. The increase of the enthalpy when the liquid becomes gaseous results in a cooling of the remaining liquid. Thereby, the superheated liquid relaxes to a stable saturated state. If no heat is supplied from external sources vaporisation continues until the remaining liquid has cooled down to saturation conditions.

2.1.2 Nucleation of vapour bubbles

The previous section discussed the vaporisation from a macroscopic point of view. The liquid and the vapour are considered as a homogeneous two-phase mixture (Fig. 2.1(a)) or as homogeneous individual phases (Fig. 2.1(b)) with phase transition being a global process. On a microscopic level vaporisation occurs locally at the interface between liquid and vapour. Here, not only the interfaces inherently defined by the geometrical configuration are important. In the context of vaporisation, the formation of new interfaces by bubble nucleation is a crucial aspect because it increases the total interface area and therefore allows for higher total vaporisation rates.

The nucleation describes the formation of the first stable vapour bubbles within the liquid. In the present work the two-phase system is regarded in the sense of Fig. 2.1(b). If the liquid lies within the metastable range it is in tension [14]. This tension is defined as the pressure difference Δp_{liq} between the saturation pressure at the local liquid temperature $p_{\text{sat}}(T)$ and the local liquid pressure p_{liq} . It can rupture the liquid to form finite vapour voids [14]. Homogeneous and heterogeneous nucleation

are two regimes characterising the formation of bubbles. Homogeneous nucleation occurs within the bulk liquid as a result of stochastic fluctuations associated with the thermal motion of the molecules. Heterogeneous nucleation instead occurs at small inclusions. This can be gas impurities at a solid wall, dissolved gas or particles. Heterogeneous nucleation typically occurs at smaller Δp_{liq} and is more relevant in engineering applications. However, flash boiling may also be determined by homogeneous nucleation as will be discussed in Sec. 2.3. For the physical description of vaporisation processes two important aspects within the nucleation theory are the nucleation rate and the properties of the stable bubbles. The nucleation rate determines the number of stable bubbles generated per unit time and unit volume and therefore the bubble number density after a certain time interval. There is no model equation that is universally valid, depending on the theory the estimated nucleation rates in the literature may vary considerably and the present work uses the nucleation rates as a free parameter. Therefore, the different nucleation theories and possible model equations are not detailed further within this chapter. The reader is referred to the work of Blander and Katz [13], Oxtoby [72] or Brennen [14] for further theories. In contrast, the properties of the stable bubble nuclei are important for the present work because they define the initial conditions of the simulation. Common assumptions are that the liquid and the vapour are in mechanical and thermodynamic equilibrium. Mechanical equilibrium exists if the surface tension force balances the pressure difference between liquid and vapour such that

$$\frac{2\sigma}{R} = p_{\text{vap}} - p_{\text{liq}}, \quad (2.3)$$

holds. Here, σ and R are the surface tension coefficient and the bubble radius, respectively. The liquid pressure is equal to the ambient pressure p_{∞} . In thermodynamic equilibrium the liquid and the vapour share the same temperature and the same chemical potential, respectively, viz. $T_{\text{liq}} = T_{\text{vap}} = T_{\infty}$ and $\mu_{\text{ch,liq}} = \mu_{\text{ch,vap}}$. Carey [16] used these conditions and the Gibbs-Duhem equation to obtain the pressure of the vapour in the bubble:

$$p_{\text{vap}} = p_{\text{sat}}(T_{\infty}) \exp\left(\frac{v_{\text{liq}}(p_{\text{liq}} - p_{\text{sat}}(T_{\infty}))}{RT_{\infty}}\right). \quad (2.4)$$

This pressure is smaller than the saturation pressure at the ambient temperature. In a p - v -diagram as given by Fig. 2.1(b) the resulting state can be assigned to the right of the saturation curve in the superheated vapour range. Inserting Eq. (2.4) into Eq. (2.3) gives the initial radius of a nucleated bubble. The pressure in the

bubble is often simplified to $p_{\text{vap}} = p_{\text{sat}}(T_{\infty})$ and this simplification is also used in the remainder of this work. These conditions are further discussed in Sec. 5.2.1.

2.2 Nozzle flow and liquid jets

The following section describes the injection of a liquid into a gaseous atmosphere. A large body of literature exists and the following theory is mainly based on the book chapter of Fritsching in the Multiphase Flow Handbook by Crowe [38]. Figure 2.2 shows the general setup with the liquid tank on the left and the injection chamber on the right side. The tank pressure is higher than the chamber pressure pushing the liquid through the nozzle into the chamber. Given that there is no phase transition the liquid pressure drops along the nozzle and it will be equal to the chamber pressure at the orifice. When the liquid exits the nozzle it generates a free surface to the gaseous atmosphere and it is called a liquid jet. Interactions between the jet and the gas phase trigger instabilities, the surface deforms and ligaments and droplets separate from the jet volume. This process is called primary jet atomisation. The secondary atomisation describes the break-up of ligaments and larger droplets into smaller droplets. Characteristic properties of this jet disintegration are the length of the liquid core, the spreading angle of the generated spray as well as the size and the velocity distribution of the liquid droplets. In the field of spray combustion different factors matter. It is generally intended to have a fast vaporisation and mixing of the fuel with the oxidizer because it enhances the combustion efficiency and avoids pockets of rich mixtures leading to incomplete combustion. On the one hand, a large spray angle indicates fast disintegration of the liquid jet into small droplets with a good mixture formation. Smaller droplets, in turn, facilitate a fast vaporisation because the surface-to-volume ratio is higher.

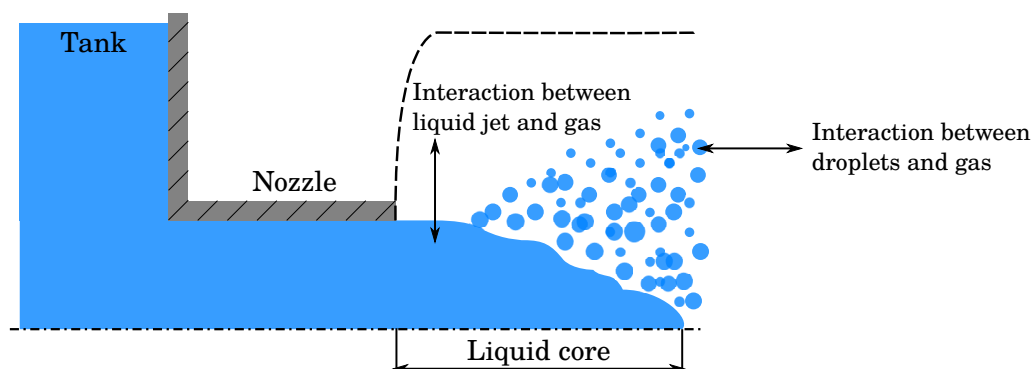


Figure 2.2: Principal sketch for liquid jets injected into gas atmosphere.

On the other hand, liquid droplets may impinge on the walls of the injection chamber where they form films and decrease the combustion efficiency. For similar reasons the length of the liquid core is important. With an increasing length of the liquid core, the likelihood of droplet impact on the chamber wall in axial direction increases. Moreover, a long liquid core indicates poor jet disintegration with fewer but larger droplets. The droplet sizes vary for one certain configuration. The average droplet diameter is characterised by the Sauter mean diameter (SMD). In the absence of phase transition inertial forces, friction and surface tension control the jet break-up. Different regimes exist depending on the ratio of these mechanical forces summarised by the Reynolds number Re , Weber number We and Ohnesorge number Oh . Further details on the mechanical jet break-up are found in the relevant literature [38, 95]. They are not further discussed here because they are of minor interest for the present computations.

2.3 Phenomenological description of flash boiling

Phase change introduces additional aspects to the jet atomisation. If the liquid temperature exceeds the saturation temperature for the local pressure the liquid vaporises. A sudden pressure drop may superheat the liquid below the saturation pressure. In this case the phase transfer rates are typically higher than compared to vaporisation at saturation conditions by an external heat supply. The enhanced phase transition of a superheated liquid is called flash boiling. Figure 2.3 depicts the simplified setup and outlines some of the key aspects of flash boiling jets with respect to the theories of Secs. 2.1 and 2.2. A storage tank contains a subcooled liquid at the injection pressure p_0 (state A). The liquid passes the nozzle and the pressure drops to the ambient pressure p_∞ . If p_∞ is smaller than the saturation pressure at the ambient temperature $p_{\text{sat}}(T_\infty)$ the liquid becomes superheated (state B, see Sec. 2.1.1) and vapour bubbles will spontaneously nucleate (state C, see Sec. 2.1.2) [102]. The low pressure conditions in the expansion chamber (state D) allow bubbles to grow, the liquid jet will strongly expand and break up into droplets once the bubbles merge [103]. The superheat ratio

$$R_p = \frac{p_{\text{sat}}(T_\infty)}{p_\infty} \quad (2.5)$$

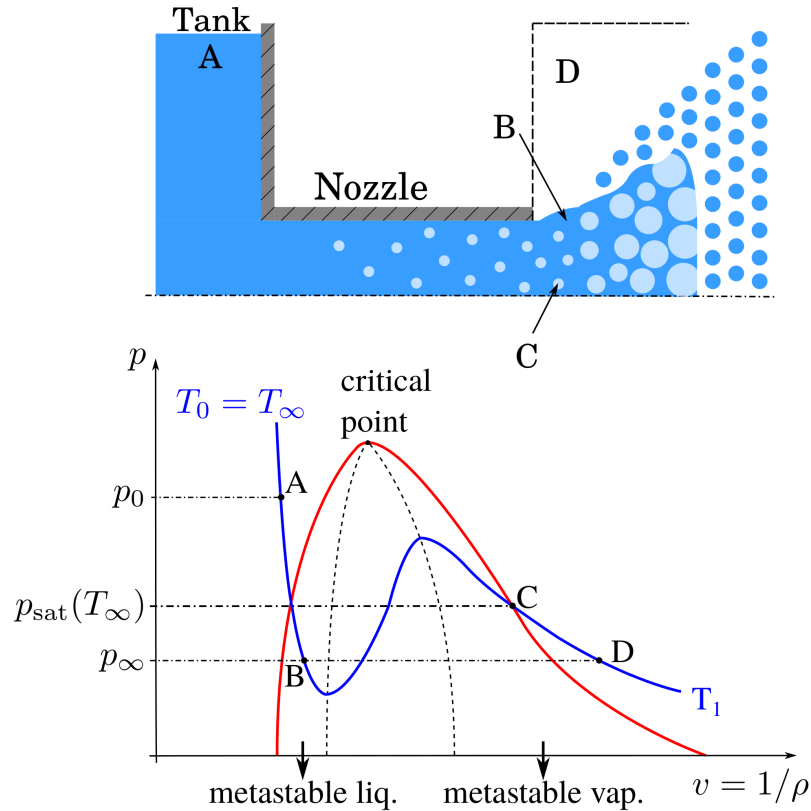


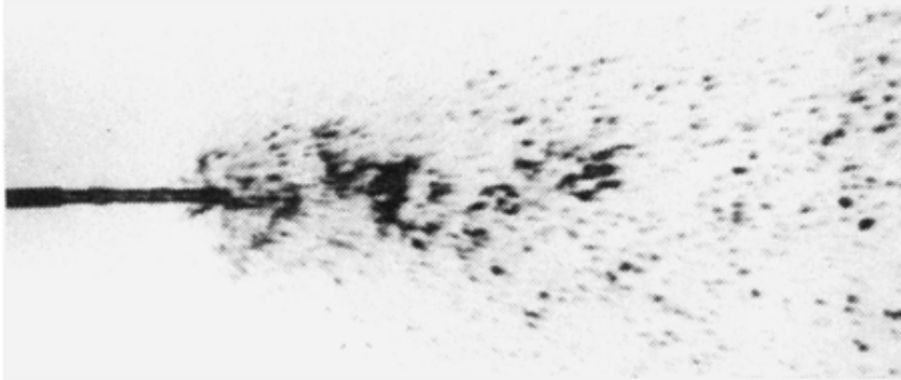
Figure 2.3: Simplified setup for a flash boiling jet. A sub-cooled liquid (state A) will be injected into a low-pressure environment (state D). The liquid will expand to a superheated state B allowing for spontaneous bubble nucleation at state C.

measures the deviation of the superheated liquid to its saturation state. Compared to mechanical jet break-up droplet sizes are typically smaller and spray angles are larger. The droplet vaporisation improves resulting in a more stable ignition within a combustion chamber [102]. However, the characteristics of the spray generated by flash boiling, such as droplet sizes, spray angle and penetration length, are difficult to predict due to the complex interactions of the parameters involved. The essential physical quantities controlling the spray generation are the nucleation rate and the bubble growth rate [8, 102]. They depend on a variety of parameters and a great effort has been spent on the experimental investigation of flash boiling in order to identify different regimes and the underlying mechanisms.

Oza [73] classified flash boiling into an internal and an external mode. While appreciable bubble nucleation and growth within the nozzle characterises internal flash boiling, pure liquid exits the orifice in the case of external flash boiling. Brown and York [15] conducted one of the pioneering studies. They investigated the



(a) Mechanical break-up [53].



(b) Flash boiling [53].

Figure 2.4: Photographies of the jet disintegration of water jets for different regimes taken from Kitamura et al. [53].

spray pattern for cylindrical water and Freon-11 jets using different nozzle types and ambient temperatures. They considered heated liquids for an atmospheric back pressure. Kitamura et al. used water and ethanol and extended the pressure range approaching vacuum conditions [53]. Both studies show that the traditional classification of the spray break-up based on the mechanical forces does not hold for jets at a sufficiently high superheat. Figures 2.4(a) and 2.4(b) depict photographs from Kitamura et al. [53] of mechanical jet break-up and external flash boiling, respectively. While the subcooled jet breaks up only far downstream a violent disintegration was observed further upstream for the superheated jet. Brown and York [15] as well as Kitamura et al. [53] analysed the sensitivity of the axial location where flashing occurs to different parameters. With increasing degree of superheat the break-up point moves upstream and shattering of the jet enhances. Both studies suggest that flash boiling requires a minimum degree of superheat. Increasing mechanically induced disturbances permit bubble nucleation at lower superheats and reduce the minimum required superheat level. The liquid jet in Fig. 2.4(b) exits the nozzle undisturbed and spontaneously flashes further downstream. The delay time is associated with the time bubbles need to nucleate and grow to a certain size. The faster the nucleation and growth process happens the further upstream the jet disintegrates. A disintegration in close vicinity to the nozzle

is typically associated to the internal flashing mode [53, 73]. On the one hand, Oza [73] suggests that disintegration directly at the nozzle orifice is a result of strong vapour generation within the nozzle. On the other hand, the photographs of Reitz [87] show a liquid core even if the jet surface bursts at the nozzle exit. Therefore, Park and Lee introduced a sub-classification of the internal flashing mode depending on the two-phase flow pattern within the nozzle [74]. In case of a bubbly flow the liquid carrier phase exits the nozzle with an intact core because bubbles are generated first at the nozzle wall. This mode supports the results of Reitz [87]. With an increasing degree of superheat the nozzle flow changes from bubbly flow to slug flow and further to annular flow. The length of the intact core reduces from bubbly flow to slug flow. For annular flow only a thin liquid film exits the nozzle and directly ruptures into ligaments and droplets after the orifice. The annular flow type supports the observations of Oza [73]. Further nozzle flow patterns are discussed by Sher [102]. A complete atomisation within the nozzle generates a fully flashing spray with a highly dispersed droplet cloud [59]. In this case, nucleation rates are high enough to solely control the disintegration of the liquid into droplets. Figure 2.5 summaries the different regimes of flash boiling according to experimental findings. Numerous other experiments on flash boiling considering different fluids (pure liquids and mixtures), a variety of nozzle geometries and materials, different temperatures and flow velocities as well as chamber and injection pressures were conducted [40, 42, 58, 103, 110, 118] which confirm the general trends discussed here. At the same time a general model treatment which covers the different regimes of flash boiling is not yet found due to the complexity of the interacting effects.

The review of experimental studies identifies the major parameters in flash boiling and their influence on the generated sprays:

1. Liquid temperature T_{liq} : For a fixed ambient pressure the liquid temperature determines the degree of superheat. A temperature rise increases bubble nu-

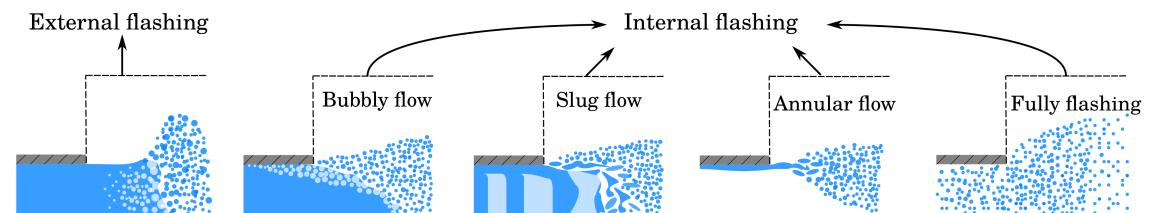


Figure 2.5: Different flow modes for flash boiling, according to [15, 73, 74, 102].

cleation and growth rates and therefore favours the onset of flash boiling.

2. Ambient pressure p_∞ : for a fixed liquid temperature a decrease in p_∞ increases the degree of superheat. Bubble nucleation and growth increase and flash boiling occurs faster. At the same time, for a fixed tank pressure p_0 a decrease in the ambient pressure increases the flow velocity of the liquid u_{liq} within the nozzle.
3. Flow velocity u_{liq} in the nozzle: On the one hand increasing velocities decrease the residence time within the nozzle and therefore the time for heterogeneous nucleation to take place. On the other hand an increased flow velocity increases the mechanical disturbances of the liquid jet and the resulting fluctuations favour homogeneous nucleation in the bulk liquid phase. Moreover, the influence of velocity on the mechanical forces becomes important in the transition regime between flash boiling and mechanical break-up.
4. Nozzle length L : Shorter nozzles result in shorter residence times of the liquid within the nozzle and therefore less heterogeneous nucleation.
5. Nozzle diameter D : Larger nozzle diameters increase the inertial forces and thus, possible disturbances that force homogeneous bubble nucleation. Moreover, inertia forces become important in the transition between flash boiling and mechanical break-up.

These interactions emphasize the complexity of flash boiling. The experimental studies showed that the generated sprays may occur in various shapes and a generalised empirical description is not yet found. Therefore, a fully predictive numerical simulation remains a challenging task. The current research efforts in the numerical simulation of flash boiling are summarised in the subsequent section.

2.4 Numerical simulation of flash boiling

2.4.1 Macroscopic models for flash boiling

Sections 2.1 to 2.3 revealed the most important thermo- and hydrodynamic aspects of flash boiling sprays. These yield a number of challenges for the numerical simulation at an industrial scale:

1. The flow solver needs to distinguish between liquid and vapour. This problem involves several length and time scales. While the liquid core of a jet has

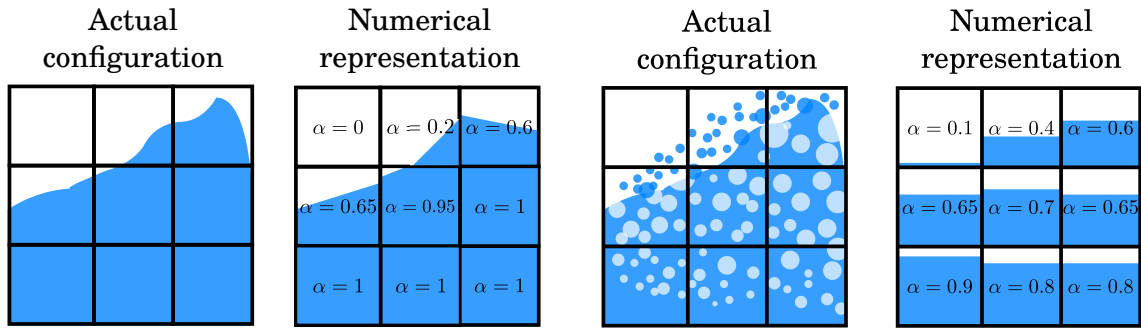
a macroscopic dimension the droplets of the generated spray may occur at a microscale. In the former case the liquid core and the surrounding gas form two distinct bulk phases. In the latter case a disperse cloud of microscopic droplets exists. This droplet cloud occurs as a homogeneous mixture of liquid and vapour on the macroscopic scale. Different modelling strategies exist for these regimes. The existence of vapour bubbles further complicates the problem. Depending on their number and size bubbles may be treated as separate bulk phases or disperse bubble clouds. A general computational framework must therefore cover the different flow regimes discussed in Fig. 2.5.

2. The transition from liquid to vapour needs to be considered. The nucleation of bubbles, the growth of these bubbles by vaporisation at the surface as well as vaporisation into the vacuum chamber from the surface of the liquid core and from the generated droplets are the four relevant phase transition processes. They are controlled by multiple physical mechanisms and it is therefore difficult to capture the phase transition by a single model only.
3. The break-up of the liquid jet and the resulting spray pattern strongly depend on the regime. Cases with a low superheat are primarily influenced by mechanical and thermodynamic forces but the influence of bubble nucleation and growth becomes dominant for higher superheats. Again, a prediction of the entire break-up process from the liquid jet core to the smallest droplets is difficult to describe with a single model.

One way to classify numerical methods for two-phase flows is to distinguish between Euler-Euler and Euler-Lagrange approaches [119]. Two main strategies evolved for the numerical simulation of flash boiling using either of the two techniques.

Euler-Euler methods treat both phases as a continuum and the governing equations (see Sec. 3.1) are solved in the liquid and vapour, respectively. An additional transport equation accounts for the volume fraction α or mass fraction \mathcal{X} of one of the two phases. If α represents the volume fraction of the liquid, computational cells with $\alpha = 1$ and $\alpha = 0$ solely contain liquid and gas, respectively. Each cell with $0 < \alpha < 1$ will contain both, liquid and vapour. In the context of DNS for multiphase flows α represents the relative amount of the liquid (or gas) with a well defined single interface in each cell, e.g. Schlottke and Weigand [96]. In this case special algorithms reconstruct a discret interface geometry from the volume fractions of neighbouring cells [89]. Figure 2.6(a) shows an exemplary two-phase

problem and its geometrical representation by a reconstructed interface. Section 1 has given an example for possible length scales and the resulting requirements on the computational effort for flash boiling. A resolution of individual well defined interfaces in each cell is therefore not feasible on an industrial scale. The liquid volume fraction would represent a liquid-vapour mixture with multiple interfaces as indicated in Fig. 2.6(b). The numerical representation of the volume fraction does not account for the geometry of individual interfaces. Thus, the derivation and calibration of suitable models representing the vaporisation is complex because α does not provide any information on the flash boiling regime, bubble or droplet sizes and densities. The most commonly used model in this context is the homogeneous relaxation model (HRM). The source term on the right hand side of the vapour mass



(a) Interface reconstruction algorithms (e.g. PLIC [89]) can determine the geometry if each cell represents a single interface.

(b) If one cell contains multiple interfaces the geometry of individual interfaces cannot be determined from the α field.

Figure 2.6: The volume fraction α represents the relative amount of liquid in a computational cell.

fraction equation [12]

$$\frac{D\mathcal{X}}{Dt} = \frac{\bar{\mathcal{X}} - \mathcal{X}}{\Theta} \quad (2.6)$$

accounts for the transition from liquid to vapour. The source term may be interpreted in the following way: the metastable liquid state in Fig. 2.1(b) is relaxed towards a stable mixture of liquid and vapour as described by the two-phase region in Fig. 2.1(a). The equilibrium mass fraction $\bar{\mathcal{X}}$ is determined based on the enthalpy of the superheated liquid and the saturation enthalpies of the liquid and the vapour at the local pressure [12]. The relaxation time Θ is the key parameter in the HRM determining how fast the transition from superheated liquid to a two-phase mixture in equilibrium occurs. The relaxation time needs to be adjusted for individual applications and can therefore also be used to adapt the model to

different flashing regimes. Downar-Zapolski et al. [28] introduced a model for determining Θ for one-dimensional channel flows. The model development is based on the „Moby Dick“experiments by Reocreux [88]. They used a long tube that mimics one-dimensional conditions and expanded a liquid below its saturation pressure. The mass flow rate, pressure and volume fraction were measured along the axial direction of the tube. Downar-Zapolski et al. [28] used these results to derive an analytical equation for the relaxation time Θ as a function of the pressure and volume fraction. The model has been developed for water in quasi one-dimensional tubes but additional empirical constants allow for a calibration of the model to different conditions. Moreover, Downar-Zapolski et al. [28] derived separate equations for a low pressure treatment and a high pressure treatment. While the low pressure treatment gave reasonable results for back pressures below $p = 10$ bar the high pressure treatment was applied beyond this limit. These studies are the basis for many other investigations. Schmidt and his coworkers [97, 98] applied the HRM for flashing water in pipes in two space dimensions. Generally they obtained good results, but the simulations did not agree to the experiments for all of their test conditions. They associate the differences to the extended problem domain without a corresponding calibration of the model coefficients in the HRM. Until today there is no database or calibration rule that allows to adapt the model coefficients with respect to the operating fluid, nozzle geometry and ambient conditions. In particular, there is no correlation explicitly tailored for the simulation of a flashing jet (instead of flashing within the nozzle). Therefore, the correlations derived by Downar-Zapolski et al. [28] are still the basis for most simulations of injectors and jets alike. Gopalakrishnan [41] and Neroorkar [71] extended the studies of Schmidt and co-workers [97, 98] to three-dimensional setups including the expansion of the liquid jet in the chamber for different fluids. Similar setups were investigated with the HRM by Duan et al. [29, 30] (jet expansion), Lee et al. [63] (injector flow and jet) and Saha et al. [92] (injector flow and jet). A mutual conclusion is, that the HRM predicts the characteristic properties qualitatively well. For certain configurations numerical results deviate from experiments. This is usually attributed to the lack of calibrated model coefficients discussed before. First attempts to tailor the HRM were made by Ramcke [84] for injector flows (modification of the threshold for switching between low and high pressure treatment) and by Gärtner [39] for nitrogen jets (modification of one model coefficient). However, the available information on the model calibration is still limited and needs further extension. A thorough jus-

tification for the applicability of the existing correlations to flash boiling does it exist.

Euler-Lagrange methods treat one phase as a continuum and the other phase as Lagrangian point particles. In the context of spray simulations a carrier continuous gas phase contains droplets which are tracked by a Lagrangian scheme [119]. Transport equations for the location and the momentum are solved for each particle or for groups of particles. Additional model equations describe the temporal evolution of the mass and energy of the droplets. Source terms in the transport equations for the Lagrangian particles and the Eulerian fields account for the interactions between the liquid and the gas phases, respectively. These interactions typically depend on sub-scale processes and appropriate models are required. Three important aspects in the spray modelling that need a special treatment in the case of flash boiling are the primary break-up of the liquid core, the secondary break-up of ligaments and droplets and the vaporisation of the droplets. A well established model for the mechanically driven primary break-up of liquid sheets is the LISA (linear stability analysis) model [101]. Zuo et al. extended this model for flash boiling conditions [122]. They calibrated the droplet sizes obtained from the classical LISA model depending on the degree of superheat with the aid of experimental data. Alternatively, it is possible to omit the primary jet break-up and directly initialise droplets within the simulation domain or at the inlet. This was done for flash-boiling sprays by Weber [115], Ma and Roekaerts [66] as well as Ramcke [84]. In this case the characteristic properties of the spray need to be prescribed to the simulation. This includes the droplet sizes (SMD, size distribution), the droplet velocity distributions, the spray angle and initial position of the droplets. Weber [115], Ma and Roekaerts [66] as well as Ramcke [84] directly prescribed the droplet SMD and the spray angle. Ma [66] obtained the input values from corresponding experiments. Ramcke [84] carried out a parametric study and selected the final input parameters by comparing the numerical results to experiments. Alternatively, Cleary et al. [19] and Witlox et al. [117] proposed a correlation between the SMD and the degree of superheat for different regimes of flash boiling. Some works also include the secondary break-up. Here, a large primary droplet contains one bubble or multiple bubbles. The bubbles grow and one primary droplet breaks up into smaller droplets when the vapour volume fraction exceeds a critical value. Weber [115], Zeng and Lee [121] as well as Kawano et al. [52] gave examples for this approach.

Both, the Euler-Euler approach and the Euler-Lagrange approach, are promising for the macroscopic simulation of flash boiling but some disadvantages remain. The HRM treats the phase transition as a global relaxation towards the thermodynamic equilibrium. The volume or mass fraction cannot represent the size and shape of individual bubbles within a single computational cell (see Fig. 2.6(b)). An approximation of bubble sizes would be possible only if a bubble number density is known. The capabilities of experimental investigations do not allow to provide bubble number counts in the liquid volume. The nucleation rates given by the relevant nucleation theories easily vary for one or more orders of magnitude and make a precise estimation difficult. Moreover, the known relaxation time scales are based on experiments of water in shock tube and may not apply to other conditions. Therefore, the HRM does not account for the different regimes shown in Fig. 2.5. An Euler-Lagrange method needs a priori data of the spray properties (angle, droplet size etc.) to properly initialise the carrier flow field and the droplets for the computation. The primary break-up is usually not resolved and separate data sets are required for individual cases. Simulation strategies providing a higher level of detail are therefore preferable. Two-equation models have a great potential to improve the existing simulation strategies. One example for such two-equation models is the Σ - Y -model. Here, a volume fraction equation and additionally an equation for the surface density, i.e. the ratio of the interface area in one computational cell and the cell volume, are solved [112, 113]. If the volume fraction and the surface density are known the size and the density of bubbles or droplets can be derived. The equations for the volume fraction and surface density require source terms that account for the generation and destruction of volume or surface. These source terms describe the break-up of the liquid jet. Models for mechanical jet break-up were applied in the context of such two-equations models. An example is the ELSA-model which has been coupled with both, the Reynolds-averaged Navier-Stokes (RANS) equations [61] and large eddy simulation (LES) for application in turbulent flows [18, 70]. The most significant advantage of a two-equation model is the extended knowledge on the interface geometry. This allows for a better differentiation between the different regimes of flash boiling. Recently, Rachakonda et al. [83] incorporated the Σ - Y -model to an HRM-based code for flash boiling. However, they used the Σ - Y -approach only to model the primary jet break-up while the secondary break-up and vaporisation were not accounted for (vaporisation is treated within the HRM-context for the vapour quality equation only). Lyras et al. [65] were the first to incorporate source terms for the phase

transition of a flash boiling liquid into the Σ - Y -model. Besides the traditional terms that describe the spray atomisation due to turbulence and aerodynamic break-up they added terms that include the impact of vaporisation. Here, Lyras et al. differentiate between a dense and a dilute vaporisation regime. In the dilute regime the source terms are based on models for droplet vaporisation as given by Abramzon and Sirignano [3]. The source term in the dense regime is adapted from the HRM-model similarly using the relaxation time Θ for calibration. As discussed before, there is no established data base that provides a reasonable calibration for different fluids or for the different flash boiling regimes. An extension of the source terms for the dense regime might be based on bubble expansion rates within the superheated liquid core. In some works single bubble models are used to account for the phase transition and jet expansion [51, 100] but these methods are not based on a two-equation model. The single bubble models allow for the description of the local production and destruction rates of volume/surface but it requires that the bubble is surrounded by a sufficiently large reservoir of superheated liquid. If a liquid jet contains numerous vapour bubbles, this assumption may get violated because bubbles can and will influence each other and thus affect the overall jet expansion rate. Therefore, the major objective of the present work is an analysis of the effect of bubble-bubble interactions with respect to growth rates within superheated liquid jets by the aid of direct numerical simulations (DNS). Chapter 5 introduces the process conditions as given by the experiments on LOX injection at the German Aerospace Center in Lampoldshausen [58]. The DNS are conducted with a fully compressible two-phase solver that accounts for phase change. The development and application of such flow solvers is a recent and active research field itself. The following section summarises the state-of-the-art for the compressible simulation of liquid-vapour flows with phase transition.

2.4.2 Direct Numerical simulation of compressible two-phase flows

A good number of compressible multiphase solvers have been developed within the last decade with recent examples introduced in references [17, 35, 36, 48, 60, 64, 93, 94, 120]. Saurel and his co-workers [93, 94] as well as Zein et al. [120] solved separate equation systems for the two phases including one volume fraction equation for each phase. The phase indicator diffuses across several cells which are treated as

homogeneous mixtures of liquid and vapour. This allows to treat two-phase flows for larger length scales because interfaces of individual bubbles do not need to be resolved. However, a sharp separation of the two phases, as it is needed for a DNS of bubble dynamics at a sub-grid scale, is difficult to achieve. Chang et al. [17] solved the fully compressible Navier-Stokes equations with a level-set approach [107] that keeps the interface between liquid and vapour sharp. However, Chang et al. did not account for phase change. Lauer et al. [60], Lee and Son [64] and Fechter et al. [35, 36] combined the level-set algorithm with compressible solvers that can account for phase transition. Lauer et al. [60] used interface Riemann solvers without phase change but source terms accounted for the mass transfer from liquid to vapour. They estimated the mass fluxes with the Hertz-Knudsen relation and calibrated the model coefficients for oscillating cavitation bubbles. However, the physics of oscillating bubbles differs from the physics of vapour bubble growth. Moreover, Lauer et al. [60] considered water and the coefficients may not be valid for other fluids. Lee and Son [64] used a ghost fluid method and incorporate phase transfer into the jump conditions which determine the ghost states. They estimated the mass flux from the heat balance at the interface which requires a suitable resolution of the temperature boundary layer. The heat flux determines the mass flux at the interface and no model coefficient requires calibration. Lee and Son [64] used this solver to investigate the growth and shrinkage of single compressible bubbles. However, the present work focuses on LOX jets under flash boiling conditions where thermal boundary layers are thin and their resolution is not feasible if numerous bubbles are to be resolved in the computational domain. Fechter et al. developed an exact [35] and an approximative [36] Riemann solver for general two-phase Riemann problems. The equation system consisted of Rankine-Hugoniot and interface jump conditions and they used a kinetic relation to estimate vaporisation rates. In [36] they showed that the approximate Riemann solver, called HLLP Riemann solver, is faster than the exact solver and it gives a reasonable approximation of the phase transition in shock tubes and for single droplets. This Riemann solver is a modification of HLLC-type Riemann solvers [49] and will be the basis of the present computations. However, the HLLP Riemann solver had only been applied to shock tubes and single droplets. The assumptions and vaporisation models for these type of flows are not necessarily applicable to multiple bubble growth. Therefore, an important aspect of the present work is the assessment of the HLLP Riemann solver with respect to vapour bubble growth and the derivation and calibration of models for the vaporisation mass flux.

CHAPTER 3

Governing equations

The universal conservation laws that govern the transport of fluids are the continuity equation (mass conservation), the Navier-Stokes equations (momentum conservation) and the energy conservation equation. They are of the general form

$$\begin{pmatrix} \text{Temporal} \\ \text{change} \\ \text{of conserved} \\ \text{quantity} \end{pmatrix} + \begin{pmatrix} \text{Advective} \\ \text{transport} \\ \text{of conserved} \\ \text{quantity} \end{pmatrix} = \begin{pmatrix} \text{Diffusive} \\ \text{transport} \\ \text{of conserved} \\ \text{quantity} \end{pmatrix} + \begin{pmatrix} \text{Change due} \\ \text{to sources} \\ \text{and external} \\ \text{forces} \end{pmatrix}. \quad (3.1)$$

In the following, the term Navier-Stokes equations and its acronym NSE refer to the entire set of conservation laws consisting of mass, momentum and energy equations. This chapter provides the fundamental physical equations and models describing compressible two-phase flows with phase transition. The relevant equation system for a single phase is detailed in Sec. 3.1. The interface between liquid and vapour is characterised by discontinuous jumps in the fluid states, most notably for the density. The transport equations do not inherently account for these discontinuities and are solved separately for the two phases. The conditions that couple the isolated domains are introduced in Sec. 3.2. The models applied to determine the vaporisation mass fluxes are outlined in Sec. 3.3. For compressible flows the Navier-Stokes equations are not a closed system and an equation of state (EOS) provides the additionally required correlation, see Sec. 3.4. Besides these physical laws and models Sec. 3.5 introduces the interface capturing approach. From here on, bold symbols represent vectors or matrices, and the subscripts 1, 2 and 3 indicate the Cartesian coordinate directions.

3.1 Conservation laws in the bulk phases

The compressible NSE are [111]

$$\mathbf{U}_t + \nabla \cdot \mathbf{F}^A(\mathbf{U}) = \nabla \cdot \mathbf{F}^D(\mathbf{U}, \nabla \mathbf{U}), \quad (3.2)$$

where

$$\mathbf{U} = (\rho, \rho u_1, \rho u_2, \rho u_3, \rho E)^T \quad (3.3)$$

is the vector of the conserved variables. Here, u_1 , u_2 , u_3 and E are the three Cartesian velocity components and the total specific energy, respectively. The latter is the sum of the internal energy e and the kinetic energy, $E = e + \frac{u_i^2}{2}$ [7]. Einstein's notation is used to sum over double indices. The subscript t in Eq. (3.2) indicates the partial derivative in time. The vectors of advective fluxes \mathbf{F}^A for the three Cartesian coordinate directions read

$$\mathbf{F}_1^A = \begin{pmatrix} \rho u_1 \\ \rho u_1^2 + p \\ \rho u_2 u_1 \\ \rho u_3 u_1 \\ u_1(\rho E + p) \end{pmatrix}, \quad \mathbf{F}_2^A = \begin{pmatrix} \rho u_2 \\ \rho u_1 u_2 \\ \rho u_2^2 + p \\ \rho u_3 u_2 \\ u_2(\rho E + p) \end{pmatrix}, \quad \mathbf{F}_3^A = \begin{pmatrix} \rho u_3 \\ \rho u_1 u_3 \\ \rho u_2 u_3 \\ \rho u_3^2 + p \\ u_3(\rho E + p) \end{pmatrix}. \quad (3.4)$$

They define the transport of a conserved quantity with the fluid velocity. Here, the pressure force is also included in the advective flux vector. The diffusive fluxes \mathbf{F}^D are defined by

$$\mathbf{F}_1^D = \begin{pmatrix} 0 \\ \tau_{11} \\ \tau_{12} \\ \tau_{13} \\ u_1 \tau_{11} + u_2 \tau_{12} + u_3 \tau_{13} - q_1 \end{pmatrix}, \quad \mathbf{F}_2^D = \begin{pmatrix} 0 \\ \tau_{21} \\ \tau_{22} \\ \tau_{23} \\ u_1 \tau_{21} + u_2 \tau_{22} + u_3 \tau_{23} - q_2 \end{pmatrix},$$

$$\mathbf{F}_3^D = \begin{pmatrix} 0 \\ \tau_{31} \\ \tau_{32} \\ \tau_{33} \\ u_1 \tau_{31} + u_2 \tau_{32} + u_3 \tau_{33} - q_3 \end{pmatrix}. \quad (3.5)$$

The stress tensor τ_{ij} describes the viscous forces. The present work considers Newtonian fluids where τ_{ij} depends linearly on the velocity gradients, viz.

$$\tau_{ij} = \mu \left(\left(\frac{\partial u_i}{\partial x_j} + \frac{\partial u_j}{\partial x_i} \right) - \frac{2}{3} \frac{\partial u_k}{\partial x_k} \delta_{i,j} \right) \quad (3.6)$$

with the Kronecker delta δ_{ij} . The heat flux in the energy equation reads

$$q_i = -k \frac{\partial T}{\partial x_i}. \quad (3.7)$$

The fluid properties μ in Eq. (3.6) and k in Eq. (3.7) are the dynamic viscosity and the heat conductivity, respectively, which can be obtained from material laws.

3.2 Conservation laws at the interface

The conserved quantities are not continuous across the interface but the liquid and the vapour states are coupled by jump conditions [50]. The present work uses a sharp interface approach. This means that each fluid state is clearly distinguishable into liquid or vapour and no mixture states appear. This approximation corresponds to Fig. 2.1(b). In this case, the interface is infinitely thin and cannot store mass, momentum or energy. The jump conditions are derived by equating the advective and diffusive flux terms in Eq. (3.2) for both sides of the interface as shown by Ishii and Hibiki [50]. The general expression

$$[[\phi]] = \lim_{x_{\text{int}}+h \rightarrow 0} \phi - \lim_{x_{\text{int}}-h \rightarrow 0} \phi \hat{=} \phi_{\text{liq}}|_{x=x_{\text{int}}} - \phi_{\text{vap}}|_{x=x_{\text{int}}} \quad (3.8)$$

is used subsequently with x_{int} being the location of the interface. The following correlations consider an interface which lies normal to the x -direction. In the general case, all vectorial quantities have to be rotated to the interface normal direction subscribed by n and the interface tangential directions subscribed by t_1 and t_2 , respectively. The rotation uses the interface normal vector \mathbf{n}_{int} and the interface tangential vectors $\mathbf{t}_{1,\text{int}}$ and $\mathbf{t}_{2,\text{int}}$ and reads

$$\phi_n = \boldsymbol{\phi} \cdot \mathbf{n}_{\text{int}}, \quad \phi_{t1} = \boldsymbol{\phi} \cdot \mathbf{t}_{1,\text{int}}, \quad \phi_{t2} = \boldsymbol{\phi} \cdot \mathbf{t}_{2,\text{int}}. \quad (3.9)$$

The normal and tangential vectors of the interface are defined in Sec. 3.5.

Continuity equation

The continuity condition

$$0 = \llbracket \dot{m}'' \rrbracket \quad (3.10)$$

requires that the mass fluxes \dot{m}'' to and away from the interface are equal. These mass fluxes are defined by [50, 119]

$$\dot{m}'' = \rho_{\text{liq}}(u_{1,\text{liq}} - S_{\text{int}}) = \rho_{\text{vap}}(u_{1,\text{vap}} - S_{\text{int}}) \quad (3.11)$$

with S_{int} being the interface normal velocity. The expression $\rho(u_1 - S_{\text{int}})$ corresponds to the advective term in the continuity equation with $(u_1 - S_{\text{int}})$ being the relative normal velocity of the fluid to the interface. Combining Eqs. (3.10) and (3.11) yields the continuity jump condition

$$0 = \llbracket \rho(u_1 - S_{\text{int}}) \rrbracket. \quad (3.12)$$

Momentum equation

The momentum balance across the interface is given by [50, 119]

$$\begin{aligned} \sigma\kappa &= \llbracket \rho u_1(u_1 - S_{\text{int}}) + p - \tau_{1,1} \rrbracket, \\ 0 &= \llbracket \tau_{1,2} \rrbracket, \\ 0 &= \llbracket \tau_{1,3} \rrbracket. \end{aligned} \quad (3.13)$$

and includes advective fluxes, viscous stresses, pressure and surface forces. The volume specific momentum ρu_1 is convected with the relative velocity $(u_1 - S_{\text{int}})$ on both sides of the interface. The difference between the liquid and the vapour pressure defines the pressure force on the interface. Additionally, the surface tension force needs to be considered. It is equal to the product of the surface tension coefficient σ and the curvature κ . The normal stress $\tau_{1,1}$ as well as the tangential stresses $\tau_{1,2}$ and $\tau_{1,3}$ act on the interface. Without slip the tangential velocities at the interface are the same from the liquid and the vapour side with equal tangential stresses. Since the interface is infinitely thin, tangential stresses cannot influence the normal component of the momentum (cf. Fig. 2.4 in Versteeg and Malalasekera, *An introduction to Computational Fluid Dynamics - The Finite Volume Method*, 2007 [114]). In mechanical equilibrium the jump condition for the normal component of

the momentum defines the pressure jump between liquid and vapour:

$$\sigma\kappa = p_{\text{liq}} - p_{\text{vap}}. \quad (3.14)$$

Energy equation

The energy balance at the interface is defined by [50, 119]

$$\sigma\kappa S_{\text{int}} = \llbracket (\rho E)(u_1 - S_{\text{int}}) + pu_1 + q_1 + u_i\tau_{1i} \rrbracket. \quad (3.15)$$

The four terms on the right hand side account for the advective flux, the pressure work, the heat flux and the work done by viscous stresses, respectively. The left hand side incorporates the surface tension work into the energy balance. Equation (3.15) can be rewritten in terms of the specific enthalpy h as defined by Eq. (2.1). In a first step the momentum balance given by Eq. (3.13) is multiplied by S_{int} and subtracted from Eq. (3.15). In a second step, the total specific energy E is replaced by $e + 1/2u^2 = h - pv + 1/2u^2$. The pressure terms and the surface tension cancel and the final enthalpy balance yields

$$\begin{aligned} 0 &= \left\llbracket \rho(u_1 - S_{\text{int}}) \left(h + \frac{u^2}{2} - uS_{\text{int}} \right) + q_1 + u_i\tau_{1i} - S_{\text{int}}\tau_{11} \right\llbracket \\ &= \left\llbracket \dot{m}'' \left(h + \frac{u^2}{2} - uS_{\text{int}} \right) + q_1 + u_i\tau_{1i} - S_{\text{int}}\tau_{11} \right\llbracket \end{aligned} \quad (3.16)$$

The enthalpy jump $\llbracket h \rrbracket$ corresponds to the latent heat of vaporisation h_{fg} as given by Eq. (2.2). The commonly applied condition

$$\dot{m}'' h_{\text{fg}} = q_{1,\text{liq}} - q_{1,\text{vap}}. \quad (3.17)$$

can be derived from Eq. (3.16) if the the work done by viscous stresses ($u_i\tau_{1i} - S_{\text{int}}\tau_{11}$), the kinetic energy ($\dot{m}''u^2/2$) and the term $\dot{m}''uS_{\text{int}}$ are negligible. Viscous stresses are small for cases with low velocities [57]. The jump in the kinetic energy is typically small as exemplified using conditions relevant for the present work. The latent heat of vaporisation for oxygen at $T = 120$ K is $h_{\text{fg}} = 173.658$ kJ/kg and the fluid velocities are below 100 m/s. Thus, the latent heat of vaporisation exceeds the kinetic energy by more than one order of magnitude. The term $\dot{m}''uS_{\text{int}}$ is of the same order as the kinetic energy and Eq. (3.17) is applicable under the present conditions.

In summary, the full jump conditions for the conservation of mass, momentum and energy read

$$\begin{aligned}
0 &= \llbracket \rho(u_1 - S_{\text{int}}) \rrbracket, \\
\sigma\kappa &= \llbracket \rho u_1(u_1 - S_{\text{int}}) + p - \tau_{1,1} \rrbracket, \\
0 &= \llbracket \tau_{1,2} \rrbracket, \\
0 &= \llbracket \tau_{1,3} \rrbracket, \\
\sigma\kappa S_{\text{int}} &= \llbracket (\rho E)(u_1 - S_{\text{int}}) + pu_1 + q_1 + u_i \tau_{1i} \rrbracket.
\end{aligned} \tag{3.18}$$

3.3 Vaporisation model

The interface velocity S_{int} is an additional unknown in the system of equations as defined by the Eqs. (3.2) with jump conditions (3.18). The mass flux \dot{m}'' and S_{int} are coupled by Eq. (3.11). Equation (3.17) is typically used to estimate the vaporisation rate at the interface. The heat flux q is determined by Eq. (3.7) using the temperature condition

$$T_{\text{int}} = T_{\text{sat}}(p). \tag{3.19}$$

This allows to estimate the temperature gradients at the interface but a suitable resolution of the temperature boundary layer is required. Sections 5.1 and 5.2.4 discuss the challenges for a direct computation of the temperature gradients and therefore of the heat and mass fluxes for the present operating conditions. Alternatively, the mass flux can be approximated by vaporisation models. The present work uses three models which are introduced now.

The Hertz-Knudsen relation (HKR)

The HKR originates from [44] and [55] and is based on a mass balance at the liquid-vapour interface. This balance law is derived from kinetic gas theory comparing the molecule fluxes from and to the interface. Schrage [99] comprehensively discussed the HKR and Persad et al. [76] gave a recent review on its application and calibration. The model equation reads

$$\dot{m}'' = \frac{1}{\sqrt{2\pi\mathcal{R}}} \left(\lambda_{\text{vap}} \frac{p_{\text{sat}}}{\sqrt{T_{\text{liq}}}} - \lambda_{\text{cond}} \frac{p_{\text{vap}}}{\sqrt{T_{\text{vap}}}} \right) \tag{3.20}$$

where \mathcal{R} , λ_{vap} and λ_{cond} are the specific gas constant, a vaporisation and a condensation coefficient, respectively. The model coefficient are problem dependent and have to be adjusted. Appendix A provides a detailed derivation of Eq. (3.20).

The kinetic relation (KR)

Fechter et al. [36] used the KR in their original formulation of the HLLP Riemann solver. They provided a detailed derivation for the final model equation [35],

$$\dot{m}'' = \frac{1}{c_{\text{ent}}} T_{\text{ref}} \llbracket s - s_{\text{sat}} \rrbracket. \quad (3.21)$$

This model ensures consistency with the second law of thermodynamics, but entropy production at the interface is unknown and requires scaling by the coefficient c_{ent} [35]. For constant interface states, \dot{m}'' is inversely proportional to c_{ent} such that the estimated mass flux decreases with an increasing model coefficient. The derivation of Eq. (3.21) is also given in Appendix A.

A sub-grid scale heat flux model (SHFM)

The SHFM is based on the energy balance at the interface. Neglecting the heat diffusion in the vapour phase the mass flux is obtained as the ratio of an approximated heat flux in the liquid phase and the latent heat, viz.

$$\dot{m}'' = \frac{q_{\text{liq}} - q_{\text{vap}}}{h_{\text{fg}}} \approx \frac{q_{\text{liq}}}{h_{\text{fg}}}. \quad (3.22)$$

The assumption of negligible diffusive heat fluxes in the vapour phase is justified as small temperature gradients in the bubble at the interface can be expected [62]. The heat diffusivity is higher in the liquid and the heat flux in the vapour becomes important only for very large temperature gradients. As the HLLP Riemann solver does not allow for diffusive effects, the thermal boundary layer will not be resolved and the heat flux, q_{liq} , is approximated by

$$q_{\text{liq}} = -k_{\text{liq}} \left. \frac{dT}{dx} \right|_{x=x_{\text{int}}} \approx -k_{\text{liq}} 2 \frac{T_{\infty} - T_{\text{sat}}}{\delta}, \quad (3.23)$$

assuming a parabolic temperature profile in the boundary layer as illustrated in Fig. 3.1(a). Similar approaches to estimate the heat flux in an unresolved thermal boundary layer exist for droplets [95] but have not intensively been discussed in the

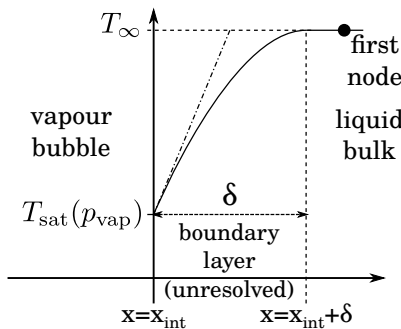
context of vapour bubble growth. The model can be implemented in the current compressible simulations by the following steps:

- The saturation temperature is determined from the vapour pressure inside of the bubble. Starting from isothermal conditions the mass flux is initially set to zero.
- The bubble growth is triggered numerically and with increasing size the pressure in the bubble will decrease.
- The saturation temperature will then decrease and the temperature gradient in Eq. (3.23) becomes non-zero. The mass flux increases proportional to the temperature gradient.
- If the mass flux increases continuously, the vapour pressure will increase and the decreasing temperature gradient relaxes the mass flux.

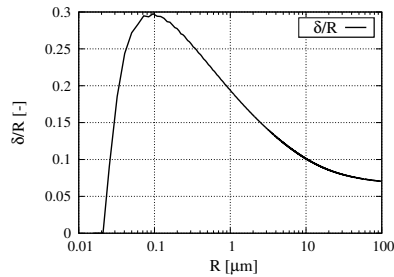
The accuracy of the SHFM depends on the estimation of the boundary layer thickness in Eq. (3.23) which is determined by

$$\delta = C_\delta R. \quad (3.24)$$

Figure 3.1(b) shows an example for the ratio $\delta/R = C_\delta$ as a function of the bubble radius R . As a first approach, the present work uses a constant C_δ calibrated separately to each individual test case.



(a) Sketch of the temperature profile at the interface between liquid and vapour.



(b) Ratio between boundary layer thickness and bubble radius as a function of the bubble radius.

Figure 3.1: Aspects of the sub-grid scale heat flux model.

3.4 Equation of state

The equation system (3.2) provides five equations for the six unknowns ρ , u_1 , u_2 , u_3 , e and p and is therefore unclosed. The jump conditions in Sec. 3.2 and the vaporisation models in Sec. 3.3 couple the liquid and the vapour phases but do not provide new equations for closure. An EOS of the form $p = f(\rho, e)$ is additionally needed. The most simplistic EOS is the perfect gas law with the thermal EOS $p = \rho \mathcal{R}T$. This equation correlates the pressure with the density and the temperature. The caloric EOS $e = c_v T$ provides then the correlation with the internal energy e using the specific heat capacity at a constant volume c_v . The perfect gas law is, however, valid for monoatomic gases only. Therefore, more sophisticated models are needed for the computation of liquid-vapour flows with phase change. The present work uses the open-source EOS library CoolProp [11] and the Noble-Abel stiffened gas (NASG) EOS [68].

Further thermodynamic properties and transport properties are also required for the present simulations. Given that ρ and e are the known independent properties, the fluid temperature T , the specific entropy s and the speed of sound c are needed. Finally, the transport properties μ and k as well as the surface tension coefficient σ have to be determined by suitable material laws.

The EOS library CoolProp

Ian Bell and his co-workers comprehensively describe the functionality and the underlying methods in their pioneering CoolProp publication [11] and only a brief summary is given here. CoolProp provides the thermophysical properties for a wide range of pure fluids. The correlations of the thermodynamic state properties are based on Helmholtz-energy-explicit EOS being the state-of-the-art for high-accuracy EOS. The correlations for the transport properties μ and k as well as the surface tension coefficient σ are either developed from experimental data, empirical or predictive methods [11]. Helmholtz-energy-explicit equations of state use the temperature and the density as independent variables. If other state properties are known numerical solvers are required to determine the unknown properties. This is exemplified by the correlation $p = f(\rho, e)$. The computational effort for the numerical solution of equation system (3.2) can strongly increase if the closing condition $p = f(\rho, e)$ requires a numerical solution itself. Therefore, the present work uses a tabulation strategy as presented by Föll et al. [37]. In a pre-processing step, the results of the EOS correlations are tabulated and later read in during runtime.

Noble-Abel stiffened gas EOS

Le Métayer and Saurel [68] provide the basic theory for the NASG-EOS and derive the correlations between the thermodynamic state properties. These correlations are empiric equations, they are simple to implement and the computation is fast. Subsequently, the NASG correlations needed for the computation within the present work are introduced. Note that the following equations are defined in terms of the specific volume v instead of the density ρ . The correlations that define the thermodynamic state properties pressure, temperature, speed of sound and specific entropy are:

$$p = \frac{(e - \tilde{q})(\gamma - 1)}{v - b} - \gamma P_\infty, \quad (3.25)$$

$$T = (v - b) \frac{p + P_\infty}{(\gamma - 1)C_v}, \quad (3.26)$$

$$c = \sqrt{\frac{\gamma v^2 (p - P_\infty)}{v - b}}, \quad (3.27)$$

$$s = C_v \ln \frac{T^\gamma}{(p + P_\infty)^{\gamma-1} + \tilde{q}'}. \quad (3.28)$$

The model coefficients γ , P_∞ , \tilde{q} , b , \tilde{q}' and C_v have to be determined for a specific fluid. Equations (3.25) to Eq. (3.28) are valid for both phases but separate model parameters apply for the liquid and the vapour, respectively. Le Métayer and Saurel [68] provide an algorithm to determine the model coefficients by the aid of reference data. In the present work the reference data is obtained from the CoolProp library.

At this point the entire physical model is determined and is summarised in the following: Equation system (3.2) describes the transport of the fluid but is solved separately for the liquid and the vapour phases. At the interface the two domains are coupled by the jump conditions given by Eqs. (3.18). The vaporisation mass flux is estimated based on one of the three models presented in Eqs. (3.20), (3.21) or (3.23). With the density from the continuity equation and the specific internal energy from the energy conservation equation all other thermodynamic properties and transport properties can be estimated from equations of state or material laws introduced in this section. Thus, the system of physical equations is closed and can be solved numerically.

3.5 Level-set equation

The flow solver needs to distinguish between the liquid and the vapour phase and several approaches have been developed in the past 30 to 40 years. The present DNS resolve individual vapour bubbles within a bulk liquid and the two phases are treated in an Euler-Euler framework. Among others, the most commonly used algorithms to capture the interface are the volume-of-fluid method introduced by Hirt and Nichols [47] and the level-set method of Sussman et al. [107]. The present work relies on the level-set algorithm because it guarantees the sharpness of the interface and it allows for a straight-forward determination of interface normal vectors and curvature.

The level-set approach uses a signed distance function $\Phi(\mathbf{x}, t)$ with its transport equation

$$\frac{\partial \Phi}{\partial t} + \mathbf{u}_{\text{LS}} \nabla \cdot (\Phi) = 0. \quad (3.29)$$

The level-set Φ determines the distance to the interface and the zero-isocontour of Φ defines the interface location. The advection velocity \mathbf{u}_{LS} is equivalent to the interface velocity S_{int} from Eq. (3.12). An extension of S_{int} to several neighbouring cells yields the level-set advection velocity \mathbf{u}_{LS} in the entire domain. For this purpose, a Hamilton-Jacobi equation is solved as described by Adalsteinsson and Sethian [4]. Similarly, the level-set function is reinitialized such that it remains a smooth distance function during the entire simulation [107].

The normal vector of the interface and its curvature are determined using the space derivatives of Φ according to:

$$\mathbf{n}_{\text{int}} = \frac{\nabla \Phi}{|\nabla \Phi|}, \quad \kappa = \nabla \cdot \frac{\nabla \Phi}{|\nabla \Phi|}. \quad (3.30)$$

The tangential vectors are derived from the normal vectors using the Gram-Schmidt orthonormalisation.

CHAPTER 4

Numerical Approach

The conservation equations introduced in Eqs. (3.2), (3.18) and (3.29) are solved numerically with the algorithms presented in the following sections. The basis for the spatial discretization is the discontinuous Galerkin spectral element method (DGSEM). It is coupled to a finite volume (FV) approach that enhances the stability and improves the representation of the liquid-vapour interface. These two algorithms are introduced in Secs. 4.1 and 4.2, respectively. Note that the term *DG solver* always refers to the entire flow solver consisting of the combined DGSEM and FV sub-cell approach. Both, the DGSEM and the FV approach are based on a balance of the fluxes across the cell faces. These fluxes are determined by means of the Riemann solvers presented in Sec. 4.3. The Runge-Kutta scheme described in Sec. 4.4 is used to integrate the semi-discrete form of the conservation laws.

Note: In Sec. 3.1 the components of the state vector \mathbf{U} and the flux vector \mathbf{F} represented the different conservation laws (mass, x -momentum, y -momentum, z -momentum, energy). The vectorial character of the flux with respect to the Cartesian direction was accounted for by the subscripts 1, 2 and 3. Within Secs. 4.1 and 4.2 the vector \mathbf{F} symbolises the flux of a single conservative quantity in the three space directions in order to simplify the derivation of the discrete equations. This single conservative quantity is therefore represented by a scalar U instead of a vector \mathbf{U} in Secs. 4.1 and 4.2. Any reference to the equations given in Ch. 3 refers to one single equation out of these equation systems, e.g. the mass conservation equation.

4.1 Discontinuous Galerkin spectral element method

The major aspects of the discontinuous Galerkin spectral element method (DGSEM) are

- a mapping of the conservation laws given in Eq. (3.2) from the physical space to a reference space,
- a sub-division of the computational domain into discontinuous Galerkin (DG) cells and
- a sub-cell resolution of the flow field within each DG cell.

The theoretical background of the DGSEM goes back to Reed and Hill [86] who used the DG scheme for the neutron transport equations. Cockburn and Shu extended these ideas in a series of papers to general hyperbolic conservation laws [20, 21, 22, 23, 24] allowing the computation of the time dependent Euler equations, i.e. Eq. (3.2) without viscous terms. Bassi and Rebay [9, 10] were the first to apply the DGSEM to the full Navier-Stokes equations. The present implementation relies on the work of Hindenlang et al. [46] who provided a detailed derivation of a three-dimensional explicit DGSEM. If not stated otherwise the following explanation is based on this work.

The governing equations are mapped from the physical space $\mathbf{x} = (x_1, x_2, x_3)^T$ to the reference space $\boldsymbol{\xi} = (\xi^1, \xi^2, \xi^3)^T$ and $\mathbf{x} = \mathbf{f}(\boldsymbol{\xi}) = \mathbf{x}(\boldsymbol{\xi})$ defines the mapping. Note that the superscripts $(\cdot)^1$, $(\cdot)^2$ and $(\cdot)^3$ indicate the three coordinate directions in reference space. The transformation from the physical space to the reference space uses two types of basis vectors [56]. Firstly, the covariant basis vectors

$$\mathbf{a}_j = \frac{\partial \mathbf{x}}{\partial \xi^j} \quad (4.1)$$

point in directions parallel to the coordinate lines in reference space. They are summarised by the Jacobian matrix [45]

$$\mathcal{J} = (\mathbf{a}_1, \mathbf{a}_2, \mathbf{a}_3)^T = \begin{bmatrix} \frac{\partial x_1}{\partial \xi^1} & \frac{\partial x_2}{\partial \xi^1} & \frac{\partial x_3}{\partial \xi^1} \\ \frac{\partial x_1}{\partial \xi^2} & \frac{\partial x_2}{\partial \xi^2} & \frac{\partial x_3}{\partial \xi^2} \\ \frac{\partial x_1}{\partial \xi^3} & \frac{\partial x_2}{\partial \xi^3} & \frac{\partial x_3}{\partial \xi^3} \end{bmatrix} \quad (4.2)$$

with its determinant

$$J = \mathbf{a}_1 \cdot (\mathbf{a}_2 \times \mathbf{a}_3). \quad (4.3)$$

Secondly, the contravariant basis vectors

$$\mathbf{a}^j = \frac{\partial \boldsymbol{\xi}}{\partial x_j} \quad (4.4)$$

point normal to the coordinate lines in reference space. The mapping between the physical space and the reference space is now defined with the aid of J and \mathbf{a}^j . The transformation of the gradient of a scalar ϕ in conservative form reads [45]

$$\nabla \phi = \frac{1}{J} \sum_{i=1}^N \frac{\partial}{\partial \xi^i} ((J\mathbf{a})^i) \phi. \quad (4.5)$$

Accordingly, a vector $\boldsymbol{\phi}$ is transformed by

$$\nabla \cdot \boldsymbol{\phi} = \frac{1}{J} \sum_{i=1}^N \frac{\partial}{\partial \xi^i} ((J\mathbf{a})^i) \cdot \boldsymbol{\phi}. \quad (4.6)$$

The following paragraph describes the mapping of Eq. (3.2) from physical space to reference space. Here, the flux vector $\mathbf{F} = \mathbf{F}^A - \mathbf{F}^D$ summarises the advective fluxes and the viscous fluxes. The mapped equations read

$$J(\boldsymbol{\xi})U_t(t, \boldsymbol{\xi}) + \nabla_{\boldsymbol{\xi}} \cdot \mathcal{F}(U(t, \boldsymbol{\xi})) = 0 \quad (4.7)$$

with

$$\mathcal{F}^i = (J\mathbf{a})^i \cdot \mathbf{F} = \sum_{n=1}^3 (Ja_n^i) F_n \quad (4.8)$$

and the nabla operator in reference space $\nabla_{\boldsymbol{\xi}} = (\partial/\partial \xi^1, \partial/\partial \xi^2, \partial/\partial \xi^3)$.

So far the mapping of the governing equations from the physical to the reference space is described. The paragraph now outlines the discretization of these equations in a discontinuous Galerkin framework. Equation (4.7) is subdivided into a set of control volumes Ω . The computational cells are mapped to a unit element $\boldsymbol{\mathcal{E}}$ of the size $[-1;1]$ in each direction in reference space. After multiplying the resulting

system of equations by a test function ϕ , the governing equations read [46]

$$\int_{\mathcal{E}} JU_t \phi d\xi + \int_{\mathcal{E}} \nabla_{\xi} \cdot \mathcal{F}(U) \phi d\xi = 0. \quad (4.9)$$

An integration by parts of the second term in Eq. (4.9) gives the weak formulation of the conservation laws,

$$\frac{\partial}{\partial t} \int_{\mathcal{E}} JU \phi d\xi + \int_{\partial \mathcal{E}} (\mathcal{F} \cdot \mathbf{N}) \phi dS - \int_{\mathcal{E}} \mathcal{F}(U) \cdot (\nabla_{\xi} \phi) d\xi = 0, \quad (4.10)$$

with the normal vector \mathbf{N} of the reference element face. The three terms on the left hand side are the time integral, the surface integral and the volume integral, respectively. Figure 4.1 illustrates the discretization of a one-dimensional domain in the DG context. A one-dimensional Lagrange polynomial of the degree N with the coefficients

$$l_i(\xi^1) = \prod_{\substack{k=0 \\ k \neq i}}^N \frac{\xi^1 - \xi_k^1}{\xi_i^1 - \xi_k^1}, \quad i = 0, \dots, N \quad (4.11)$$

represents the state U of the fluid within a DG cell. In three-dimensional space the exact fluid state is approximate by

$$U(\boldsymbol{\xi}, t) \approx \sum_{i,j,k=0}^N \hat{U}_{ijk}(t) \psi_{ijk}(\boldsymbol{\xi}). \quad (4.12)$$

using the basis functions

$$\psi_{ijk} = l_i(\xi^1) l_j(\xi^2) l_k(\xi^3). \quad (4.13)$$

Here, i , j and k indicate the three coordinate directions in reference space ξ^1 , ξ^2 and ξ^3 , respectively. In the DGSEM the interpolation points, i.e. the sample points of the Lagrange polynomials, and the integration points, i.e. the discretization points for the numerical approximation of the flow field, collocate. At the same time the Lagrange coefficients in Eq. (4.11) fulfill the Lagrange property

$$l_i(\xi_j) = \delta_{i,j}; \quad i, j = 0, \dots, N. \quad (4.14)$$

Therefore, \hat{U}_{ijk} is equivalent to the physical state U at the polynomial node i , j , k .

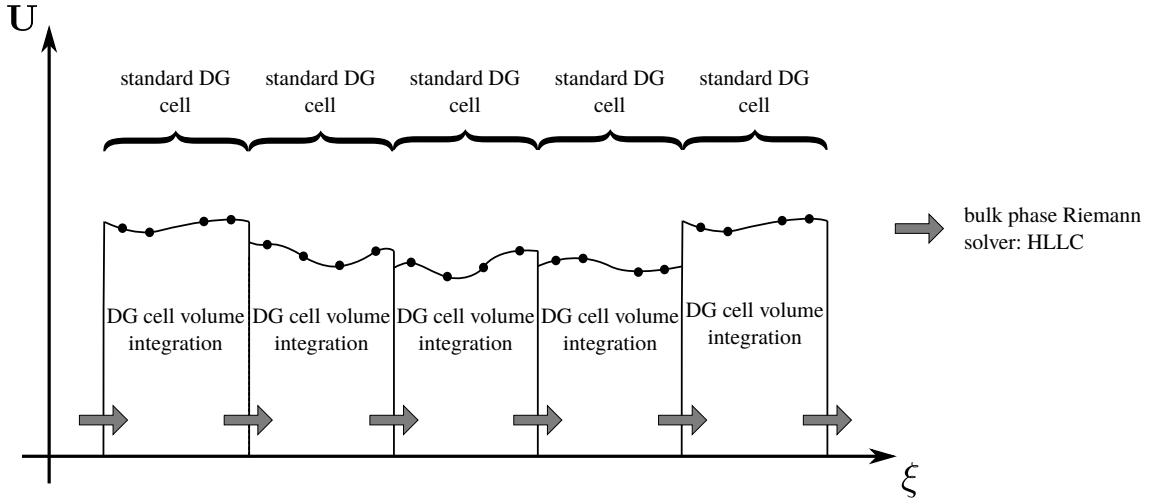


Figure 4.1: Discretization of a one-dimensional domain by DG cells with a sub-cell resolution defined by a third order polynomial.

Similarly, the flux \mathcal{F} is defined by

$$\mathcal{F}(U(\xi)) \approx \sum_{i,j,k=0}^N \hat{\mathbf{F}}_{ijk} \psi_{ijk}(\xi) \quad (4.15)$$

and, with the aid of Eq. (4.8), the representation of $\hat{\mathbf{F}}_{ijk}$ by the physical flux \mathbf{F} is

$$\hat{\mathcal{F}}^m = \sum_{d=1}^3 J \mathbf{a}_d^m(\xi_i^1, \xi_j^2, \xi_k^3) F_d(\xi_i^1, \xi_j^2, \xi_k^3). \quad (4.16)$$

The expressions in the preceding section are now used to derive the numerical approximations for the three integrals in Eq. (4.10)

Time derivative integral

The first term on the left hand side of Eq. (4.10) is the volume integral of the time derivative of U . Defining the test function by $\phi = \psi_{ijk}$ and using Eq. (4.12) gives

$$\frac{\partial}{\partial t} \int_{\mathcal{E}} J U \phi d\xi = \frac{\partial}{\partial t} \int_{\mathcal{E}} J(\xi) \left(\sum_{l,m,n=0}^N \hat{U}_{lmn} \psi_{lmn}(\xi) \right) \psi_{ijk} d\xi. \quad (4.17)$$

Now the integral over the reference element is split into the three coordinate directions, viz.

$$\frac{\partial}{\partial t} \int_{\mathcal{E}} JU\phi d\boldsymbol{\xi} = \frac{\partial}{\partial t} \int_{-1}^1 \int_{-1}^1 \int_{-1}^1 J(\boldsymbol{\xi}) \left(\sum_{l,m,n=0}^N \hat{U}_{lmn} \psi_{lmn}(\boldsymbol{\xi}) \right) \psi_{ijk} d\xi^1 d\xi^2 d\xi^3. \quad (4.18)$$

The Gauss-Legendre quadrature rule along with Eqs. (4.11) and (4.14) yields

$$\begin{aligned} \frac{\partial}{\partial t} \int_{\mathcal{E}} JU\phi d\boldsymbol{\xi} &= \frac{\partial}{\partial t} \sum_{\lambda,\mu,\nu=0}^N J(\boldsymbol{\xi}) \left(\sum_{l,m,n=0}^N \hat{U}_{lmn} \underbrace{l_l(\xi_\lambda)}_{\delta_{l\lambda}} \underbrace{l_m(\xi_\mu)}_{\delta_{m\mu}} \underbrace{l_n(\xi_\nu)}_{\delta_{n\nu}} \right) \psi_{ijk} \omega_\lambda \omega_\mu \omega_\nu \\ &= \frac{\partial}{\partial t} \sum_{\lambda,\mu,\nu=0}^N J(\boldsymbol{\xi}_{\lambda\mu\nu}) \hat{U}_{\lambda\mu\nu} \underbrace{l_l(\xi_\lambda)}_{\delta_{l\lambda}} \underbrace{l_m(\xi_\mu)}_{\delta_{m\mu}} \underbrace{l_n(\xi_\nu)}_{\delta_{n\nu}} \omega_\lambda \omega_\mu \omega_\nu = J(\boldsymbol{\xi}_{ijk}) \omega_i \omega_j \omega_k \frac{\partial \hat{U}_{ijk}}{\partial t}. \end{aligned} \quad (4.19)$$

The integration weights for the Gauss quadrature are ω . More details on the computation of ω are given, e.g., in the textbook of Kopriva [56] in the Secs. 1.11 and 3.2.

Volume integral

The volume integral is the third term on the right hand side of Eq. (4.10). The fluxes for the three coordinate directions d are treated separately by summing over the individual fluxes,

$$\int_{\mathcal{E}} \mathcal{F}(U) \cdot (\nabla_{\boldsymbol{\xi}} \phi) d\boldsymbol{\xi} = \sum_{d=1}^3 \int_{\mathcal{E}} \mathcal{F}^d(U) \cdot \frac{\partial \phi}{\partial \xi^d} d\boldsymbol{\xi}. \quad (4.20)$$

Subsequently, Eq. (4.20) is simplified in the same manner as the time derivative integral term in the preceding paragraph: The fluxes \mathcal{F} are approximated using Eq. (4.8), the test function is set to $\phi = \psi_{ijk}$, integrals are determined using the Gauss quadrature and the Lagrange property (4.14) leads to a cancellation of the majority of the summation terms. This is exemplified here for the first component of the flux \mathcal{F}^1 ,

$$\begin{aligned}
\int_{\mathcal{E}} \mathcal{F}^1(U) \cdot \frac{\partial \phi}{\partial \xi^1} d\xi &= \int_{\mathcal{E}} \left(\sum_{l,m,n=0}^N \hat{\mathcal{F}}_{lmn}^1 \psi_{lmn}(\xi) \right) \frac{\partial \phi_{ijk}}{\partial \xi^1} d\xi \\
&= \sum_{\lambda,\mu,\nu=0}^N \left(\sum_{l,m,n=0}^N \hat{\mathcal{F}}_{lmn}^1 \underbrace{l_l(\xi_\lambda^1)}_{\delta_{l\lambda}} \underbrace{l_m(\xi_\mu^2)}_{\delta_{m\mu}} \underbrace{l_n(\xi_\nu^3)}_{\delta_{n\nu}} \right) \frac{\partial \phi_{ijk}}{\partial \xi^1} \omega_\lambda \omega_\mu \omega_\nu \\
&= \sum_{\lambda,\mu,\nu=0}^N \hat{\mathcal{F}}_{\lambda\mu\nu}^1 \frac{dl_i}{d\xi} \Big|_{\xi=\xi^1} \underbrace{l_j(\xi_\mu^2)}_{\delta_{j\mu}} \underbrace{l_k(\xi_\nu^3)}_{\delta_{k\nu}} \omega_\lambda \omega_\mu \omega_\nu \\
&= \omega_j \omega_k \sum_{\lambda=0}^N \hat{\mathcal{F}}_{\lambda\mu\nu}^1 \frac{dl_i}{d\xi} \Big|_{\xi=\xi^1} \omega_i. \tag{4.21}
\end{aligned}$$

The derivative of the Lagrange coefficient l is generalised to

$$D_{ij} = \frac{dl_j(\xi)}{d\xi} \Big|_{\xi=\xi_i}. \tag{4.22}$$

The volume integral considering all three coordinate directions then reads

$$\begin{aligned}
\int_{\mathcal{E}} \mathcal{F}(U) \cdot (\nabla_\xi \phi) d\xi &= \omega_j \omega_k \sum_{\lambda=0}^N D_{i,\lambda} \hat{\mathcal{F}}_{\lambda j k}^1 \omega_\lambda + \omega_i \omega_k \sum_{\mu=0}^N D_{j,\mu} \hat{\mathcal{F}}_{i \mu k}^2 \omega_\mu + \\
&\quad \omega_i \omega_j \sum_{\nu=0}^N D_{k,\nu} \hat{\mathcal{F}}_{i j \nu}^3 \omega_\nu. \tag{4.23}
\end{aligned}$$

Surface integral

The second term in Eq. (4.10) describes the fluxes across DG element faces. The integrated fluxes for a hexahedral element read

$$\begin{aligned}
\int_{\partial \mathcal{E}} (\mathcal{F} \cdot \mathbf{N}) \phi dS &= \left[\int_{-1}^1 \int_{-1}^1 (\mathcal{F} \cdot \mathbf{N}) \phi d\xi^2 d\xi^3 \right]_{\xi^1=-1}^1 \\
&\quad + \left[\int_{-1}^1 \int_{-1}^1 (\mathcal{F} \cdot \mathbf{N}) \phi d\xi^1 d\xi^3 \right]_{\xi^2=-1}^1 \\
&\quad + \left[\int_{-1}^1 \int_{-1}^1 (\mathcal{F} \cdot \mathbf{N}) \phi d\xi^1 d\xi^2 \right]_{\xi^3=-1}^1. \tag{4.24}
\end{aligned}$$

Subsequently, the numerical approximation of these integrals is exemplified for the fluxes in the positive and negative ξ^1 -directions. In this case the unit normal vectors in reference space read $\mathbf{N}^\pm = \pm(1, 0, 0)^T$ and the flux can be simplified to

$\mathcal{F} \cdot \mathbf{N}^\pm = \pm \mathcal{F}^1$ at the respective element face. According to Eq. (4.8) the flux in reference space is expressed by the physical flux as

$$\pm \mathcal{F}^1 = \sum_{n=1}^3 Ja_n^1(\pm 1, \xi^2, \xi^3) F_n(\pm 1, \xi^2, \xi^3). \quad (4.25)$$

With the normal vector in physical space

$$\mathbf{n}_n^\pm = \frac{\pm Ja_n^1}{\hat{s}^\pm} \quad (4.26)$$

and the surface element

$$\hat{s}^\pm = \sqrt{\sum_{n=1}^3 (Ja_n^1(\pm 1, \xi^2, \xi^3))^2} \quad (4.27)$$

the flux becomes

$$\mathcal{F} \cdot \mathbf{N} = (\mathbf{F} \cdot \mathbf{n}^\pm) \hat{s}^\pm = (f(U^L, U^R, \mathbf{n}^\pm)) \hat{s}^\pm. \quad (4.28)$$

The physical flux \mathbf{F} needs to be evaluated at the face of a DG element. However, one central aspect of the DG approach is the discontinuity in the physical state at the element faces. Figure 4.2 illustrates this problem. On the basis of the Lagrange polynomials the fluid states are extrapolated to DG element faces. The Lagrange polynomials are independent for each DG cell and the left and right sided states U^L and U^R are in general not equal. Therefore, an approximated flux must be determined to guarantee the consistency of the surface integral among adjacent cells. The Riemann solvers described in Sec. 4.3 below approximate the fluxes depending on U^L , U^R and the normal vector \mathbf{n}^\pm . The resulting numerical flux is labelled $f(U^L, U^R, \mathbf{n}^\pm)$ and integrated over the element surface according to

$$f(\pm 1, \xi^2, \xi^3) \hat{s}^\pm = \sum_{j,k=0}^N [f \hat{s}]_{j,k}^{\pm \xi^1} l_j(\xi^2) l_k(\xi^3). \quad (4.29)$$

Inserting Eq. (4.28) into Eq. (4.24) yields in ξ^1 direction

$$\left[\int_{-1}^1 \int_{-1}^1 (\mathcal{F} \cdot \mathbf{N}) \phi d\xi^2 d\xi^3 \right]_{\xi^1=-1}^1 = \left[\int_{-1}^1 \int_{-1}^1 (f(U^L, U^R, \mathbf{n}^\pm)) \hat{s}^\pm \phi d\xi^2 d\xi^3 \right]_{\xi^1=-1}^1. \quad (4.30)$$

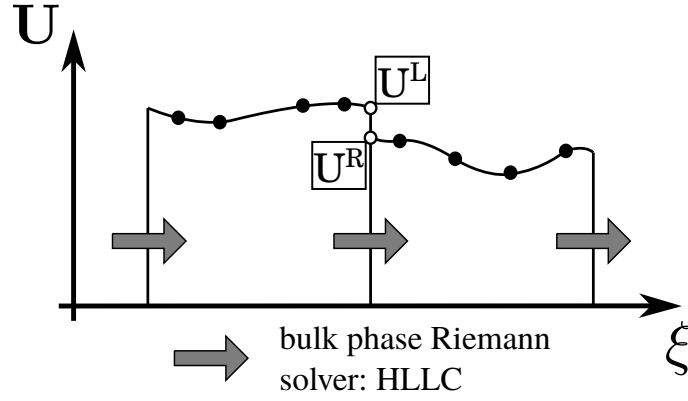


Figure 4.2: The extrapolation of the physical state U from the left and right cell to the common face yields the different states U^L and U^R , respectively.

As for the time derivative and volume integral, the use of the Gauss quadrature along with the Lagrange property (4.14) simplifies the resulting equation to

$$\begin{aligned}
 \text{Eq. (4.30)} &= \sum_{\mu,\nu=0}^N \left(\sum_{m,n=0}^N [f\hat{s}]_{m,n}^{+\xi^1} l_m(\xi_\mu^2) l_n(\xi_\nu^2) \right) l_i(1) l_j(\xi_\mu^2) l_k(\xi_\nu^3) \omega_\mu \omega_\nu \\
 &\quad - \sum_{\mu,\nu=0}^N \left(\sum_{m,n=0}^N [f\hat{s}]_{m,n}^{-\xi^1} l_m(\xi_\mu^2) l_n(\xi_\nu^2) \right) l_i(-1) l_j(\xi_\mu^2) l_k(\xi_\nu^3) \omega_\mu \omega_\nu \\
 &= \left([f\hat{s}]_{jk}^{+\xi^1} - [f\hat{s}]_{jk}^{-\xi^1} \right) \omega_j \omega_k.
 \end{aligned} \tag{4.31}$$

The extension to three space dimension gives

$$\begin{aligned}
 \int_{\partial\mathcal{E}} (\mathcal{F} \cdot \mathbf{N}) \phi dS &= \left([f\hat{s}]_{jk}^{+\xi^1} l_i(1) - [f\hat{s}]_{jk}^{-\xi^1} l_i(-1) \right) \omega_j \omega_k \\
 &\quad + \left([f\hat{s}]_{ik}^{+\xi^2} l_j(1) - [f\hat{s}]_{ik}^{-\xi^1} l_j(-1) \right) \omega_i \omega_k \\
 &\quad + \left([f\hat{s}]_{ij}^{+\xi^3} l_k(1) - [f\hat{s}]_{ij}^{-\xi^1} l_k(-1) \right) \omega_i \omega_j.
 \end{aligned} \tag{4.32}$$

Semi-discret formulation

The discrete formulations of the time derivative, volume and surface integrals, as given by Eqs. (4.19), (4.23) and (4.32) can be inserted into Eq. (4.10) to yield the semi-discret formulation of the DGSEM:

$$\begin{aligned}
\frac{\partial U_{ijk}}{\partial t} = & \left[\sum_{\lambda=0}^N \hat{D}_{i,\lambda} \hat{\mathcal{F}}_{\lambda jk}^1 \sum_{\mu=0}^N \hat{D}_{j,\mu} \hat{\mathcal{F}}_{i\mu k}^2 \sum_{\nu=0}^N \hat{D}_{k,\nu} \hat{\mathcal{F}}_{ij\nu}^3 \right. \\
& + \left([f\hat{s}]_{jk}^{+\xi^1} \hat{l}_i(1) - [f\hat{s}]_{jk}^{-\xi^1} \hat{l}_i(-1) \right) \\
& + \left([f\hat{s}]_{ik}^{+\xi^2} \hat{l}_j(1) - [f\hat{s}]_{ik}^{-\xi^2} \hat{l}_j(-1) \right) \\
& \left. + \left([f\hat{s}]_{ij}^{+\xi^3} \hat{l}_k(1) - [f\hat{s}]_{ij}^{-\xi^3} \hat{l}_k(-1) \right) \right]. \tag{4.33}
\end{aligned}$$

Here the one-dimensional operators

$$\hat{l}_i = \frac{l_i}{\omega_i}, \quad \hat{D}_{ij} = -\frac{\omega_i}{\omega_j} D_{ij} \tag{4.34}$$

are used. The discretisation of the time derivative term on the left hand side is outlined in Sec. 4.4.

4.2 Finite volume sub-cell approach

The interface between a liquid and a vapour is an obvious discontinuity within a flow field. While discontinuities can occur at DG element faces the polynomials within each DG element are continuous, see Figs. 4.1 and 4.2. If the interface moves between two nodes of the same DG element instabilities will occur in the numerical solution procedure. Alternatively, the interface can explicitly be restricted to lie between two DG elements. This would, however, significantly reduce the accuracy of the geometrical representation of the interface. Therefore the finite volume (FV) sub-cell approach of Sonntag [105, 106] is used in the present work. Figure 4.3 depicts the basic idea of this concept in one dimension. The DG element is sub-divided into multiple FV sub-cells if a discontinuity occurs. The number of FV sub-cells is equal to the number of polynomial nodes within a DG element. Sonntag developed this method to stabilize DG simulations with strong shock waves [105] and Fechter extended the scheme to two-phase flows [32, 34]. According to the nomenclature proposed by Sonntag [105] a FV sub-cell refers to one individual degree of freedom (DOF) within a DG element. An entire sub-divided DG element is called a FV element. In three dimensions a FV element consists of $(N + 1)^3$ individual FV sub-cells.

The discontinuous Galerkin scheme evaluates the integral balances of the conser-

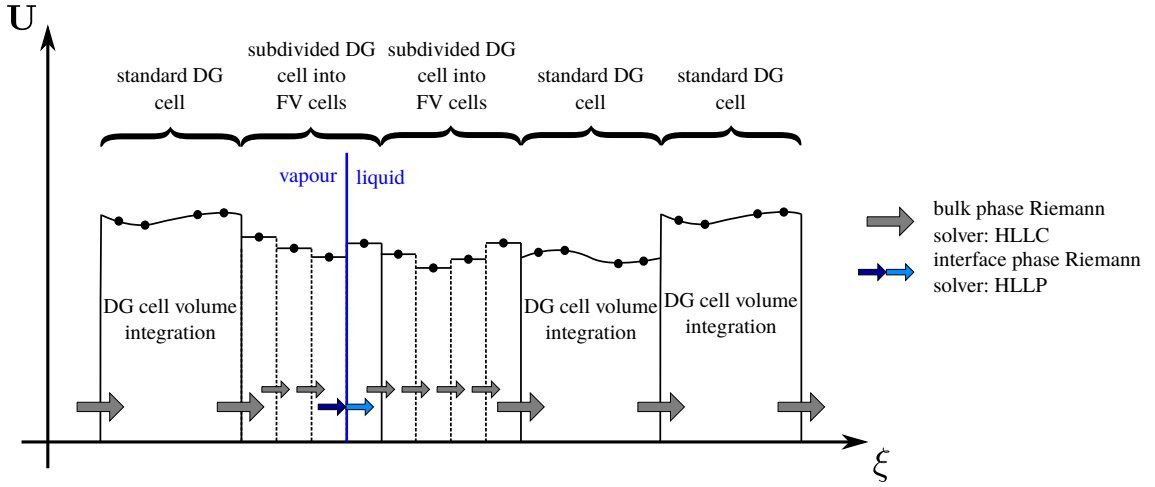


Figure 4.3: Discretization of a one-dimensional domain in the DG cells and a sub-cell resolution defined by a third order polynomial. Cells in the vicinity of the liquid-vapour interface are treated as FV cells.

vation laws for individual DG cells. The inner-cell resolution is accounted for by the test function ϕ . The FV sub-cell approach applies the integral balances separately to each polynomial node of a DG cell, i.e. to each individual DOF. The fluid state is constant within a FV sub-cell reducing the test function to $\phi = 1$. Therefore, the volume integral existing in the DG approach disappears and the integral balance for a single FV sub-cell \mathcal{SC} reduces to

$$\frac{\partial}{\partial t} \int_{\mathcal{SC}} JU d\xi + \int_{\partial \mathcal{SC}} (\mathcal{F} \cdot \mathbf{N}) dS = 0. \quad (4.35)$$

The change between the DG and the FV method is performed adaptively during the runtime of a computation. The numerical scheme switches when a predefined criteria is fulfilled. This is discussed later on in this section. The conservation of mass, momentum and energy must be enforced when the scheme switches between DG and FV. Therefore the condition

$$\int_{\mathcal{E}} U^{DG} d\xi = \int_{\mathcal{E}} U^{FV} d\xi = \sum_{i,j,k=0}^N \int_{\mathcal{SC}} U_{ijk}^{FV} d\xi \quad (4.36)$$

must be satisfied. In the general case the discret states U_{ijk}^{DG} and U_{ijk}^{FV} are not equal. Firstly, in the DG context the discrete values are the sampling points of a continuous polynomial while the states are constant within a FV sub-cell. Secondly, in the present work the FV sub-cells are distributed equidistantly within the FV element, while the sampling points follow a Gauss distribution in a DG element. Sonntag

[105] discussed routines that ensure the consistent interpolation between U_{ijk}^{DG} and U_{ijk}^{FV} with respect to Eq. (4.36). Subsequently, the semi-discrete formulation of the FV scheme is discussed. In contrast to traditional FV methods the FV element is here mapped to the reference space as discussed for the DG algorithm in Sec. 4.1. The approximated time derivative integral then reads

$$\frac{\partial}{\partial t} \int_{SC} JU d\xi = \Delta V_{ijk}^{\text{ref}} J_{ijk} \frac{\partial U_{ijk}}{\partial t} \quad (4.37)$$

with $\Delta V_{ijk}^{\text{ref}}$ being the volume of a FV sub-cell in reference space. The surface integral is

$$\begin{aligned} \int_{\partial\mathcal{E}} (\mathcal{F} \cdot \mathbf{N}) dS &= A_{jk}^{\text{ref}} \left(f_{i-\frac{1}{2},j,k}(U^L, U^R, \mathbf{N}) + f_{i+\frac{1}{2},j,k}(U^L, U^R, \mathbf{N}) \right) \\ &\quad A_{ik}^{\text{ref}} \left(f_{i,j-\frac{1}{2},k}(U^L, U^R, \mathbf{N}) + f_{i,j+\frac{1}{2},k}(U^L, U^R, \mathbf{N}) \right) \\ &\quad A_{ij}^{\text{ref}} \left(f_{i,j,k-\frac{1}{2}}(U^L, U^R, \mathbf{N}) + f_{i,j,k+\frac{1}{2}}(U^L, U^R, \mathbf{N}) \right) \end{aligned} \quad (4.38)$$

where A_{jk}^{ref} is the area of FV sub-cell face for the respective direction. The semi-discrete form of Eq. (4.35) is given by

$$\begin{aligned} \frac{\partial U_{ijk}}{\partial t} &= -\frac{1}{\Delta V_{ijk}^{\text{ref}} J_{ijk}} \left[A_{jk}^{\text{ref}} \left(f_{i-\frac{1}{2},j,k}(U^L, U^R, \mathbf{N}) + f_{i+\frac{1}{2},j,k}(U^L, U^R, \mathbf{N}) \right) \right. \\ &\quad A_{ik}^{\text{ref}} \left(f_{i,j-\frac{1}{2},k}(U^L, U^R, \mathbf{N}) + f_{i,j+\frac{1}{2},k}(U^L, U^R, \mathbf{N}) \right) \\ &\quad \left. A_{ij}^{\text{ref}} \left(f_{i,j,k-\frac{1}{2}}(U^L, U^R, \mathbf{N}) + f_{i,j,k+\frac{1}{2}}(U^L, U^R, \mathbf{N}) \right) \right]. \end{aligned} \quad (4.39)$$

The time derivative term on the left hand side is discretized using the algorithm in Sec. 4.4. As in the DG approach, the flux f depends on two generally discontinuous states U^L and U^R . In contrast to the DG scheme the face values are here not determined by an extrapolation of the polynomial. Instead, local gradients are reconstructed by finite differences. If a first order discretization is used the state of the FV sub-cell is simply copied to the respective sub-cell face. A second order discretization is obtained using limited central-difference gradients. For each sub-cell the gradient to the left and the right neighbor sub-cell is calculated and the minimum gradient is used to extrapolate the state from the sub-cell to the sub-cell face [105]. Central difference gradients cannot be reconstructed for cells next to the liquid-vapour interface, even though a minimum limiter is used. This is illustrated by the following example. A vaporising quiescent droplet has a high velocity on the vapour side and an (almost) zero velocity on the liquid side. The gradients in the

DG solver are built for the conservative variables. The momentum as a product of density and velocity may be similar across the interface (high velocity times low density vs. low velocity times high density). Therefore, the minimum limiter cannot directly be applied to interface cells. To achieve a second order discretization at the interface ghost states can be constructed as suggested by Aslam [5]. Here, the state of one fluid is extrapolated normal to the interface into the (auxilliary) cells of the other fluid. States are extrapolated by solving an additional differential equation. This has to be done independently for both fluids. Section 5.3.3 discusses the influence of the gradient approximation at the interface and within bulk FV sub-cells for the present computations.

4.2.1 Criteria to switch between DG and FV

The change from a DG element to a FV element or vice versa has to obey suitable rules. Here, indicators are determined for each element, and switching between DG and FV is enforced if the predefined upper or lower limits are exceeded or undercut. Sonntag [105] used indicator functions which analyse the smoothness of a solution. If the polynomial solution exhibits instabilities the indicator value \mathcal{I} increases. If \mathcal{I} exceeds the upper treshold \mathcal{I}_{\max} the numerical scheme switches from DG to FV. When the polynomial solution returns into a smooth state \mathcal{I} decreases and the DG scheme is used when $\mathcal{I} < \mathcal{I}_{\min}$. The condition $\mathcal{I}_{\min} < \mathcal{I}_{\max}$ avoids a frequent alternation between the DG and FV schemes [105]. One of these indicators was introduced by Persson and Peraire [77], and it is also used for the present work. Fechter [32] combined the indicator of Persson and Pareire to an indicator directly accounting for the location of the interface. Whenever the distance to the interface is below a predefined limit \mathcal{I} is explicitly set to a value higher than \mathcal{I}_{\max} to enforce FV elements near the liquid-vapour interface. The indicator in the present work is established on these indicators with the following modification and specification: The initial pressure jump in the present work is always between the liquid and the vapour. There are no shock fronts within an individual bulk phase at the start of a computation, but the high pressure ratio between liquid and vapour leads to a strong shock/rarefaction in the liquid and to a moderate shock/rarefaction in the vapour phase. The main test cases involve interactions of multiple vapour bubbles that lead to intense pressure wave dynamics within the liquid. In contrast, previous studies with the present solver investigated cases such as single droplets and shock tubes [32, 33, 34, 35, 36]. In these cases the liquid pressure relaxes more quickly than compared to the present setups. Therefore, the liquid elements are generally treated

with the FV scheme during this work. On the vapour side only those elements are treated as FV elements that contain the interface, that have an element face next to the interface or that exceed \mathcal{I}_{\max} due instabilities in the polynomial presentation of the pressure field.

4.3 Riemann solvers

In Secs. 4.1 and 4.2 the need to determine consistent fluxes across the DG element and FV sub-cell faces that separate discontinuous fluid states has been discussed. In the present work Riemann solvers are used to obtain the consistent flux \mathbf{f} from the neighbouring states U^L and U^R . Riemann solvers capture compressible effects such as shock or rarefaction waves. The basic idea is to treat the numerical discontinuity as an initial value problem. Different algorithms are required at single face element/cell faces and across the liquid vapour interface, respectively. In the present work the HLLC Riemann solver of Toro [111] and the HLLP Riemann solver of Fechter et al. [36] are used in the bulk phase and at the interface, respectively. Note that a modified HLLC Riemann solver exists also for two-phase problems without phase transition [33, 49]. If not stated otherwise, HLLC always refers to the single-phase Riemann solver in the present work. The Riemann solvers define fluxes normal to element/cell faces. The vectorial notation using the bold symbols \mathbf{U} and \mathbf{F} accounts here for the different conservation laws, see Sec. 3.1.

4.3.1 HLLC single phase Riemann solver

The basis for the HLLC Riemann solver is the approximate Riemann solver proposed by Harten, Lax and van Leer (HLL) [43]. The C refers to a *contact discontinuity* which is additionally resolved in the HLLC approach. This concept is illustrated in Fig. 4.4. The abscissa and the ordinate are a space and a time axis, respectively, and the initial discontinuity between \mathbf{U}^L and \mathbf{U}^R lies at $x = 0$. The diagonal lines represent signals which propagate away from the initial discontinuity as time passes. The sketch in Fig. 4.4 shows three such signals which are also called waves. Firstly, the left and the right waves are discussed. In the context of compressible fluid dynamics these waves are associated with shock and rarefaction waves evolving from pressure discontinuities. In the HLL approach the two outer waves enclose a constant state which can be considered as a relaxed pressure field between shock and rarefaction. In the HLLC approach an intermediate wave is resolved accounting

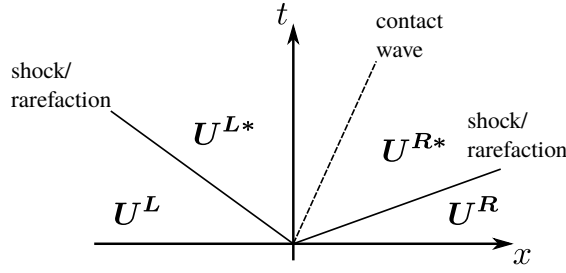


Figure 4.4: Riemann wave fan for the HLLC approximation according to Toro [111].

for contact or shear waves within a bulk phase [111]. In the framework of multi-component flows the contact wave describes the material interface between two fluids. The present work deals with single component two-phase flows and phase transition. Here, the contact wave may account for the discontinuity between fresh vapour and ambient gas. The intermediate states in Fig. 4.4 are approximated by

$$\mathbf{U}^{k*} = \rho^k \left(\frac{S^k - u^k}{S^k - S^*} \right) \begin{bmatrix} 1 \\ S^* \\ v^k \\ w^k \\ \frac{E^k}{\rho^k} + (S^* - u^k) \left[S^* + \frac{p^k}{\rho^k(S^* - u^k)} \right] \end{bmatrix} \quad (4.40)$$

with $k = L, R$ accounting for the left and right state, respectively. Auxilliary fluxes \mathbf{F}^{*k} are defined using the intermediate states \mathbf{U}^{k*} according to

$$\mathbf{F}^{*k} = \mathbf{F}^k + S^k(\mathbf{U}^{*k} - \mathbf{U}^k), \quad (4.41)$$

with the advective flux \mathbf{F}^k given by Eq. (3.4). The numerical flux \mathbf{f}^{HLLC} is then determined by

$$\mathbf{f}^{HLLC} = \begin{cases} \mathbf{F}^L & , \text{ if } 0 \leq S^L \\ \mathbf{F}^{*L} & , \text{ if } S^L \leq 0 \leq S^* \\ \mathbf{F}^{*R} & , \text{ if } S^* \leq 0 \leq S^R \\ \mathbf{F}^R & , \text{ if } S^R \leq 0. \end{cases} \quad (4.42)$$

The remaining unknowns are the signal velocities S^L , S^R and S^* that transport the different waves in Fig. 4.4. The outer wave speeds are characterised by the flow velocity and the speed of sound. The present work uses the Roe-eigenvalues [91]

$$S^L = \tilde{u} - \tilde{a}, \quad S^R = \tilde{u} + \tilde{a}. \quad (4.43)$$

The variables denoted $\tilde{\cdot}$ are the Roe-averages with the velocity given by

$$\tilde{u} = \frac{\sqrt{\rho^L}u^L + \sqrt{\rho^R}u^R}{\sqrt{\rho^L} + \sqrt{\rho^R}}. \quad (4.44)$$

The EOS determines the average speed of sound as a function of the average density and internal energy

$$\tilde{\rho} = \sqrt{\rho^L \rho^R} \quad \text{and} \quad \tilde{e} = \frac{\sqrt{\rho^L}e^L + \sqrt{\rho^R}e^R}{\sqrt{\rho^L} + \sqrt{\rho^R}}. \quad (4.45)$$

The velocity of the contact discontinuity is

$$S^* = \frac{p^R - p^L + \rho^L u^L (S^L - u^L) - \rho^R u^R (S^R - u^R)}{\rho^L (S^L - u^L) - \rho^R (S^R - u^R)}. \quad (4.46)$$

The text book „Riemann Solvers and Numerical Methods for Fluid Dynamics“ by Toro [111] provides a detailed derivation of these equations in Ch. 10.4.

4.3.2 HLLP two phase Riemann solver

Fechter et al. [36] introduced the HLLP two-phase Riemann solver which is also based on the ideas of Harten, Lax and van Leer [43]. In contrast to the HLLC Riemann solver it captures the phase transition (P) at a liquid-vapour interface. The following two paragraphs outline the general two-phase Riemann problem based on [35] and the simplifications of the HLLP algorithm introduced by [36], respectively.

Exact description of the two-phase Riemann problem with phase change

Figure 4.5(a) shows all relevant fluid states for the description of compressible fluid dynamics with vaporisation. The Riemann problem consists of the two initial and three intermediate states. They are separated by four waves. As in the HLLC Riemann problem the outer waves are shock or rarefaction waves propagating with S^L and S^R , respectively. The Rankine-Hugoniot conditions [111]

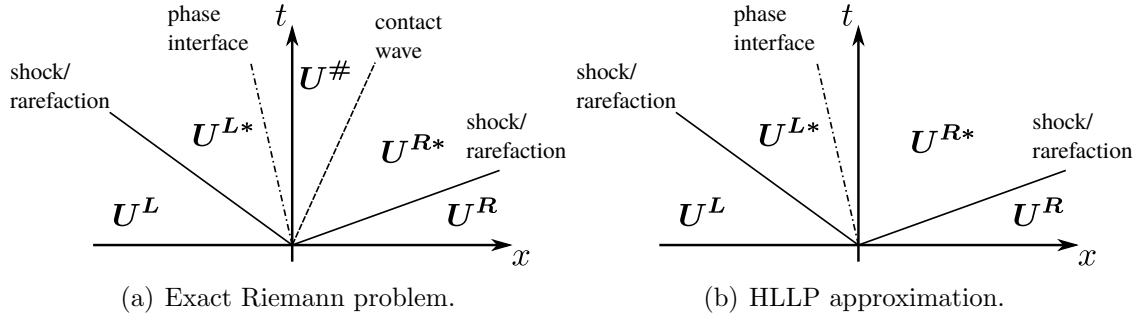


Figure 4.5: Riemann wave fans for two-phase problems with phase transition. Adapted from [36].

$$\begin{aligned}
 \rho^{k*} u^{k*} - \rho^k u^k &= S^k (\rho^{k*} - \rho^k) \\
 \rho^{k*} (u^{k*})^2 + p^{k*} - \rho^k (u^k)^2 - p^k &= S^k (\rho^{k*} u^{k*} - \rho^k u^k) \\
 (E^{k*} + p^{k*}) u^{k*} - (E^k + p^k) u^k &= S^k (\rho^{k*} E^{k*} - \rho^k E^k)
 \end{aligned} \tag{4.47}$$

couple the initial states with the star states. For the tangential velocity components $v^k = v^{k*}$ and $w^k = w^{k*}$ holds [111]. The phase interface separates the liquid from the vapour. It propagates with the interface velocity S_{int} . The jump conditions in Eq. (3.18) give the relation between the inner state $\mathbf{U}^\#$ (fresh vapour in case of vaporisation) and either \mathbf{U}^{L*} or \mathbf{U}^{R*} (the liquid state in case of vaporisation). The evaporative mass flux \dot{m}'' and the interface velocity are related by Eq. (3.10) using the states next to the phase interface. The contact wave separates the inner state $\mathbf{U}^\#$ (fresh vapour in case of vaporisation) and \mathbf{U}^{L*} or \mathbf{U}^{R*} (the vapour state in case of vaporisation). The Rankine-Hugoniot conditions (4.47) correlate these states. The following example shall illustrate the theoretical view given by Fig. 4.5(a) as well as relations (3.18) and (4.47) with a simple physical example:

- A liquid droplet is initially subcooled at state \mathbf{U}^L with $p^L \geq p_{\text{sat}}$
- The droplet is injected into a low-pressure environment at \mathbf{U}^R with $p^R < p_{\text{sat}}$
- A rarefaction wave will propagate from the liquid-vapour interface towards the center of the droplet. The signal velocity S^L is of the order of the speed of sound. The liquid pressure drops and the resulting rarefied liquid is superheated (\mathbf{U}^{L*} with $p^{L*} < p_{\text{sat}}$).
- The vapour becomes marginally compressed (\mathbf{U}^{R*} with $p^{R*} > p^R$) by a weak

shock wave. Again, the signal velocity S^R mainly depends on the speed of sound.

- Liquid vaporises at the phase interface generating fresh vapour at $\mathbf{U}^\#$.
- The liquid-vapour interface propagates with S_{int} due to vaporisation of liquid. As fresh vapour is continuously emitted from the interface the contact discontinuity between fresh vapour and compressed vapour propagates with S^* .

The exact Riemann problem is solved by 14 equations including

- Eq. (3.18) without both tangential momentum equations,
- Eq. (4.47) across the outer waves and the contact wave,
- Eq. (3.10) and one model equation from Sec. 3.3

for 14 unknowns ($\mathbf{v}^{L*} = (\rho^L, u^L, e^L)^T$, $\mathbf{v}^{R*} = (\rho^R, u^R, e^R)^T$, $\mathbf{v}^\# = (\rho^\#, u^\#, e^\#)^T$, S_L , S_R , S^* , S_{int} , \dot{m}'') [35]. Note that Fechter et al. [35, 36] neglect the diffusive terms in the jump conditions Eq. (3.18) and replace the jump in the heat flux by Eq. (3.17). Section 3.2 discusses the simplifications comprised in Eq. (3.17) which include the omission of the kinetic energy and a term of the form $\dot{m}'' u S_{\text{int}}$. These terms are negligible for the present work and the resulting jump conditions read

$$\begin{aligned} 0 &= \llbracket \rho(u_1 - S_{\text{int}}) \rrbracket, \\ \sigma\kappa &= \llbracket \rho u_1(u_1 - S_{\text{int}}) + p \rrbracket, \\ \sigma\kappa S_{\text{int}} &= \llbracket (\rho E)(u_1 - S_{\text{int}}) + p u_1 \rrbracket + \dot{m}'' h_{\text{fg}}. \end{aligned} \quad (4.48)$$

The models from Sec. 3.3 estimate the mass flux \dot{m}'' and h_{fg} is evaluated at $T_{\text{ref}} = 0.5(T_{\text{vap}} + T_{\text{liq}})$ from the EOS [35, 36]. Remember that the tangential velocity components are defined by $v^k = v^{k*}$ and $w^k = w^{k*}$ [111]. In principal, this equation system can be solved iteratively yielding the exact solution of the Riemann problem [35]. However, the computational cost is high. Therefore, Fechter et al. [36] reduced the complexity of the Riemann problem and provided a simplified solution algorithm as outlined now.

HLLP approximation for two-phase flows with phase change

Simplification 1 - Outer wave speeds S^L and S^R : The HLLP Riemann solver uses the same a priori estimation of the outer wave speeds S^L and S^R as the two-phase HLLC Riemann solver of Fechter et al. [33]. Firstly, the auxiliary states

$$\begin{aligned}
\Delta p &= p^R - p^L + \sigma\kappa, \\
\Delta u &= u^R - u^L, \\
\xi^L &= \frac{c^R \rho_R \Delta u - \Delta p}{c^L \left(c^R \frac{\rho^R}{\rho^L} + c^L \right)}, \quad \xi^R = \frac{c^L \rho_L \Delta u + \Delta p}{c^R \left(c^R + c^L \frac{\rho^R}{\rho^L} \right)}, \\
\tilde{\rho}^L &= \rho^L + \xi^L, \quad \tilde{\rho}^R = \rho^R + \xi^R, \\
\tilde{u}^L &= u^L - \frac{c^L}{\rho^L} \xi^L, \quad \tilde{u}^R = u^R + \frac{c^R}{\rho^R} \xi^R, \\
\tilde{p}^L &= p^L + (c^L)^2 \xi^L, \quad \tilde{p}^R = p^R + (c^R)^2 \xi^R
\end{aligned} \tag{4.49}$$

are determined. The corresponding speeds of sound \tilde{c}^L and \tilde{c}^R are obtained from the EOS (see 3.4 for details). The outer wave speeds are then estimated as

$$\begin{aligned}
S^L &= \min(u^L - c^L, \tilde{u}^L - \tilde{c}^L), \\
S^R &= \max(u^R + c^R, \tilde{u}^R + \tilde{c}^R).
\end{aligned} \tag{4.50}$$

This approximation formally reduces the number of unknowns by two. However, now the pressures p^{L*} and p^{R*} in Eq. (4.47) are thermodynamically inconsistent with ρ^{L*} , e^{L*} and ρ^{R*} , e^{R*} [35] because the corresponding signal velocities have been estimated a priori. Thus, the number of unknowns remains constant including now p^{L*} and p^{R*} as they are independent of \mathbf{U}^{L*} and \mathbf{U}^{R*} .

Simplification 2 - Omitting the contact discontinuity: The contact discontinuity is neglected and the state across the contact wave is averaged. This is similar to the HLL concept for single phase Riemann problems as proposed by Harten et al. [43]. Figure 4.5(b) depicts the resulting wave fan. This reduces the number of equations by three (Rankine Huginiot condition across the contact wave) while the number of unknowns is reduced by four ($\mathbf{U}^\#$, S^*). Thus, the remaining system of equations is overdetermined with 11 equations and 10 unknowns. A third simplification resolves this conflict.

Simplification 3 - Neglecting the energy coupling on the vapor side: The Rankine-Hugoniot condition is dropped for the internal energy on the vapour side. In cases with vaporisation, the energy e^{L*} will be mainly determined by the energy jump across the liquid-vapour interface and the influence of the initial internal energy e^L on e^{L*} is neglected [36]. The system of equations now consists of ten equations and ten unknowns. Fechter et al. [36] obtained analytical expressions for the internal states \mathbf{v}_L^* , \mathbf{v}_R^* as well as the pressures p_L^* and p_R^* from the software Maple[®]. These expressions are given in [36] and in Appendix B.

This Riemann solver can be solved explicitly or implicitly. The explicit solution uses the initial states \mathbf{U}^L and \mathbf{U}^R to determine the vaporisation mass flux \dot{m}'' , and the intermediate states can be calculated from the equations in Appendix B. For the implicit solution \dot{m}'' is determined from the intermediate states \mathbf{U}^{L*} and \mathbf{U}^{R*} . The initial states give a first estimation of \dot{m}'' and the intermediate states as well as the mass flux are then iterated until convergence is achieved. From the final intermediate states the numerical fluxes are calculated according to Eq. (4.41). In contrast to the HLLC Riemann solver the fluxes F^{L*} and F^{R*} are used individually for the left and the right cells, respectively.

4.4 Time discretization

For the numerical integration of the time derivatives, i.e. the left hand side of Eqs. (4.33) and (4.39), a third-order Runge Kutta scheme is used. Williamson [116] provided the theoretical background. The discrete equations evolving the initial solution \mathbf{U}^n at time step n to the new solution \mathbf{U}^{n+1} at time step $n + 1$ read

$$\begin{aligned}\tilde{\mathbf{U}} &= \mathbf{U}^n + 1/3\mathbf{U}_t^n \Delta t, \\ \tilde{\tilde{\mathbf{U}}} &= \tilde{\mathbf{U}} + 15/16\tilde{\mathbf{U}}_t \Delta t \quad \text{with} \quad \tilde{\mathbf{U}}_t = \mathbf{U}_t(\tilde{\mathbf{U}}) + 5/9\mathbf{U}_t^n, \\ \mathbf{U}^{n+1} &= \tilde{\tilde{\mathbf{U}}} + 8/15\tilde{\tilde{\mathbf{U}}}_t \Delta t \quad \text{with} \quad \tilde{\tilde{\mathbf{U}}}_t = \mathbf{U}_t(\tilde{\tilde{\mathbf{U}}}) + 153/128\tilde{\tilde{\mathbf{U}}}_t.\end{aligned}\tag{4.51}$$

The adaptive time step Δt is determined based on the *CFL* criterion by Courant, Friedrichs and Lewy [25] for the convective terms of the conservation laws. Similarly, a *DFL* number is used within the DG solver to account for the diffusive terms. The

convective and viscous eigenvalues,

$$\lambda_{\text{con}} = \max \left(\frac{(|\mathbf{u}| + c)}{\Delta x} \right) \quad (4.52)$$

and

$$\lambda_{\text{dif}} = \max \left(\frac{a}{\Delta x^2} \right), \quad (4.53)$$

determine the size of the time step. Here, a and Δx are the thermal diffusivity and the size of the DG element, respectively. The maximum function considers all DG elements of the computational domain. The minimum of the convective and diffusive time steps,

$$\Delta t_{\text{con}} = \frac{CFL\alpha_{RK}(N)}{\lambda_{\text{con}}(2N + 1)} \quad (4.54)$$

and

$$\Delta t_{\text{dif}} = \frac{DFL\beta_{RK}(N)}{\lambda_{\text{dif}}(2N + 1)^2}, \quad (4.55)$$

is used for the computation. The factors $(2N + 1)$ and $(2N + 1)^2$ account for the non-equidistant inner cell resolution of a DG element. α_{RK} and β_{RK} are scaling parameters which depend on the polynomial degree N and the order of the time integration.

CHAPTER 5

Determination of reference conditions

This chapter contains results of a series of code validations, parameter and model studies that help to set up and analyse the main test cases presented in Chs. 6 and 7. Section 5.1 discusses some of the essential properties of the HLLP Riemann solver and compressible liquid-vapour flows. The role of vapour bubble growth for the disintegration of flashing jets and the complexity of nucleation and bubble interaction was discussed in Sec. 2.3. In contrast, single bubble growth is a relatively simple and well defined test case. Here, it serves as a reference case used to understand the basic physical mechanisms, to estimate length and time scales for bubble growth in cryogenic LOX and to validate the solver for the DNS of multiple bubbles. In Sec. 5.2 the general physical aspects are summarised and a semi-analytical model for single bubble growth is used to generate a reference data base. This semi-analytical solution is used to validate the DNS solver and calibrate the vaporisation models. Section 5.3 studies the sensitivity of the DNS results to the numerical parameters.

5.1 Vaporisation modeling with the HLLP Riemann solver

In the following section the vaporisation of LOX in a shock tube is investigated. This one-dimensional test case allows to analyse the properties of the HLLP Riemann solver and to illustrate some characteristics of compressible two-phase flows at a moderate computational cost. Sections 5.1.1 and 5.1.2 present the test setup and the corresponding results, respectively.

5.1.1 Setup shock tube

Figure 5.1 outlines the geometrical setup and the physical configuration of the shock tube. Here, this shock tube is closed at one end and opened at the other end. The left half of the domain is filled with saturated liquid (state A in Subfig. 5.1(b)), the right half is filled with superheated vapour (state B in Subfig. 5.1(b)). The initial temperature is the same in both phases. The initial pressure of the vapour p_{vap} on the right side is therefore less than the liquid pressure p_{liq} . Table 5.1 provides the physical initial conditions for both phases. A symmetry condition and an outflow condition are prescribed to the left and right domain boundary, respectively. Table 5.2 summarises the physical models and the numerical parameters applied for the present test case. The Hertz-Knudsen relation (HKR) introduced in Sec. 3.3 estimates the vaporisation mass flux and the coefficients are arbitrarily set to $\lambda_{\text{vap}} = \lambda_{\text{cond}} = 0.5$. The results of this test case are used here for a qualitative analysis and a precise calibration of λ_{vap} and λ_{cond} is therefore not needed. For the quantitative analysis of multiple vapour bubbles a detailed calibration of the coefficient follows in Ch. 6. For the same reason all other parameters given in Tab. 5.2 remain unchanged for the shock tube test case.

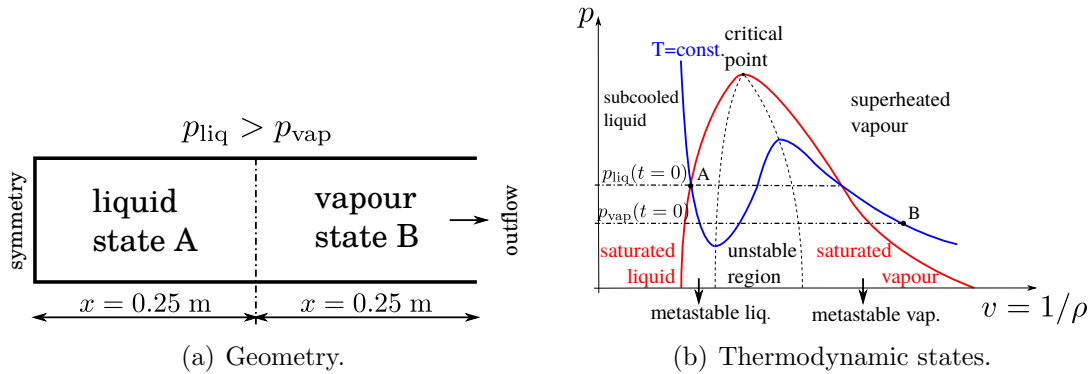


Figure 5.1: Configuration of a shock tube test case with one open end.

Table 5.1: Initial conditions for the shock tube test case.

state	density ρ in $[\text{kg}/\text{m}^3]$	pressure p in $[\text{bar}]$	temperature T in $[\text{K}]$
A	976.336	10	120
B	17.378	5	120

Table 5.2: Default numerical parameters and physical models for the shock tube test case.

parameter	value	comment
Vaporisation model	HKR	Sec. 3.3
$\lambda_{\text{vap}}, \lambda_{\text{cond}}$	0.5	arbitrary
EOS	CoolProp	
DG cells, N_{poly}	50, 3	
FV order, IF order, CFL	2, 2, 0.9	

5.1.2 Results shock tube

Figure 5.2 shows the density, pressure, velocity and temperature field after $t = 0.2$ ms. The density profile in Subfig. 5.2(a) shows that the position of the liquid-vapour interface has not changed. The amount of vaporised liquid after $t = 0.2$ ms is too small to considerably reduce the liquid volume after the rather short time interval. The increase in the vapour density at the interface results from a shock wave as indicated by the pressure field in Subfig. 5.2(b). The initial pressure difference causes shock and rarefaction waves propagating through the vapour and liquid phases, respectively. The propagation speed of these waves is estimated by Eq. (4.50) and for the present test case mainly determined by the speed of sound, c . For the present operating conditions, the speed of sound of the liquid and the vapour is $c_{\text{liq}} = 642$ m/s and $c_{\text{vap}} = 201$ m/s, respectively. Thus, the rarefaction wave in the liquid has propagated further away from the interface than the shock wave in the vapour. The pressure field at $t = 0.2$ ms also allows to identify the different states in the Riemann wave fan as it is depicted for the HLLP approximation in Fig. 4.5(b). The initial states $\mathbf{U}^L = \mathbf{U}_{\text{liq}}$ and $\mathbf{U}^R = \mathbf{U}_{\text{vap}}$ are still present at the left and right sides of the domain, respectively. The rarefaction wave and the interface enclose the rarefied liquid of state \mathbf{U}^{L*} . The compressed vapour is represented by the state \mathbf{U}^{R*} between the interface and the shock wave. Subfigure 5.2(c) shows the velocity field. The shock wave accelerates the vapour and the fluid velocity $u_{\text{vap}} \approx 22$ m/s is maintained by the vaporisation from the interface. The small velocity on the liquid side accounts for the expansion of the liquid by the rarefaction wave. The temperature profile in Subfig. 5.2(d) illustrates three effects. Firstly, the liquid temperature slightly cools down. This is the consequence of the expansion rather than of the latent heat of vaporisation. Secondly, the vapour temperature increases because the shock wave compresses the fluid. The third important aspect is the

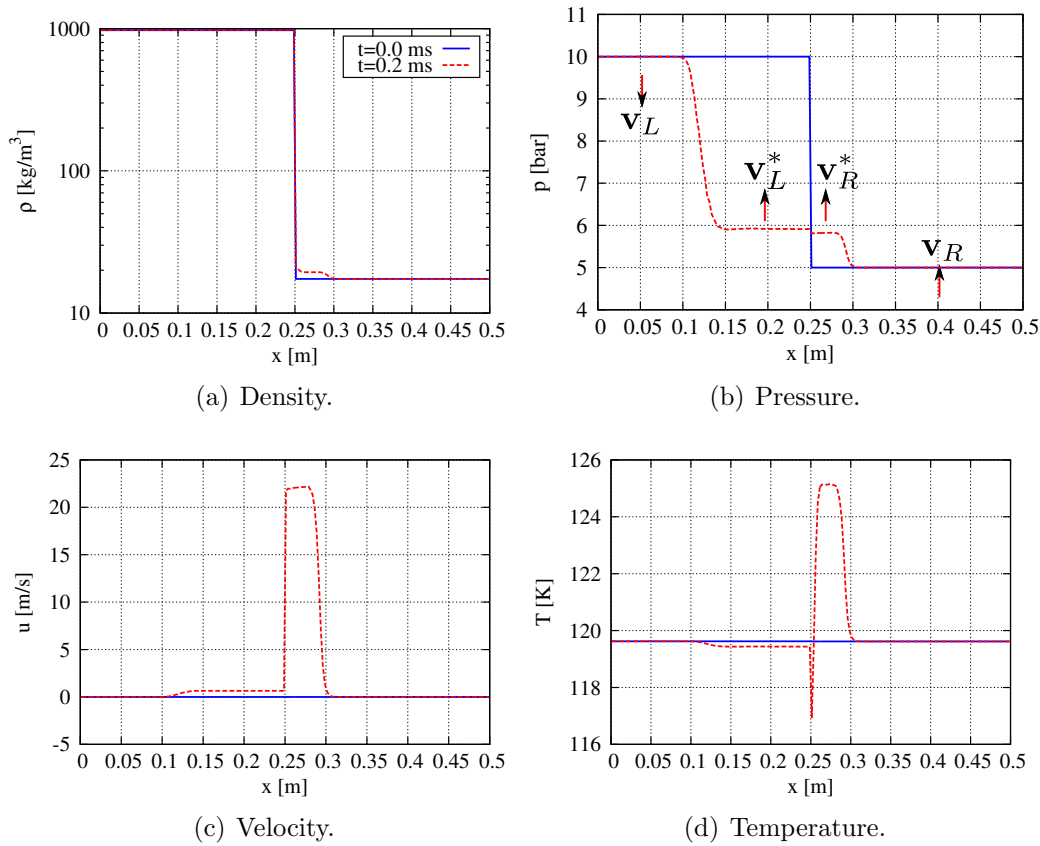


Figure 5.2: Solid lines: initial conditions of the shock tube. Dashed lines: results after $t = 0.2$ ms.

temperature drop to $T \approx 117$ K close to the interface. It occurs on the vapour side and it is not associated with the latent heat of vaporisation. Figure 5.3 shows the temperature profile after $t = 5.0$ ms which gives a better illustration of this effect. The temperature drop has propagated towards the vapour with the flow velocity of the fresh vapour. This is confirmed estimating the propagated distance using the vapour velocity near the interface with $\Delta x_{\text{dist}} \approx 22 \text{ m/s} \cdot 5 \cdot 10^{-3} \text{ s} = 0.11 \text{ m}$. Figure 5.3 shows that the low temperature zone in the vapour ranges to $x \approx 0.35$ m being approximately the distance to the interface at $x \approx 0.25$ m. The temperature jump at $x \approx 0.35$ is associated with the contact discontinuity in the exact Riemann problem. The states \mathbf{U}^{L*} , $\mathbf{U}^\#$ and \mathbf{U}^{R*} as introduced in Fig. 4.5(a) can also be identified in Fig. 5.3. The contact discontinuity separates the fresh vapour from the compressed surrounding gas. Even though the HLLP approximation neglects this jump the use of the HLLC Riemann solver in the bulk phase allows to account also for the contact discontinuity.

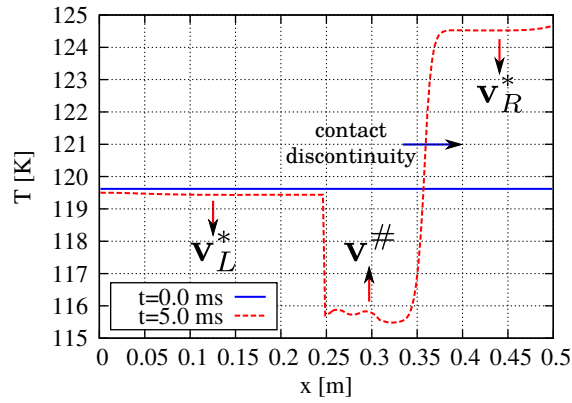
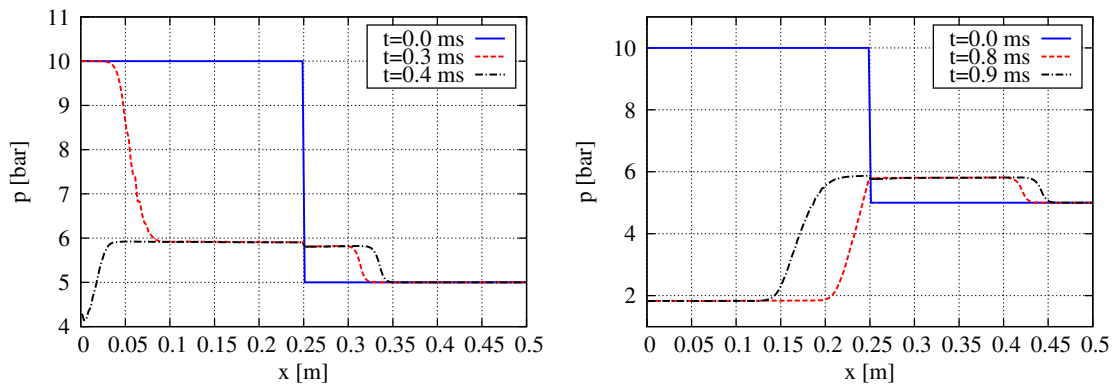


Figure 5.3: Solid line: initial temperature field of the shock tube. Dashed lines: temperature after $t = 5.0$ ms.

Figure 5.4 illustrates the characteristic behaviour of pressure waves in liquids. Subfigure 5.4(a) shows the reflection of the initial rarefaction wave at the symmetry plane on the left side of the domain. The pressure behind the rarefaction decreases by the reflection and the wave propagates back towards the interface. The reflection at the interface is depicted in Subfig. 5.4(b). The pressure wave is inverted from a rarefaction to a shock wave. The pressure behind the shock is approximately the same as the pressure before the previous rarefaction. Similar to the pressure decrease after the reflection of the rarefaction at the symmetry, the shock wave reflection increases the pressure behind the shock after it is reflected (not shown here). Over time the pressure will relax towards the ambient pressure. Figure 5.5 depicts results at late time intervals. The density profiles in Subfig. 5.5(a) indicate that an appreciable amount of liquid is vaporised within the time interval



(a) Pressure wave reflection at the symmetry plane. (b) Pressure wave reflection at the interface.

Figure 5.4: Pressure wave propagation in the liquid phase.

considered. The liquid pressure is approximately the same as the vapour pressure and the remaining pressure waves are of a small amplitude only. Subfigure 5.5(c) shows that the liquid velocity has relaxed to zero and that the vapour velocity remains constant during the vaporisation process.

The energy jump condition in Eq. (4.48) omits the heat fluxes across the interface but couples the liquid and vapour energy by the source term $\dot{m}''h_{fg}$, see Sec. 4.3.2. Therefore, the cooling of the liquid due to the latent heat of vaporisation is not accounted for by the HLLP Riemann solver. This is also seen in the temperature fields in Fig. 5.5(d). Here, the liquid remains superheated at a constant temperature. Consequently, the mass flux at the interface converges, see Fig. 5.6. Although the temperature of the generated vapour is lower than the temperature of the superheated liquid, the specific enthalpy is higher in the vapour phase. The energy needed to increase the enthalpy actually comes from the superheated liquid, the liquid cools down and energy is conserved. The cooling of the liquid at the interface is, however, not resolved in the HLLP Riemann solver and the energy conservation is violated. To analyse the conservation property of the solver the total mass and the total energy are determined by

$$m_{\text{tot}}(t) = \int_V \rho dV + \int_0^t \rho u A dt \quad (5.1)$$

$$(5.2)$$

and

$$E_{\text{tot}}(t) = \int_V \rho \left(e + \frac{u^2}{2} \right) dV + \int_0^t \rho \left(e + \frac{u^2}{2} \right) u A dt, \quad (5.3)$$

respectively. In both equations the first term on the right hand side represents the volume integral of the conservative quantities within the domain. The second term on the right hand side accounts for the fluid that has crossed the control surface surrounding the domain. Figure 5.7 depicts the results for the shock tube. The total mass represented by the solid line is conserved throughout the vaporisation. The total energy increases instead because the evaporative cooling is not resolved. In the present example 95% of the liquid vaporises within the time interval of $t = 0.5$ s. Therefore, the rise in the total energy is relatively high. The energy reservoir

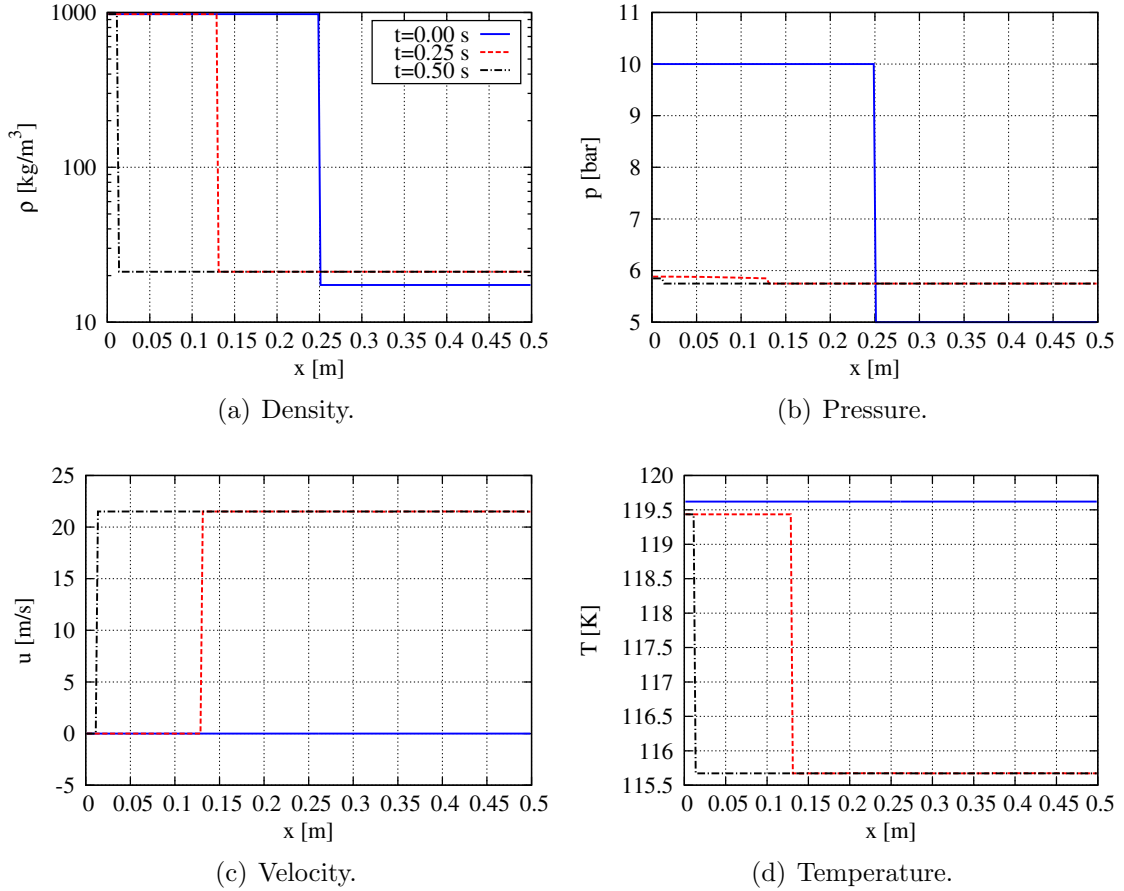


Figure 5.5: Results for the shock tube when a considerable amount of mass has vaporised.

allowing to vaporise the liquid is solely the superheated liquid itself and the liquid temperature would therefore continuously decrease during the vaporisation process. Reducing the energy of the remaining liquid at $t = 0.5$ s by the energy difference $\Delta E = E_{\text{tot}}(t = 0.5 \text{ s}) - E_{\text{tot}}(t = 0)$ would reduce the liquid temperature to unphysically low ranges. Accounting for the liquid cooling during the entire vaporisation process would result in a decreasing mass flux and less liquid would vaporise in total. On a macroscopic level the cooling of the liquid will only become important at reasonably long time intervals. If, however, time intervals are small, the change of the mean temperature of the liquid bulk is negligible. In the case of vapour bubble growth a relatively small amount of vaporised liquid leads to large volumetric increase in the bubble radii. The energy rise is less significant for the simulation of vapour bubble growth within the time intervals considered in the present work. This is discussed in Sec. 5.3.6.

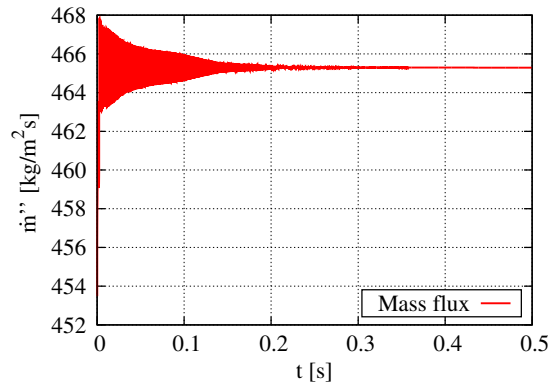


Figure 5.6: Mass flux over time for the shock tube test case.

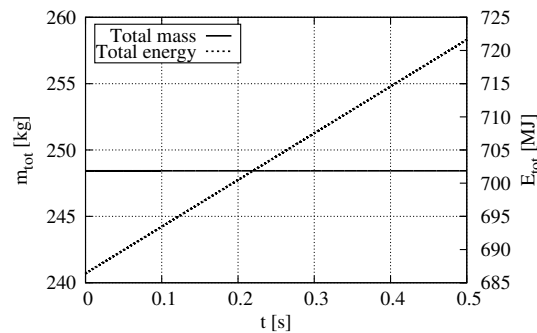


Figure 5.7: Mass flux over time for shock tube.

5.2 Generation of a reference data base

The previous test case is well suited to characterise some of the fundamental physical effects of compressible two-phase flows with vaporisation and the representation of these effects using the HLLP Riemann solver. In the next step, the growth of isolated vapour bubbles is investigated because it is more closely related to flash boiling. It is important to point out that the studies of the present section are conducted with a semi-analytical model that is independent from the DG solver. This model is based on the Rayleigh-Plesset equation [80, 85] and referred to as RPE solver in the remainder of this work. Here, it serves as a reference solution for the validation and calibration of the DG solver in the further course of the investigations. Therefore, in this section a data base for comparison is generated which is based on the RPE solver.

5.2.1 Physical aspects of single vapour bubble growth

Some aspects of bubble nucleation were introduced in Sec. 2.1.2 and further detail on their subsequent growth is given here. Figure 5.8 illustrates the common assumptions for single vapour bubble growth [82, 90]. The surrounding liquid is superheated, i.e. it is below its saturation pressure at a metastable state B and vapour bubbles nucleate under saturation pressure (see also Fig. 2.3). The latter condition was introduced in Sec. 2.1.2 as a simplification of Eq. (2.4). The error associated with this simplification is smaller than 4% for the present operating conditions suggesting that $p_{\text{vap}} = p_{\text{sat}}(T_{\infty})$ is a reasonable assumption.

The surface tension force balances the pressure difference between vapour and liquid leading to a mechanical equilibrium. An isothermal nucleation defines the thermodynamic limit for a bubble of *critical radius* [14]

$$R_{\text{crit}} = \frac{2\sigma}{p_{\text{sat}}(T_{\infty}) - p_{\text{liq}}}. \quad (5.4)$$

Tiny fluctuations overcome the mechanical equilibrium and the bubble grows initially at an extremely low rate. After the initial delay, the bubble grows at high rates driven by the inertia of the liquid. The heat required for the vaporisation of the liquid cools down the interface, and the vapour pressure as well as the growth rate decrease. This process is indicated in Fig. 5.8 by the path from state C to state D on the vapour side. A thin boundary layer develops from the bubble wall towards the liquid, the vapour pressure approaches the ambient pressure and heat conduction drives the bubble growth.

5.2.2 Reference model

The growth of single vapour bubbles has excessively been investigated and reliable analytical and semi-analytical solutions for determining the bubble radius and its growth rate exist [14, 62, 69, 79, 80, 81, 82, 85, 90]. These models use an integration of the Navier-Stokes equations (momentum conservation) from the bubble wall to infinity using assumptions of spherical symmetry. Plesset [78, 79] extended the early work of Rayleigh [85] to the Rayleigh-Plesset equation (RPE)

$$R\ddot{R} + \frac{3}{2}(\dot{R})^2 = \frac{1}{\rho_{\text{liq}}}(p_{\text{sat}} - p_{\infty} - \frac{2\sigma}{R} - \frac{4\mu}{R}\dot{R}) \quad (5.5)$$

for single bubble growth. Here, R , \dot{R} and \ddot{R} are the bubble radius and its first and second time derivative, respectively. A derivation according to Brennen [14] is given in Appendix C. Solving Eq. (5.5) provides the temporal evolution of the bubble radius R and its derived quantities (growth velocity, acceleration). Equation (5.5) holds for the inertia controlled regime and includes the surface tension force and the viscous forces. Lee and Merte [62] coupled the RPE to the temperature equation

$$\frac{\partial T}{\partial t} + u_r \frac{\partial T}{\partial r} = a \left(\frac{\partial^2 T}{\partial r^2} + \frac{2}{r} \frac{\partial T}{\partial r} \right) \quad (5.6)$$

and derived suitable boundary conditions at the bubble wall from Eq. (3.22). Equations (5.5) and (5.6) provide a relatively simple, one-dimensional integrable solution [62], they account for the inertia and the heat diffusion driven stages of bubble growth and can thus serve as a reference for the DNS code development. The solution algorithm is adapted from Lee and Merte [62]. In the present work an implicit Euler scheme is used to discretise Eq. (5.5). Equation (5.6) is discretised in a thin liquid band which captures the thermal boundary layer at the interface. The resulting equation system is solved iteratively until the temperature field converges.

The Rayleigh-Plesset equation [79, 85] and its coupling to the temperature equation by Lee and Merte [62] describe the growth of isolated bubbles using several assumptions that warrant some further discussion:

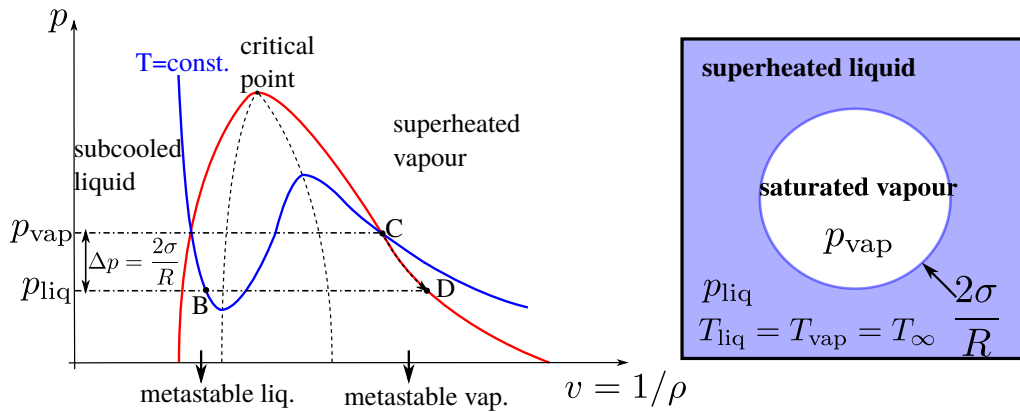


Figure 5.8: Initial conditions for the present setup. State B indicates a metastable superheated liquid. State C indicates a vapour bubble which nucleates within the liquid. We assume an isothermal nucleation with the vapour bubble being saturated. The resulting pressure gap is balanced by the surface tension.

1. The system consists of a spherical bubble in an infinite liquid reservoir: This assumption allows to employ radial symmetry for the solution of bubble expansion. In a truly flashing liquid multiple bubbles occur and the bubble density is typically high. The bubbles may therefore interact with their neighbour and deviate from sphericity. The present study, however, considers isolated bubbles in a sufficiently extended liquid environment only and the fluid properties need to be selected with respect to the ambient conditions (i.e. pressure and temperature) typical for flash boiling of cryogenic oxygen. Multiple bubble arrangements will be discussed in Ch. 7.
2. The vapour in the bubble is saturated and in thermodynamic equilibrium with the liquid at the interface: If the growth rate of the bubble exceeds the rate at which vapour can be generated, the bubble pressure drops below the saturation pressure [79, 80]. An estimation of the maximum rate of vapour generation is difficult because the accommodation coefficients of the underlying kinetic model are in general not known [81]. Shusser et al. [104] gave an example for an extension of the Rayleigh-Plesset equation incorporating a kinetic model for phase transfer rates and nonequilibrium effects are briefly addressed in [81]. Up to today, uncertainties in the estimation of these nonequilibrium effects at the interface persist and the present work therefore assumes processes at molecular scale to be much faster than macroscopic processes such as bubble expansion and uses the common equilibrium assumption.
3. The vapour pressure inside the bubble is constant and the liquid is incompressible: The growth velocities of the isolated bubbles in this work do not exceed 20 m/s and are therefore considerably smaller than the speed of sound in the vapour. It is valid to assume that the bubble pressure instantaneously follows the pressure at the bubble wall [80]. The speed of sound of the liquid oxygen is larger than 640 m/s for the present operating conditions confirming the assumption of an incompressible liquid phase.

It is emphasized here, that the approximation of Lee and Merte [62] is in general not restricted to certain regimes of bubble growth. Plesset and Zwick [80] derived an analytical model for the heat diffusion controlled stage taking into account the evaporative cooling. This model is, however, valid for thin boundary layers only. The procedure of Lee and Merte resolves the temperature field and assumptions regarding the boundary layer thickness are not needed. Up to today, the Rayleigh-Plesset equation is a common reference for the understanding and the quantification of the

growth process in the context of flash boiling [8, 102] and it is deemed reasonable to use the implementation by Lee and Merte [62] for the present investigation.

5.2.3 Physical conditions

Experiments on flash boiling of LOX are currently conducted at the German Aerospace Centre (DLR) in Lampoldshausen and first results have been presented by Lamanna et al. [58]. The temperature of the cryogenic oxygen ranges from $T = 90$ K to $T = 120$ K and the same range is covered here. The superheat ratio R_p defined by Eq. (2.5) specifies the pressure conditions for the liquid and the vapour at a given temperature. Table 5.3 lists the initial conditions of the different test cases that span the entire temperature range and provide conditions from very moderate to high superheat. Cases are labeled CX-Y with X and Y being the superheat ratio R_p and the initial temperature, respectively (e.g. C5-120 for $R_p = 5$ and $T_0 = 120$ K). Single bubble growth is typically characterized by the Jakob number Ja

Table 5.3: Initial conditions for bubble growth parametric study. Densities are given in $[\text{kg}/\text{m}^3]$, pressures are given in $[\text{bar}]$, critical radii in $[\mu\text{m}]$ and temperatures in $[\text{K}]$. The Jakob number Ja is dimensionless.

		$R_p = 5$	$R_p = 10$	$R_p = 50$	$R_p = 100$
$T_\infty = 90.0$ $p_{\text{sat}} = 0.994,$ $\rho_{\text{vap}} = 4.39$	p_{liq}	0.199	0.099	0.02	0.01
	ρ_{liq}	1141.927	1141.905	1141.887	1141.885
	R_{crit}	0.332	0.295	0.271	0.268
	Ja	117.545	298.334	1965.017	4185.898
$T_\infty = 100.0$ $p_{\text{sat}} = 2.54,$ $\rho_{\text{vap}} = 10.425$	p_{liq}	0.508	0.254	0.051	0.025
	ρ_{liq}	1090.303	1090.230	1090.171	1090.164
	R_{crit}	0.332	0.295	0.271	0.268
	Ja	62.883	158.303	1022.836	2162.338
$T_\infty = 110.0$ $p_{\text{sat}} = 5.434,$ $\rho_{\text{vap}} = 21.281$	p_{liq}	1.087	0.543	0.109	0.054
	ρ_{liq}	1033.779	1033.566	1033.395	1033.374
	R_{crit}	0.039	0.034	0.031	0.031
	Ja	39.698	99.442	632.984	1329.518
$T_\infty = 120.0$ $p_{\text{sat}} = 10.0223,$ $\rho_{\text{vap}} = 39.308$	p_{liq}	2.045	1.022	0.204	0.102
	ρ_{liq}	969.208	968.612	968.133	968.073
	R_{crit}	0.015	0.013	0.012	0.012
	Ja	28.780	72.016	453.795	948.112

$$Ja = \frac{\rho_{\text{liq}} c_{p,\text{liq}} (T_{\infty} - T_{\text{sat}}(p_{\infty}))}{\rho_{\text{sat,vap}}(p_{\infty}) h_{\text{fg}}}. \quad (5.7)$$

It measures the degree of superheat as the ratio between the heat stored in the liquid and the latent heat needed for vaporisation [81]. The present parameter study is based on the pressure ratio R_p instead, because it is one important key parameter in flash boiling (e.g. [59]). Table 5.3 lists the corresponding Ja used for the evaluation of the DNS results in Sec. 6.1.

5.2.4 Results of the reference model and conclusions for the DNS of vapour bubbles

In this section the reference model described in 5.2.2 is evaluated using the operation conditions given in Sec. 5.2.3. The relevant time frame should cover the growth process until bubbles merge in a superheated LOX jet. This, however, is generally not known a priori, it depends on the bubble density and therefore on the nucleation rate. Here, a time interval of 100 microseconds is considered. Figure 5.9 depicts the bubble radii for different temperatures T_{∞} and different pressure ratios R_p . The bubble sizes at $t = 100 \mu\text{s}$ are larger than 100 micrometer. For reasonably high nucleation rates a jet disintegration is likely to occur within this growth interval. Only for low nucleation rates the time range needs to be extended further. The three stages of bubble growth - initial delay, inertia controlled growth and heat diffusion controlled growth - can be characterised in Subfig. 5.9(a). During the initial stage the bubble radii do not change. Once the disturbance is large enough bubbles rapidly grow and inertia forces control the growth rate. During this stage the growth rate typically increases with increasing T_{∞} . The bubble surface is accelerated by the pressure force (first term on the right hand side of Eq. (5.5)) which rises with increasing saturation pressure and therefore with increasing temperature. At later times, C5-120 grows more slowly than the C5-90 because the former reached the heat diffusion controlled stage while the latter is still inertia controlled. For $R_p = 100$ all cases remain inertia controlled and therefore C100-120 keeps higher growth rates up to $t = 100 \mu\text{s}$, see Subfig. 5.9(b).

Subfigure 5.10(a) depicts the liquid temperature profiles for different initial temperatures with a superheat ratio $R_p = 100$ at the final simulation time. The bubble surface lies at $r - R = 0$ and its decreased temperature T_{int} is a consequence of the

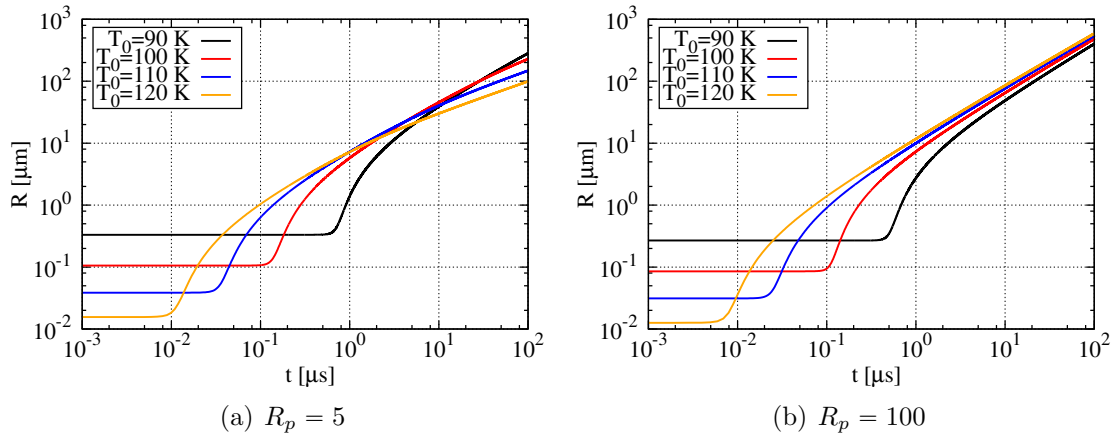


Figure 5.9: Bubble radius over time for different temperatures

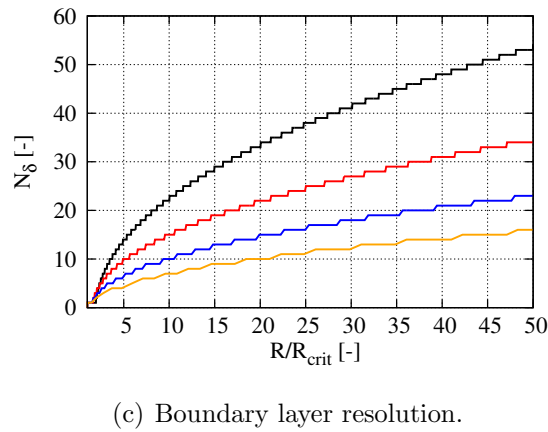
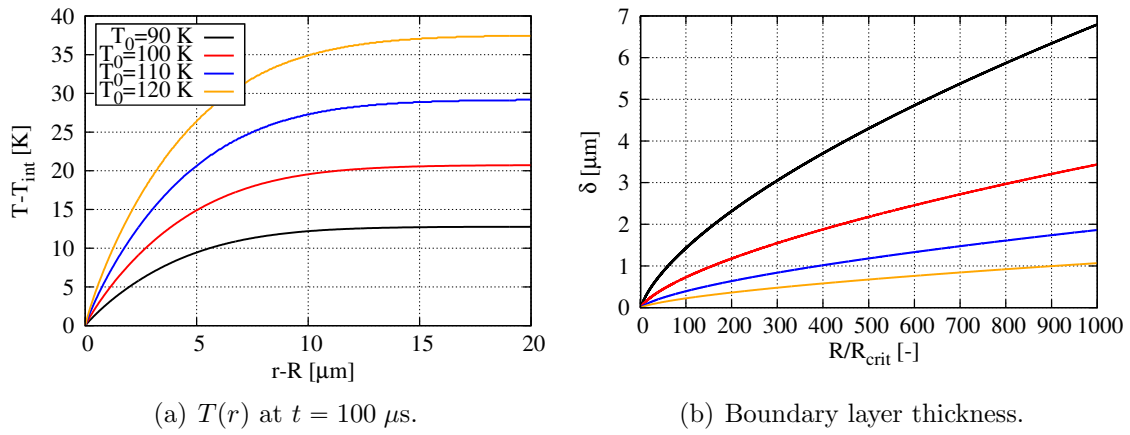


Figure 5.10: Thickness and resolution of the boundary layer for different temperatures and $R_p = 100$.

latent heat of vaporisation. The boundary layer to the bulk liquid with $T > T_{\text{int}}$ is of the order of $\delta = 10 \mu\text{m}$. Subfigure 5.10(b) shows the boundary layer thickness during the growth up to 1000 times R_{crit} . Within this growth interval δ does not exceed 7 micrometer and a good resolution must be ensured, in particular for the early stages. Subfig. 5.10(c) shows the number of cells the boundary layer is resolved with. The yellow line represents C100-120 where less than 10 cells resolve δ for the first stage of growth from $R = R_{\text{crit}}$ to $R = 10R_{\text{crit}}$. Therefore, C100-120 is used to assess the sensitivity of the reference solution to the mesh spacing. Figure 5.11(a) compares the results of the default mesh to a mesh with increased resolution. The bubble radius in Subfig. 5.11(a) compares very well for both meshes with differences only at the early time intervals. Subfigure 5.11(b) depicts the corresponding number of cells in the boundary layer. With the finer mesh δ is well resolved by more than 30 cells during the first period. The difference in the radius during the early stages results from the different initial delay times. A mapping of the physical time t to $t^* = t - t(R = 1.01 \cdot R_{\text{crit}})$ allows to compare solely the growth process without effects of the initial delay. Figure 5.12 shows that the corresponding results for the two meshes fit very well. The low resolution of the boundary layer in the early stages does not affect the growth process but only the initial delay. The delay time in the computations strongly depends on the numerics. In the present case a pressure increase in the bubble by 1% for the first time step triggers the growth from the mechanical equilibrium. Physically, such fluctuations may occur as a consequence of turbulent fluid motion or thermal motion of the molecules. A direct relation of the numerical disturbances to the physical fluctuations is difficult. However, since the actual growth process seems unaffected by the initial delay this issue is not further investigated here. The influence of the delay time on the calibration of the vaporisation models for the DNS is discussed in Sec. 6.1.

In Sec. 5.2.1 the different stages of bubble growth and the relevant physical mechanisms determining the growth rates were discussed. If time and bubble size are normalized by [81]

$$t^+ = \frac{A^2 t}{B^2}, \quad R^+ = \frac{AR}{B^2}, \quad (5.8)$$

with $A = \sqrt{\frac{2}{3} \frac{h_{\text{fg}} \rho_{\text{vap}} (T_{\infty} - T_{\text{sat}})}{\rho_{\text{liq}} T_{\text{sat}}}}$ and $B = Ja \sqrt{\frac{12}{\pi} a_{\text{liq}}}$, then the asymptotes of the inertia and heat conduction driven stages can be approximated by linear and square root dependencies of R^+ on t^+ , respectively [81]. An analytical equation for the

dimensionless radius reads

$$R^+ = \frac{2}{3} [(t^+ + 1)^{3/2} - (t^+)^{3/2} - 1]. \quad (5.9)$$

The normalisation defined by Eqs. (5.8) and (5.9) was originally introduced by Mikic et al. [69] and covers the inertia and heat diffusion driven stages. It uses several assumptions and empirical correlations which may introduce appreciable uncertainties. However, Eq. (5.9) compares surprisingly well with multiple experimental and numerical studies [6, 81]. In the context of the current study, these correlations provide first estimates of the relevant bubble growth stages and the asymptotic limits for flash boiling of cryogenic oxygen. Other analytical solutions coupling the different stages of bubble growth are presented, among others, by Theofanous and Patel [109], Prosperetti and Plesset [82] as well as Avdeev et al. [6], but are not further discussed here.

The $t^+ - R^+$ relationship according to Mikic et al. [69] is demonstrated in Fig. 5.13. Here, the reference solutions for single vapour bubble growth have been normalized as introduced by Eqs. (5.8) and the dashed and dash-dotted lines indicate the asymptotic limits of Eq. (5.9). It is apparent that inertia driven growth holds for times smaller than $t^+ = 10^{-2}$ only, while diffusion controlled growth requires growth for time scales longer than $t^+ = 50$. The intermediate range is defined from $10^{-2} < t^+ < 50$. Figure 5.13 shows the cases C5-90, C5-120, C100-90 and C100-120, which cover a wide spectrum of Ja including the highest and the lowest degree of superheat within the present parameter range. The maximum physical simulation

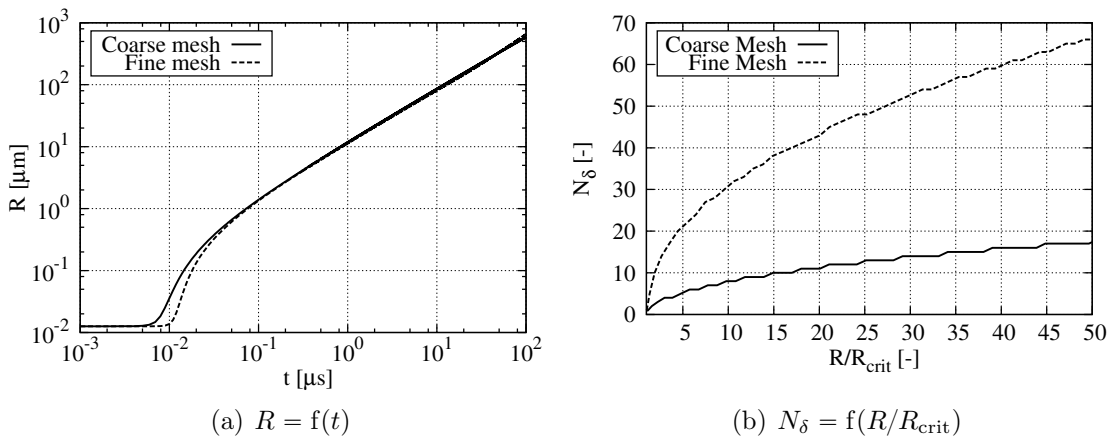


Figure 5.11: Bubble radius and boundary resolution for case C100-120 using different mesh resolutions.

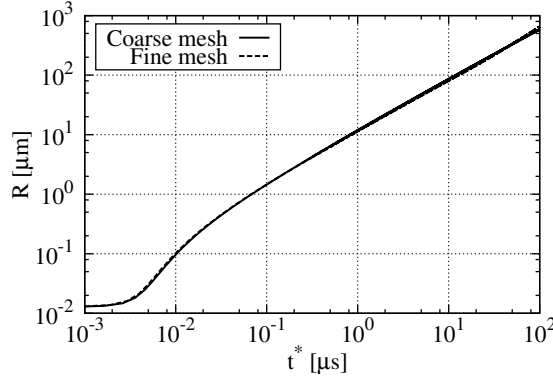


Figure 5.12: Bubble radius for different mesh resolutions without initial delay.

time in this reference study is $t = 100 \mu\text{s}$ because flash vaporisation is not limited to single bubble growth, nucleation rates are high and bubbles will rapidly interact and merge. Only case C5-120 becomes heat diffusion controlled within this time interval and all other cases are either inertia controlled or lie within the intermediate range. Increasing R_p or Ja shifts the dimensionless solution towards the inertia controlled range for the same final time while an increase in T_0 has the opposite effect. Lee and Merte [62] observed the same trend comparing different experimental investigations. This analysis shows that the majority of our test cases is inertia controlled. However, the vaporisation models cannot be calibrated towards a mass flux which is solely derived from the solution of Eq. (5.5) without coupling of the temperature equation as explained subsequently with the aid of Fig. 5.14.

Figure 5.14 demonstrates the effect of heat diffusion and evaporative cooling on the reference solution. The black lines depict the bubble radius over time for case C100-90 with (solid lines) and without (dashed lines) diffusive terms, where the initial bubble growth is nearly identical. The blue lines show the corresponding vaporisation mass flux and considerable differences between the coupled and the uncoupled solutions occur even at early stages, where the bubble radii still feature very similar values. The mass flux is determined as $\dot{m}'' = \rho_{\text{vap}} \dot{R}$. Without heat diffusion the mass flux increases and remains at a high level. At the same time, the pressure in the bubble and the vapour density remain constant. If evaporative cooling (and thereby heat diffusion) is included, the mass flux decreases after an early peak, the pressure in the bubble decreases and the vapour density decreases as well. In the inertia controlled range, the growth rate of the bubble (\dot{R}) is not affected by the different mass fluxes because the vapour density changes for the different

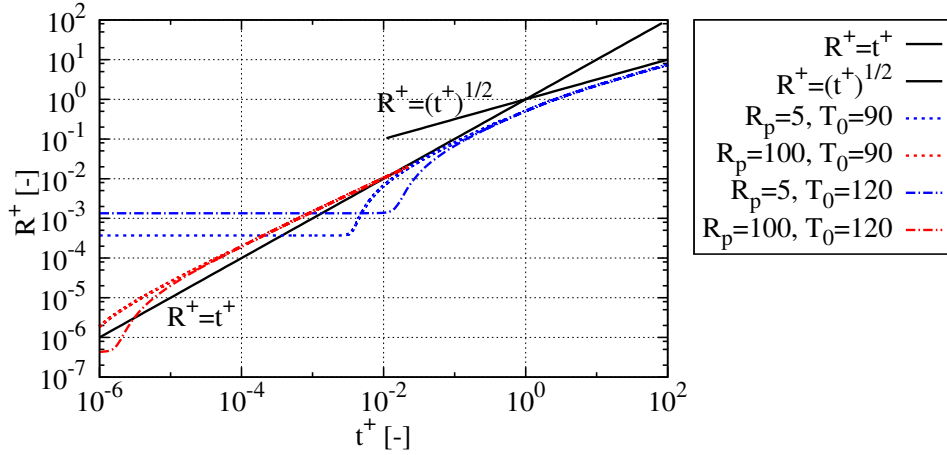


Figure 5.13: Dimensionless bubble radius over time for different combinations of T_0 and R_p , respectively. The dashed line defines the analytical solution in the inertia controlled range. The dash-dotted line indicates the analytical solution in the heat diffusion controlled range.

approximations and compensates the variation in \dot{m}'' . Therefore, the volumetric flow rate $\dot{V} = A \cdot \dot{m}'' / \rho_{\text{vap}}$ (with A being the bubble surface) is similar for the two approaches within the inertia controlled regime. It is concluded that evaporative cooling affects the bubble pressure and the mass flux throughout the entire growth process, but the growth rate is markedly affected at later stages only. Regarding the simulation of bubble growth with the DG solver it seems attractive to omit the early stages and use the converged mass flux from the RPE reference solution as input (i.e. replace the models introduced in Sec. 3.3 by the converged mass flux of the reference solution). This, however, turned out to be inaccurate. In the DG solver, the bubble pressure will also drop despite the omission of heat conduction and subsequent temperature decrease at the interface since the bubble is fully resolved and surface effects become small as the radius increases. The mass flux of the DG solver should therefore not be calibrated towards the constant mass flux derived from the RPE solution without heat diffusion, as this will strongly overpredict the growth rate. Therefore, it is concluded that evaporative cooling and heat diffusion are required to predict all physical quantities accurately, even for the inertia driven stage. The HLLP Riemann solver presented in Sec. 4.3 does not account for the heat diffusion at the interface. In the bulk phases non-viscous Riemann solvers can be extended to account for diffusive fluxes using the approach of Bassi and Rebay [9, 10]. They approximate the diffusive flux as the arithmetic mean of two neighboring cells. This is a valid approach in the continuous bulk phases but it will

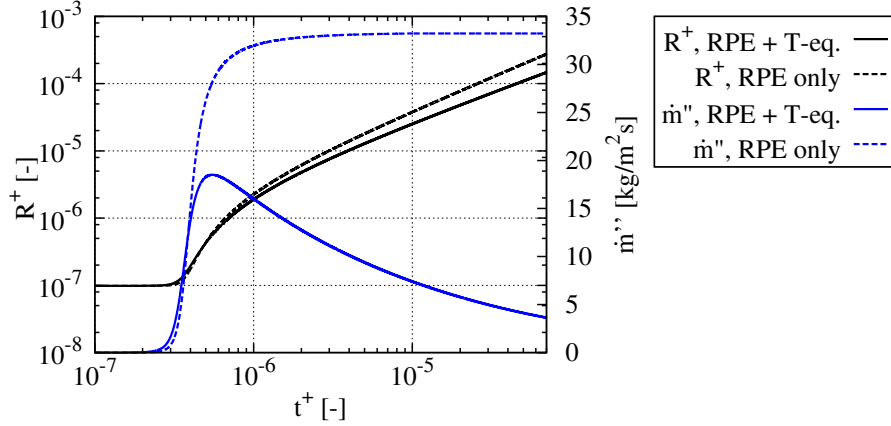


Figure 5.14: Reference solution for case C100-90 with (solid lines) and without (dashed-lines) coupling of the temperature equation 5.6. Black lines show the dimensionless radius R^+ and blue lines show the instantaneous mass flux.

lead to non-physical fluxes if applied across the interface. To avoid any inconsistency with the HLLP Riemann solver the DNS does not resolve heat diffusion across the interface and the vaporisation models are calibrated such that the growth rates of the bubbles are matched for particular time intervals. Section 6.1.1 assesses the validity of this approach.

Figure 5.14 also indicates that the relevant length scales of bubble growth easily cover three orders of magnitude. For different physical conditions these ranges may even be larger for the same time interval. This is shown in Fig. 5.9(a) which depicts the physical bubble radii at $R_p = 5$ for the different temperatures. The bubble grows by four orders of magnitude for $T_0 = 120$ K which is impossible to resolve in full 3D computations. As the volumetric jet expansion and jet break-up are key quantities of interest, it is fair to stipulate that the early stages of growth are not relevant. Figure 5.15 depicts the total vaporised mass (solid lines) and the mass flux (dashed lines) as functions of the bubble radius R . The mass flux peaks at low R but the total vaporised mass accumulates during the final stages, due to the R^2 -dependence of the surface area of the bubble. Thus,

- it is valid to assume that early bubble growth can be neglected and that
- the initial bubble radius for the DG simulation can be increased to $R_0 = 0.1R_{\text{end}}$. The computations would then cover 99.9% of the volume expansion of a single bubble growing from R_{crit} to R_{end} .

In a real jet the final bubble radius will depend on the generally unknown nucleation

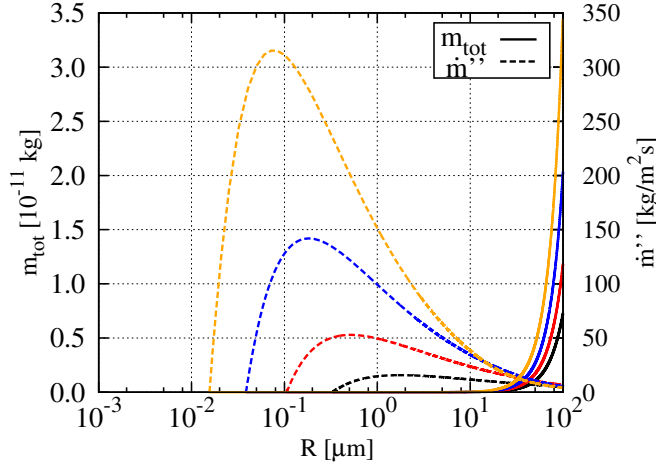


Figure 5.15: Results obtained from the RPE coupled to the temperature equation for different temperatures (colours) at $R_p = 5$

rates. Within the present work different possible growth stages are considered and represented by the normalized radius

$$R^* = \frac{R}{R_{\text{crit}}} \quad (5.10)$$

and the initial radii

$$R_0^* = \frac{R_0}{R_{\text{crit}}} = \{1, 5, 10, 25, 50\} \quad (5.11)$$

as a third independent parameter in addition to T_∞ and R_p . The reference solution from Sec. 5.2 defines the final simulation time for each combination of R_0^* , T_∞ and R_p with $t_{\text{end}} = f(R_{\text{end}} = 10R_0)$. Note that the initial radius in the reference solution (RPE) is always equal to the critical radius. In summary, the test matrix is defined by three independent variables. Two of these parameters, T_0 and R_p , define the physical conditions and the third parameter, R_0^* , defines the range of the length and time scales that are covered during the simulation time.

Figure 5.16 depicts different terms of the RPE for case C5-120. The black, red and yellow lines represent the pressure in the bubble $p_{\text{sat}}(T = T_{\text{int}})$, the surface tension and the viscous term, respectively. The blue line shows the pressure in the liquid at the bubble defined by the boundary condition

$$p_{\text{liq}}(r = R) = p_{\text{vap}} - \frac{2\sigma}{R} - \frac{4\mu\dot{R}}{R}, \quad (5.12)$$

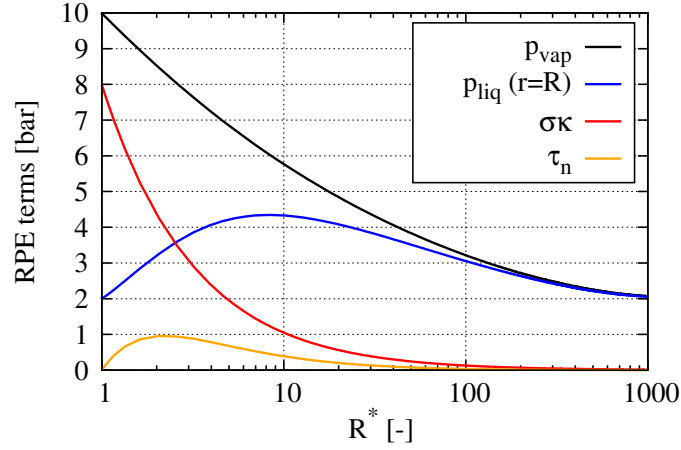


Figure 5.16: The black, red and yellow lines show the bubble pressure, the surface tension and the viscous terms in the Rayleigh-Plesset equation for C5-120. The blue line represents the liquid pressure at the bubble wall defined by Eq. (5.12)

see also Eq. (C.15) in Appendix C. Figure 5.16 reveals two features of single bubble growth that are important for the subsequent investigations. Firstly, the liquid pressure increases at the bubble wall. Section 5.1 showed pressure waves rapidly propagating through the liquid and an amplification if they are reflected, e.g. at a symmetry plane. In cases with multiple bubbles pressure waves originating from different bubble walls will be reflected and amplified when they interact. This will lead to a local pressure increase. The influence of this pressure rise on the bubble growth rates is discussed in Ch. 7. Secondly, the viscosity affects the growth process only at early stages where it is of the same order as the liquid pressure $p_{liq}(r = R)$. Therefore, viscous tension can be neglected if isolated bubbles are considered because it mostly influences the delay time of the start of the bubble growth process, only.

5.3 Numerical tests

Section 5.2 introduced a reference solution for single vapour bubble growth. This test case is used to validate the DNS solver for the computation of multiple bubble growth. The computation of single bubble growth with the DNS solver requires a calibration of the vaporisation models introduced in Sec. 3.3 for each combination of the independent parameters T_0 , R_p and R_0^* . A detailed study for the calibration for the entire parameter range is presented in Ch. 6. The present section uses C5-120 with $R_0^* = 50$ to analyse the sensitivity of the solution to numerical parameters and

to compare the results for the EOS approximations given in Sec. 3.4.

5.3.1 Base case setup

The spherically symmetric reference solution allows for the use of identical symmetry conditions in the DG solver. The tangential stresses are zero for spherical symmetry and Fig. 5.16 showed that normal stresses are negligible for single bubble growth under the present operating conditions. In this case, the Cartesian three-dimensional equation system (3.2) can be reverted to a 1D configuration with spherical symmetry by adding the source term [111]

$$\mathbf{S} = \frac{2}{r} \begin{pmatrix} \rho u \\ \rho u^2 \\ u(E + p) \end{pmatrix} \quad (5.13)$$

to the right hand side. Figure 5.17 depicts the geometrical setup where the bubble is on the left side of the domain. The left boundary at $r = 0$ indicates the bubble centre and is treated as a symmetry plane. The superheated liquid fills the right side with an outflow boundary condition at $r = L$. The default domain size satisfies the condition

$$L = \frac{t_{\text{end}} c_{\text{liq}}}{2} \quad (5.14)$$

ensuring that a pressure wave can travel only one time forth and back through the domain. The parameters $C = f \cdot N_{DG}$, $r^* = \frac{1-Cr_{\text{ref}}}{1-C}$ and $r_{\text{node}} = L \cdot r^*$ determine the radial position of a polynomial node r_{node} . Here, f , N_{DG} and r_{ref} are an adjustable stretching coefficient, the number of discontinuous Galerkin elements and the node coordinate in an equidistant reference domain ranging from 0 to 1, respectively. The degree of the polynomial is kept constant for all simulations with $N = 3$. The default stretching factor is $f = 1.03$ and the number of DG elements N_{DG} is set such that a bubble is initially resolved with at least ten discretisation points. Table 5.4 summarises the default parameters. The numerical tests in the present section are accomplished using the Hertz-Knudsen relation. The model coefficients are calibrated against the reference solution from Sec. 5.2 and also provided in Tab. 5.4.

The preceding section discussed the condition for the initial radius according to Eq. (5.11). The increase in initial radius reduces the computational cost compared

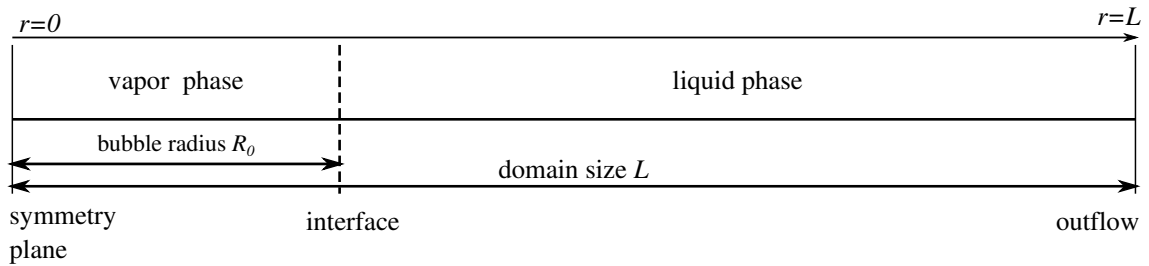


Figure 5.17: Geometrical setup for single bubble growth.

Table 5.4: Default numerical and geometrical parameters as well as physical models for single bubble test case C5-120 with $R_0^* = 50$.

parameter	value	comment
Vaporisation model	HKR	Sec. 3.3
λ_{vap}	0.038	calibrated (see Ch. 6)
λ_{cond}	0.0376	$\lambda_{\text{vap}} = 0.99\lambda_{\text{cond}}$
EOS	CoolProp	
DG cells	120	
N_{poly}	3	
L	0.33 mm	Eq. (5.14)
f	1.03	mesh stretching coefficient
FV order	2	
IF order	1	
CFL	0.9	

to $R_0 = R_{\text{crit}}$ for two reasons: Firstly, for a fixed number of cells across the bubble radius the total number of computational cells reduces. Secondly, the required time step increases with the cell width and therefore with R_0 if, again, the number of cells across the bubble radius is constant. For a given final simulation time, the total number of time steps reduces with increasing time step size. The total computational time is proportional to the number of time steps and the number of cells. The computational time relative to the computational time with $R_0 = R_{\text{crit}}$ reads

$$\frac{t_{\text{CPU}}}{t_{\text{CPU},R_{\text{crit}}}} = \frac{\Delta t_{R_{\text{crit}}}}{\Delta t} \frac{N_{DG}}{N_{DG,R_{\text{crit}}}}. \quad (5.15)$$

Table 5.5 lists the results for $R_0^* = 5 \dots 50$. They do not strongly depend on T_0 nor R_p . The meshes for the present analysis were constructed such that the number of cells across the bubble radius and the cell width approaching the right end of the domain (cf. Fig. 5.17) are constant for $R_0 = R_{\text{crit}}$ and $R_0 = R_0^* \cdot R_{\text{crit}}$, respectively. The

Table 5.5: Relative computational time for different R_0^* in percent.

	$R_0^* = 5$	$R_0^* = 10$	$R_0^* = 25$	$R_0^* = 50$
$t_{\text{CPU}}/t_{\text{CPU,Rcrit}}$	15%	7%	2%	1%

computational time reduces by at least 85% compared to the cases with $R_0 = R_{\text{crit}}$. At $R_0^* = 50$ the computational time reduces to 1% emphasising the benefit of using Eq. (5.11).

5.3.2 Mesh resolution and time step restriction

A grid dependency study is conducted to ensure independence of results on the major numerical parameters. These include the domain size, L , the bubble resolution, i.e. the grid size, and the time step that is here expressed with the aid of the CFL number. The influence of these parameters is studied for C5-120 with $R_0^* = 50$. First, the domain size is varied to assess the influence of wave reflections from the boundary: L is given by Eq. (5.14). It is then increased and decreased by a factor of 2 for the current study. The specific parameters are given in Tab. 5.6. Figure 5.18(a) depicts the bubble radius over time which is not sensitive to the domain size. Diagram 5.18(b) shows the pressure field at the final time and an increase in p on the liquid side is observed for $L/2$ compared to L and $2L$. The differences arise due to weak shock wave reflections at the outflow boundary condition. The deviation in the pressure field does not affect the bubble growth but using the domain size L in Eq. (5.14) guarantees mesh independence throughout the investigation and L is used for the remainder of this work. Figure 5.19 depicts the same quantities for a varying resolution of the initial bubble with $N_{\text{bub}} = 5$, $N_{\text{bub}} = 10$ and $N_{\text{bub}} = 20$. Table 5.7 lists the corresponding mesh parameters. The three cases are in very good agreement indicating mesh independent results for the given criteria. Figure 5.19 also illustrates results when using a reduced time step (here, the CFL number is set to 0.45). Again, no significant changes in the growth rates and in the resulting pressure field are observed. The bubble radii deviate by a maximum of 2.2%, 1.4% and 0.9% comparing the cases with a variable cell width, time step size and domain length, respectively.

Table 5.6: Parameters for domain size sensitivity study. The default length L is given by Eq. (5.14).

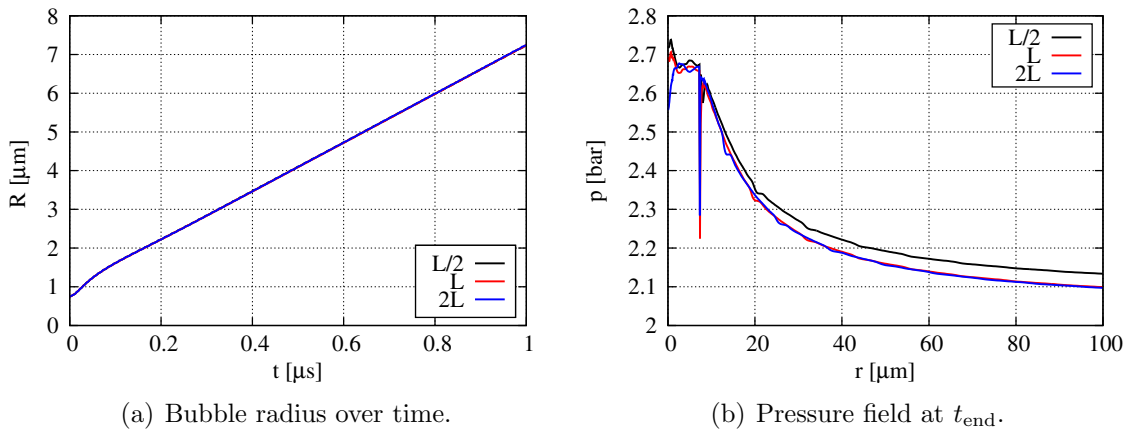
	domain size [mm]	f [-] f [-]	DG cells DG cells
$L/2$	0.165	1.029	100
L	0.33	1.03	120
$2L$	0.66	1.031	140

Table 5.7: Parameters for cell size sensitivity study.

N_{bub}	f [-]	DG cells
5	1.062	60
10	1.03	120
20	1.015	240

5.3.3 Discretisation order and HLLP approximation at the interface

This section analyses the sensitivity of the results to the numerical approximation at the interface and in bulk phase FV sub-cells. The default setup introduced in Sec. 5.3.1 uses a first-order approximation at the interface (IF-order) and a second order approximation in the bulk phase FV sub-cells (FV-order). The HLLP Riemann solver is treated explicitly as discussed in Sec. 4.3. The sensitivity of the results to these numerical parameters is investigated here using the three combinations


 Figure 5.18: Results of C5-120 with different domain sizes ($L/2$, L , $2L$) for $N_{\text{bub}} = 10$.

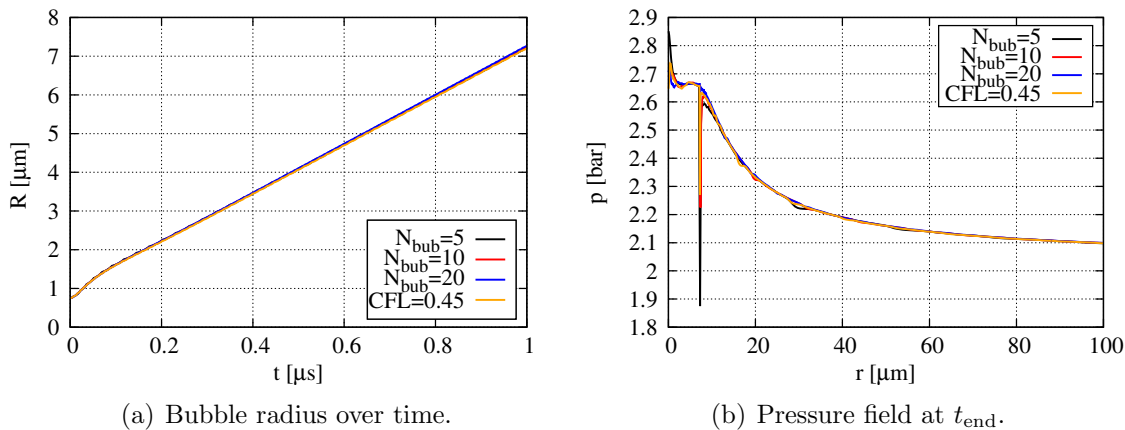


Figure 5.19: Results of C5-120 with different bubble resolutions N_{bub} and with $\text{CFL} = 0.45$ using the domain size L .

- FV-order: 1st; IF-order: 1st; HLLP: explicit,
- FV-order: 2nd; IF-order: 2nd; HLLP: explicit,
- FV-order: 1st; IF-order: 2nd; HLLP: implicit.

Figure 5.20 depicts the corresponding results for the radius and the final pressure field. Significant differences in the growth rate are only obtained if the gradient approximation at the interface is changed to the more accurate second-order scheme. Using a first-order approximation also in the bulk phase results in a significant change in the pressure field. If both, the interface and the bulk phases are treated with a second order scheme the pressure fluctuation at the interface on the liquid side is avoided. However, a second-order treatment in a three-dimensional case requires the solution of additional differential equations as suggested by Aslam [5], see also Sec. 4.2. Thereby, the computational effort may rise significantly. Since the general physical aspects are also covered with the first-order approximation this will be used in the remainder of the present work. This considerably reduces the computational time for the three-dimensional simulations in Ch. 7. Note that the vaporisation models are scaled such that the reference solution is matched. In principal, a good match may be obtained for any combination of the numerical parameters. A consistent comparison between the single bubble DNS in Ch. 6 and the multiple bubble DNS in Ch. 7 will be ensured using the same numerical setup, respectively.

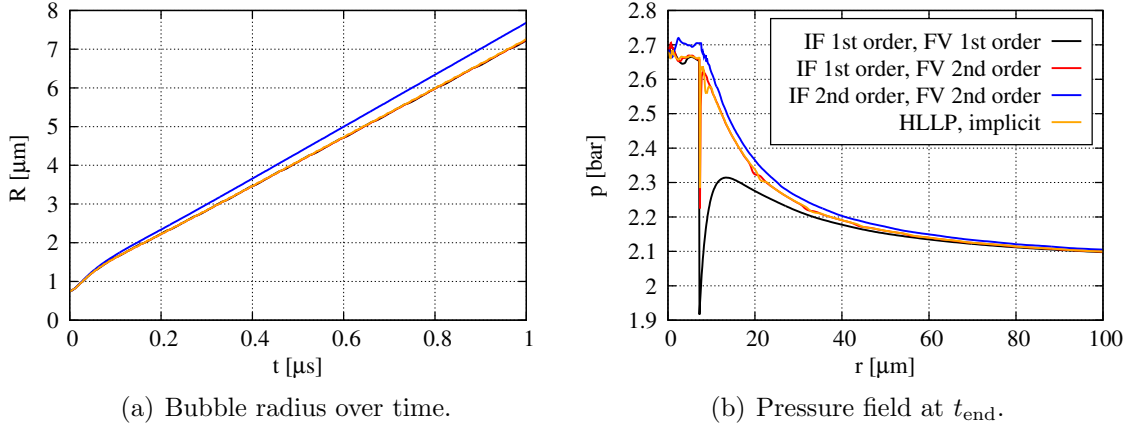


Figure 5.20: Results of C5-120 with different bubble resolutions N_{bub} for $L = L_2$.

5.3.4 Initial condition for the vapour in the bubble

The previous test cases initialised the vapour in the bubble according to the initial conditions defined by T_0 and R_p using the physical conditions presented in Sec. 5.2.3. The initial bubble radius is increased from $R_0^* = R_0/R_{\text{crit}} = 1$ to $R_0^* = 50$. The pressure in the bubble is equal to the saturation pressure at the ambient temperature $p_{\text{sat}}(T_0)$. This initialisation is referred to as the default initialisation within the present section. Following the results in Sec. 5.2.4 the bubble pressure reduces when the bubble grows. Therefore, an initialisation of the vapour with a reduced pressure obtained from the reference solution at $R^* = 50$ seems a reasonable alternative. Figures 5.21(a) and 5.21(b) depict the corresponding pressure fields after 10% of the physical simulation time and at the end of the computation. The default setup with the increased vapour pressure rapidly converges towards the solution using a decreased initial pressure. The pressure fields deviate for very early time intervals only suggesting no significant effect of the pressure initial condition on the DNS solution.

The simplified initialisation associated with the increase in the initial bubble radius also affects the initial velocity field. While the initial interface velocity is zero in the DNS the reference solution yields a non-zero velocity at $R^* = 50$. Figure 5.22 depicts the interface velocity for the reference solution (blue line) as well as the DNS with the default initialisation (black line) and with a decreased initial bubble pressure (red line). Again, the default solution converges to the solution with the reduced pressure after a short time. Moreover, the early peak in the interface velocity observed for the reference solution is also obtained with the DNS using the default

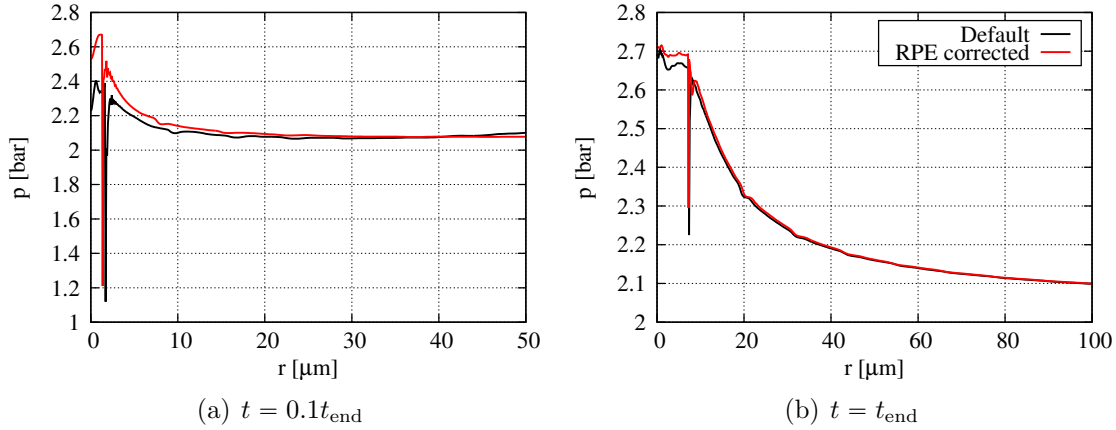


Figure 5.21: Pressure fields of C5-120 with $R_0^* = 50$ with different initial conditions for the pressure field.

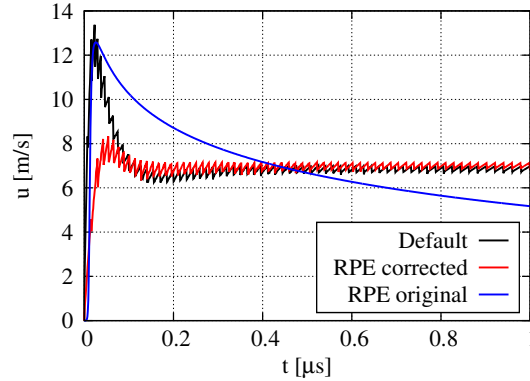


Figure 5.22: Interface velocity for C5-120 and $R_0^* = 50$ with different initial conditions for the pressure.

initialisation. Since the pressure difference is initially higher than the surface tension a strong pressure wave propagates through the liquid. This yields a strong increase in the liquid and consequently of the interface velocity. The simplified start conditions in the pressure field compensate for simplified start conditions in the velocity field. Therefore, the default initial conditions with $p_{\text{vap}} = p_{\text{sat}}(T_0)$ are used for the bubble in the remainder of this work.

5.3.5 Equation of state

In the following section the results using the CoolProp EOS library and the NASG-EOS are compared. The coefficients for the NASG-EOS for liquid oxygen are obtained using the algorithm of Le Métayer and Saurel [68]. The CoolProp library

provides the reference data for the computation of the coefficients and for a validation of the resulting correlations. Table 5.8 lists the coefficients for the vapour and the liquid phases, respectively. Figures 5.23 and 5.24 depict the resulting correlations for the vapour and the liquid phase, respectively. The lines represent the reference data from the CoolProp library and the symbols show the NASG results. The subfigures show the specific volume, the specific internal energy, the speed of sound and the specific entropy as functions of the temperature for three different pressures. The NASG data match the CoolProp data well on the vapour side. Only the specific internal energy slightly deviates for high temperatures, and in particular for temperatures above 100 K. Note that the subcooled vapour states are omitted in the data generation with CoolProp because they are not of interest for the present computations. In the liquid phase (cf. Fig 5.24) the specific internal energy and the specific entropy compare well to the reference data for the entire temperature range. The specific volume matches well the CoolProp data at temperatures below 100 K but increasingly deviates at higher temperatures. The speed of sound is predicted correctly only at $T = 90$ K. Below 90 K, c is underpredicted and above 90 K it is overpredicted.

Since the best EOS fit with the NASG approximation is obtained at $T = 90$ K the results of the single bubble DNS are compared for C5-90 and C5-120 with $R_0^* = 50$, respectively. Figure 5.25 depicts the bubble radius over time and the pressure field at the final simulation time. Both diagrams show that the NASG-EOS provides results in good agreement with those obtained using the CoolProp library. Figure 5.26 depicts the corresponding results for C5-120. Here, the differences between results using the different EOS approximations are considerably larger. The final bubble radius is overpredicted by approximately 70%. The coefficients of the NASG-EOS are computed for a predefined temperature range. Attempts to increase the accuracy for the temperatures above 100 K by adapting this predefined temperature range have not been successful. The NASG-EOS is an appealing alternative to more general EOS models because it is easy to implement and allows for a fast

Table 5.8: Coefficients for the NASG-EOS given in Eqs. (3.25)-(3.28).

	γ	P_∞	\tilde{q}	b	\tilde{q}'	C_v
vapour	1.4702	0.0	139968	0.0	1696.42	551.814
liquid	1.65513	1.96685×10^8	-151817	0.00057131	5160.61	1019.15

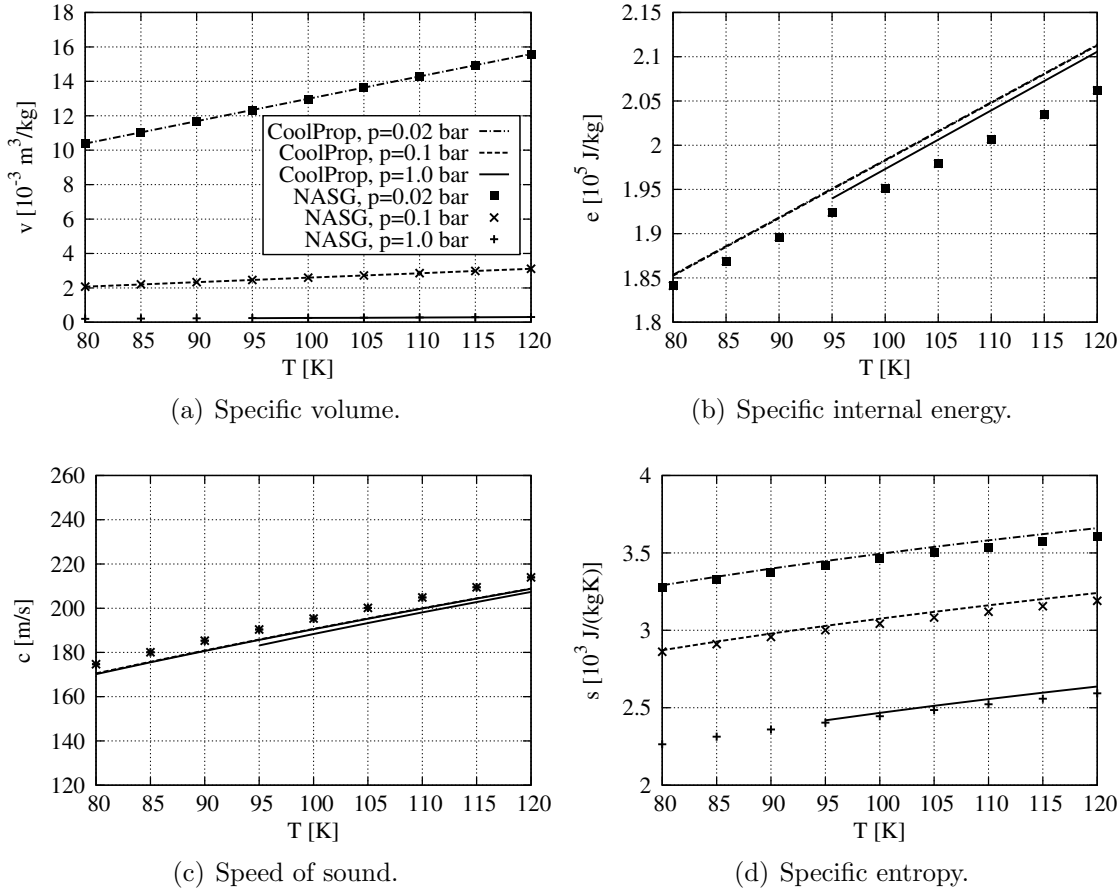


Figure 5.23: Comparison between CoolProp data and NASG approximation for the vapour phase at three different pressures.

computation of the fluid states. The present work relies, however, on the CoolProp library because the NASG-EOS does not cover the entire parameter range with sufficiently high accuracy.

5.3.6 3D simulation of single bubble growth

As a final validation, the capabilities of the 3D implementation of the DG solver are demonstrated. The results of the single bubble setup are compared between the 3D DG computation, the 1D DG computation and the reference solution (RPE). Figure 5.27 depicts the dimensionless bubble radius over time. The three-dimensional case agrees very well with the one-dimensional simulation and with the reference solution. Figure 5.28 shows a three-dimensional representation of the bubble growth. The four subfigures from the top left to the bottom right depict different simulation times ranging from $t = 0.0 \mu\text{s}$ to $t = 1.0 \mu\text{s}$. The left plane of each

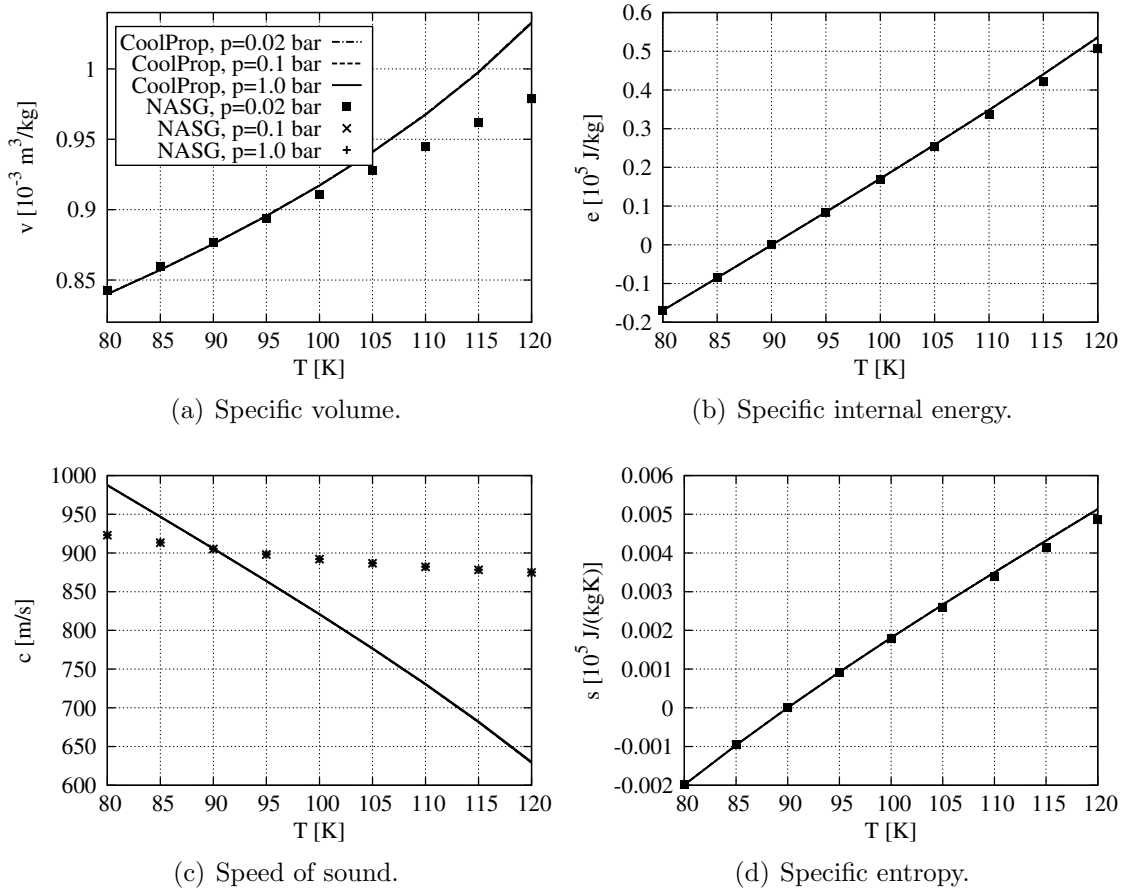


Figure 5.24: Comparison between CoolProp data and NASG approximation for the liquid phase at three different pressures.

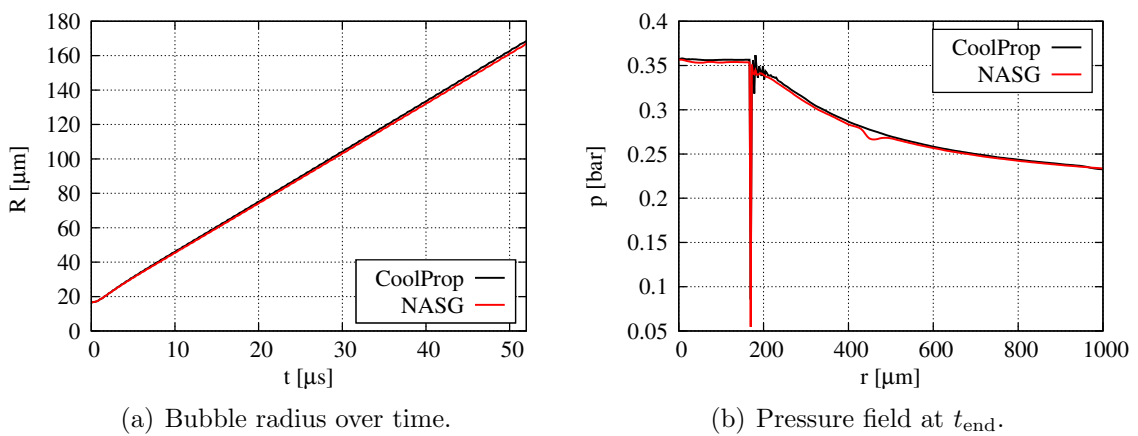


Figure 5.25: Results of C5-90 with different EOS approximations.

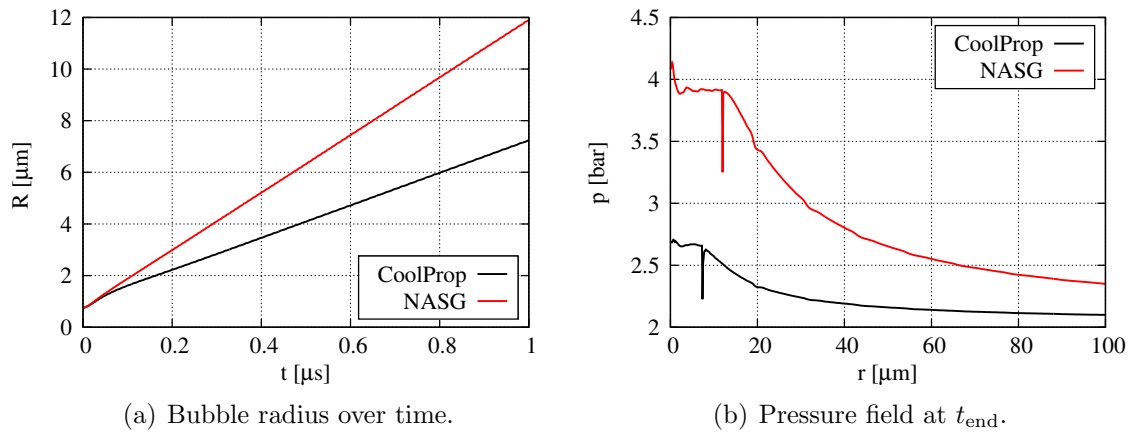


Figure 5.26: Results of C5-120 with different EOS approximations.

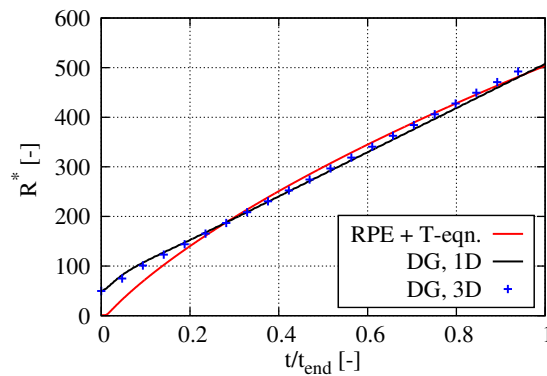


Figure 5.27: Normalized bubble radius R^* over time for C5-120 with $R_0^* = 50$. The DG simulation with the 1D solver (black line) and the 3D solver (blue crosses) match the reference solution (red line).

subfigure illustrates the pressure field. As observed in the 1D computation a pressure wave propagates away from the interface as the bubble grows. Note that the color bar scales with a maximum pressure of $p = 3$ bar which indicates that the global pressure level rapidly relaxes towards the ambient pressure. This effect was also discussed in Sec. 5.2, see Fig. 5.16. The right plane of the subfigures in Fig. 5.28 shows the characteristic velocity field for single vapour bubble growth: the velocity peaks at the interface in the liquid phase and decreases towards the outside due to the spherical symmetry of the problem. The density fields shown in the bottom planes demonstrate that the sharpness of the interface is guaranteed. The results show that the DG solver accurately captures essential physical effects of the growth of vapour bubbles. It is therefore a suitable tool for the computation of multi-bubble dynamics and their interactions under flashing conditions.

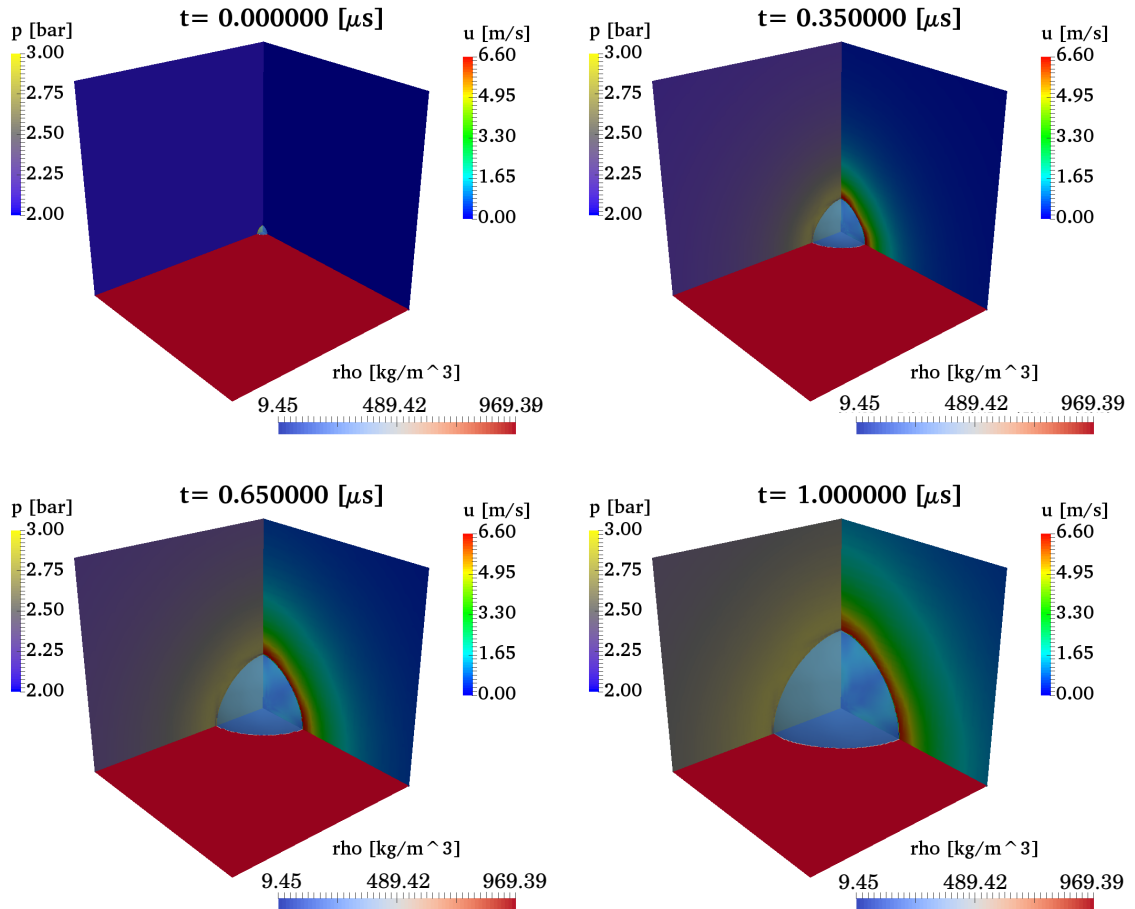
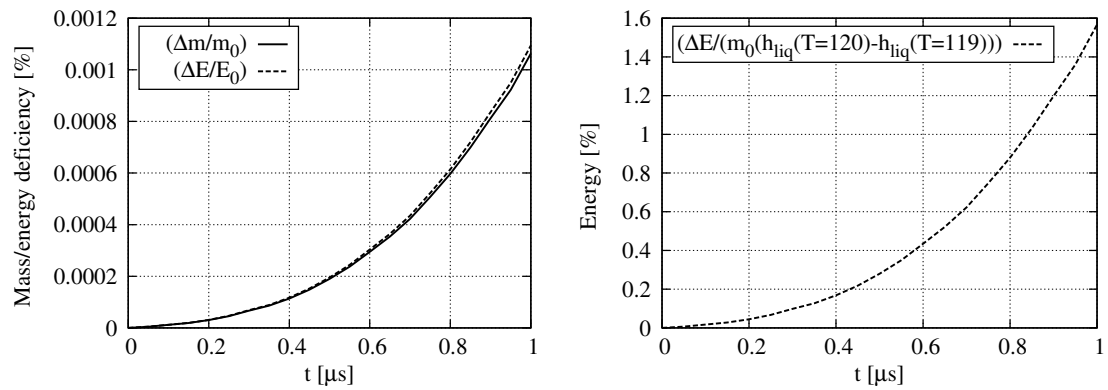


Figure 5.28: Three-dimensional representation of the bubble growth.

Finally, the mass and energy conservation is evaluated for the three-dimensional solver. Figure 5.29(a) illustrates the relative change of the total mass and the total energy throughout the simulation. Both increase by less than 1%. Section 5.1 demonstrated that the HLLP approximation does not resolve evaporative cooling and that the total energy therefore increases by the amount of the latent heat of vaporisation. Within the time intervals used for the computation of bubble growth in the present work, the relative amount of vaporising liquid is rather small and the unresolved evaporative cooling does not strongly affect the bulk liquid temperature. Figure 5.29(b) normalises the total energy increase by the energy released if the entire bulk liquid cools down by 1 K. The diagram reveals that the error introduced by the numerical approximation amounts to less than 2% of the energy needed to change the liquid temperature by 1K.



(a) Relative change of mass and energy.

(b) Change in energy relative to energy required to change the liquid temperature by 1 K.

Figure 5.29: Mass and energy conservation.

CHAPTER 6

DNS of single vapour bubble growth

The preceding chapter outlined the important properties of the DG solver and summarised the physics of vapour bubble growth using the example of LOX under flash boiling conditions. These investigations yield two important applications for the remainder of this work. Firstly, as discussed in Sec. 5.2.4, the bubble growth easily covers several orders of magnitude. Therefore, individual cases defined by R_0^* in Eq. (5.11) consider different stages of the growth process separately. Secondly, the evaporative cooling at the interface makes bubble growth a highly transient process. The HLLP Riemann solver does not account for evaporative cooling. Therefore, the vaporisation models are calibrated separately for each combination of R_p , T_0 and R_0^* in Sec. 6.1. A prediction of the model coefficients on the basis of the Rayleigh-Plesset reference data is suggested in Sec. 6.2.

6.1 Calibration of vaporisation models

The coefficients of the vaporisation models in Sec. 3.3 are calibrated such that the bubble radius at the final simulation time matches the reference solution. Starting from an initial guess the coefficients are scaled by the ratio of the obtained bubble radius in the DG computation to the target bubble radius. This is repeated until the model coefficients change by less than 1%. The entire process is automated to efficiently provide calibrated model coefficients for the 240 cases defined by R_p , T_0 , R_0^* and the vaporisation model.

6.1.1 Hertz-Knudsen relation

A direct calibration of the HKR is difficult because two model coefficients appear in Eq. (3.20). Setting $\lambda_{\text{cond}} = \lambda_{\text{vap}}$ reduces the accuracy of the model but simplifies the estimation of the remaining model coefficient. Lauer et al. [60] calibrated this single coefficient according to a reference solution for the simulation of cavitation bubbles. A similar strategy is used in the present work but $\lambda_{\text{cond}} = 0.99\lambda_{\text{vap}}$ is suggested to stabilise the simulations. At the initial time steps, when the solution deviates only slightly from mechanical and thermodynamic equilibrium, vaporisation is favoured and early bubble growth is stabilised. The present investigation does not consider bubble collapse nor bubble oscillations. At later time steps, the proposed reduction in the condensation rate does not change the results. The condition $\lambda_{\text{cond}} = 0.99\lambda_{\text{vap}}$ holds throughout the remainder of this work but the subsequent discussion refers only to λ_{vap} . In the following, the DG results are compared with the reference solution starting the discussion for case C5-120 with $R_0^* = 50$.

C5-120, $R_0^* = 50$

The black line in Fig. 6.1 depicts the normalized bubble radius R^* over time obtained from the DG solver while the red line shows the corresponding reference solution. The DG solution agrees well with the reference solution for the relevant time and length scales. The deviations are large only for $t/t_{\text{end}} < 0.2$ because the initial radius for the DG solution had been increased. The corresponding vaporisation coefficient $\lambda_{\text{vap}} = 0.038$ scales the mass flux towards $\dot{m}'' \approx 65 \text{ kg}/(\text{m}^2\text{s})$, see Fig. 6.2. The vaporisation mass flux converges to a constant value because the liquid remains superheated in the HLLP approximation. Initially, the vapour in the bubble is saturated and Eq. (3.20) gives a zero mass flux. There is no mechanical equilibrium, the bubble grows and the pressure in the bubble drops. With decreasing pressure the mass flux increases and the pressure drop is slowed down. After a short time the bubble pressure converges towards the ambient pressure and a steady state is reached for the bubble pressure and the mass flux. Figure 6.3 depicts the pressure field at different time steps. The bubble pressure approaches to the ambient level after $t/t_{\text{end}} \approx 0.08$. After that time, the bubble pressure and the mass flux remain unchanged. The qualitative behaviour of \dot{m}'' in the reference solution cannot be matched but the integrated mass flux depicted in Fig. 6.4(a) deviates by only 10%. The vaporisation coefficients are calibrated such that the final bubble radius

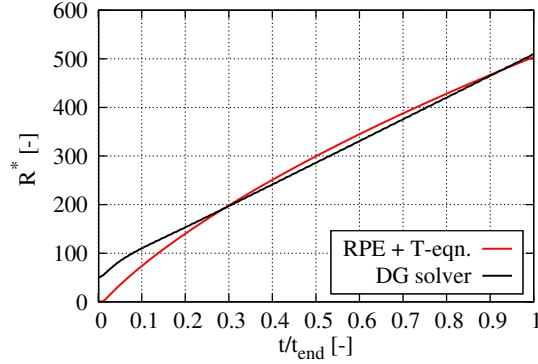


Figure 6.1: Normalized bubble radius R^* over time of case C5-120 with $R_0^* = 50$.

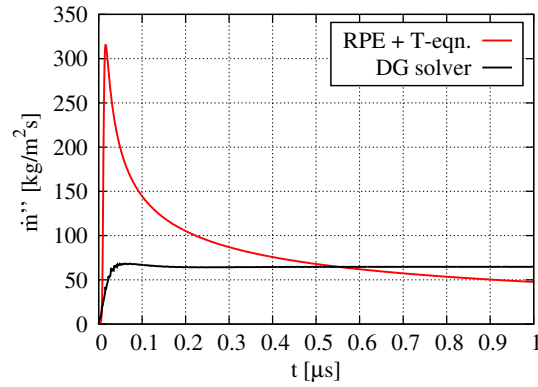


Figure 6.2: Vaporisation mass flux \dot{m}'' of case C5-120 with $R_0^* = 50$.

matches. The total vaporised mass deviates from the reference solution because the vapour densities are not exactly the same as in the reference solution and the same volume contains a different mass. The main focus of this work is the volume expansion of the bubbles. Figure 6.4(b) shows the total change in the bubble volume where the deviations are smaller. Thus, the HLLP Riemann solver coupled to the HKR is a suitable approach to predict the volumetric expansion of single vapour bubbles. Note that the results for total vaporised mass can be improved adopting the calibration to the target quantity m_{tot} . However, the calibration towards m_{tot} is found to be more difficult to obtain, particularly at low R_0^* . Given the good match in ΔV the calibration towards R is continued. The calibration of λ_{vap} is specific for the chosen time scale. The next step analyses the validity of the present approach for the same physical conditions, i.e. constant T_0 and R_p , at different time intervals implicitly defined by R_0^* (cf. Sec. 5.2.4).

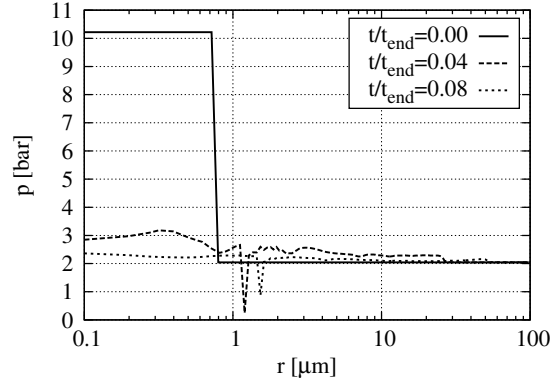


Figure 6.3: Pressure field of C5-120 and $R_0^* = 50$ at different time steps.

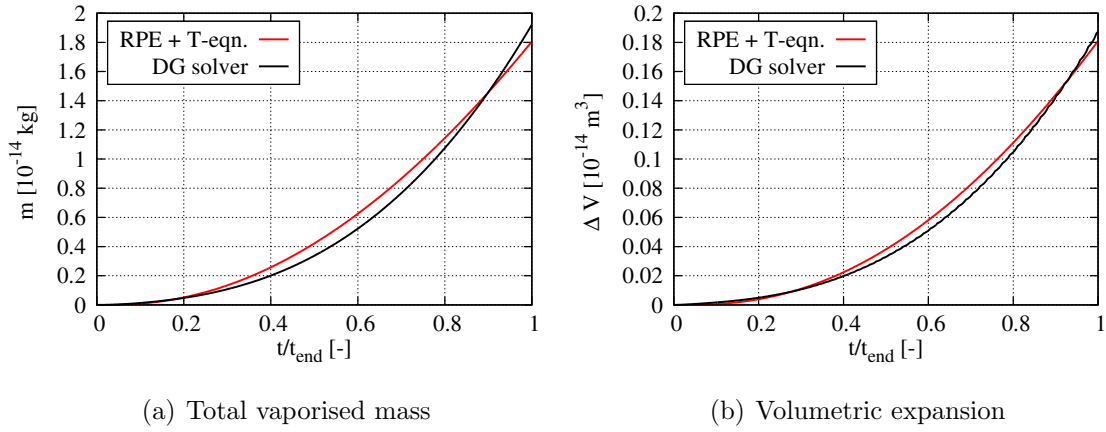


Figure 6.4: Integrated quantities of C5-120 and $R_0^* = 50$.

Variation of the initial radius R_0^*

In this section R_0^* is decreased towards the critical radius $R_0^* = 1$ keeping the time interval of each simulation fixed by $R_{\text{end}}^* = 10R_0^*$. Figure 6.5 depicts the bubble radii as a function of time where each individual calibration provides a good match with the reference solution for the final simulation time. The growth at the relevant length and time scales matches the reference solution well as seen for $R_0^* = 50$ in Fig. 6.1. Figure 6.6 depicts the total vaporised mass and the total volume change as a function of time for C5-120 with $R_0^* = 1$ and $R_0^* = 10$. The total vaporised mass deviates by more than 25% for the case with $R_0^* = 1$. The generated volume matches the reference solution well only close to t_{end} . In contrast, a very good agreement for both m_{tot} and ΔV is obtained starting from $R_0^* = 10$. While m_{tot} is predicted with different accuracy for the combinations of R_0^* , R_p and T_0 , very good matches in ΔV are observed across the parameter range with minor restrictions for $R_0^* = 1$.

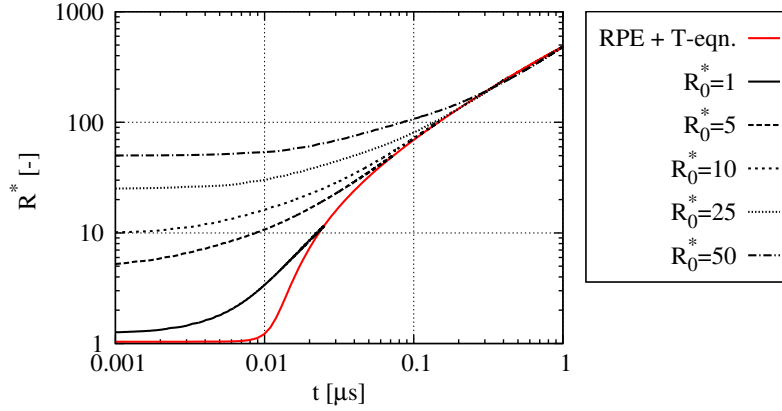


Figure 6.5: Normalized bubble radius R^* over time for different length scales.

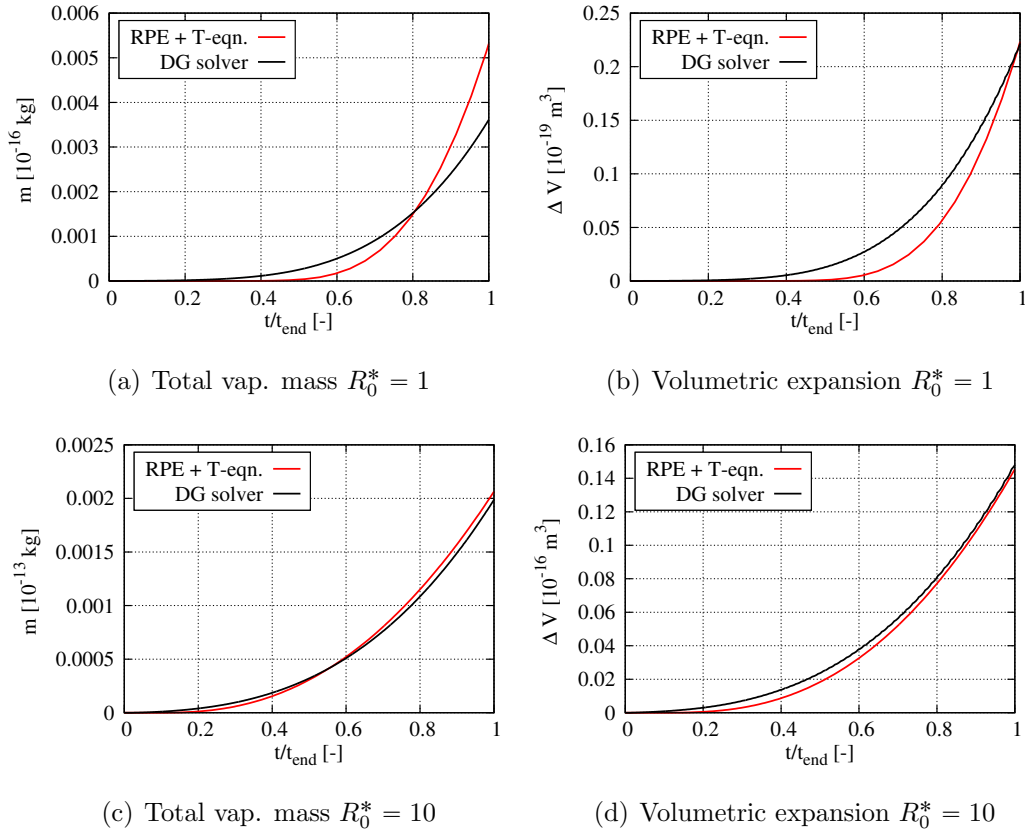


Figure 6.6: Total vaporised mass and volume change of C5-120 for different R_0^* .

Variation of the physical conditions

The following simulations are conducted using $R_0^* = 50$ and the superheat ratio R_p and the temperature T_0 are varied. Figure 6.7 shows the volumetric expansion for the cases C100-120 and C5-90, which agree well with the reference solution. Similar results are obtained for the various combinations of R_p , T_0 and R_0^* . Regarding the

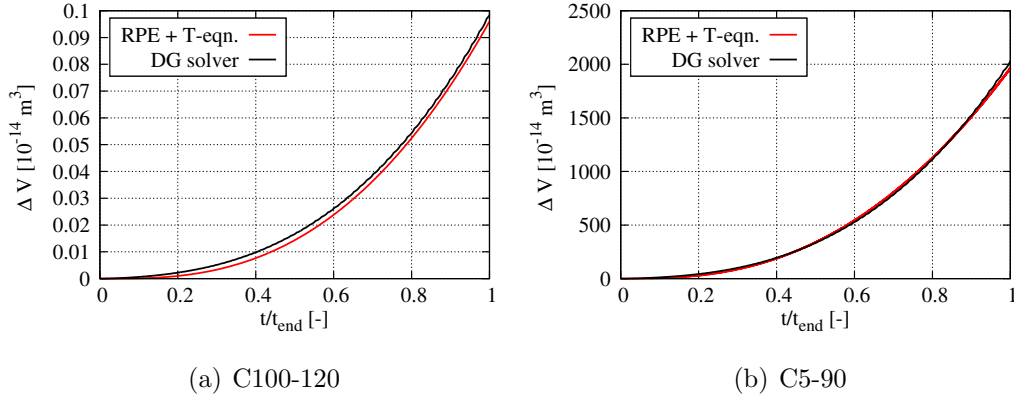


Figure 6.7: Volumetric expansion for $R_0^* = 50$ under different physical conditions.

simulation of single vapour bubble growth it is concluded that

- the simplifying assumptions discussed in Sec. 5.2.4 are valid in most of our cases,
- the bubble growth can be predicted within a wide parameter range using the HLLP Riemann solver combined to the HKR,
- the instantaneous mass flux cannot be predicted with the HKR within the HLLP Riemann solver.

6.1.2 Kinetic relation and sub-grid scale heat flux

This section compares the former results to the two alternative vaporisation models. Figure 6.8 depicts the corresponding vaporisation mass fluxes, the bubble radii and the volumetric expansion. The blue and yellow lines show results for the KR and the SHFM, respectively. The peak mass flux (Fig 6.8(a)) is slightly higher for the KR when compared with the HKR (black line), but - as the evaporative cooling in the HLLP approach is not resolved - it rapidly asymptotes towards a constant value. The asymptotes of the HKR and KR deviate by approximately 5%. Particularly at early times \dot{m}'' fluctuates but the volumetric expansion is nearly identical to the HKR (Fig. 6.8(c)). Similarly, trends observed for different initial radii R_0^* and for different physical conditions follow trends described for the HKR closure. The yellow lines in Fig. 6.8 represent the SHFM. Here, the mass flux agrees qualitatively better with the reference solution than the HKR and the KR solutions. The mass flux peaks during the initial stages and continuously decreases for larger time intervals. This results from the dependency of the vaporisation model on the continuously

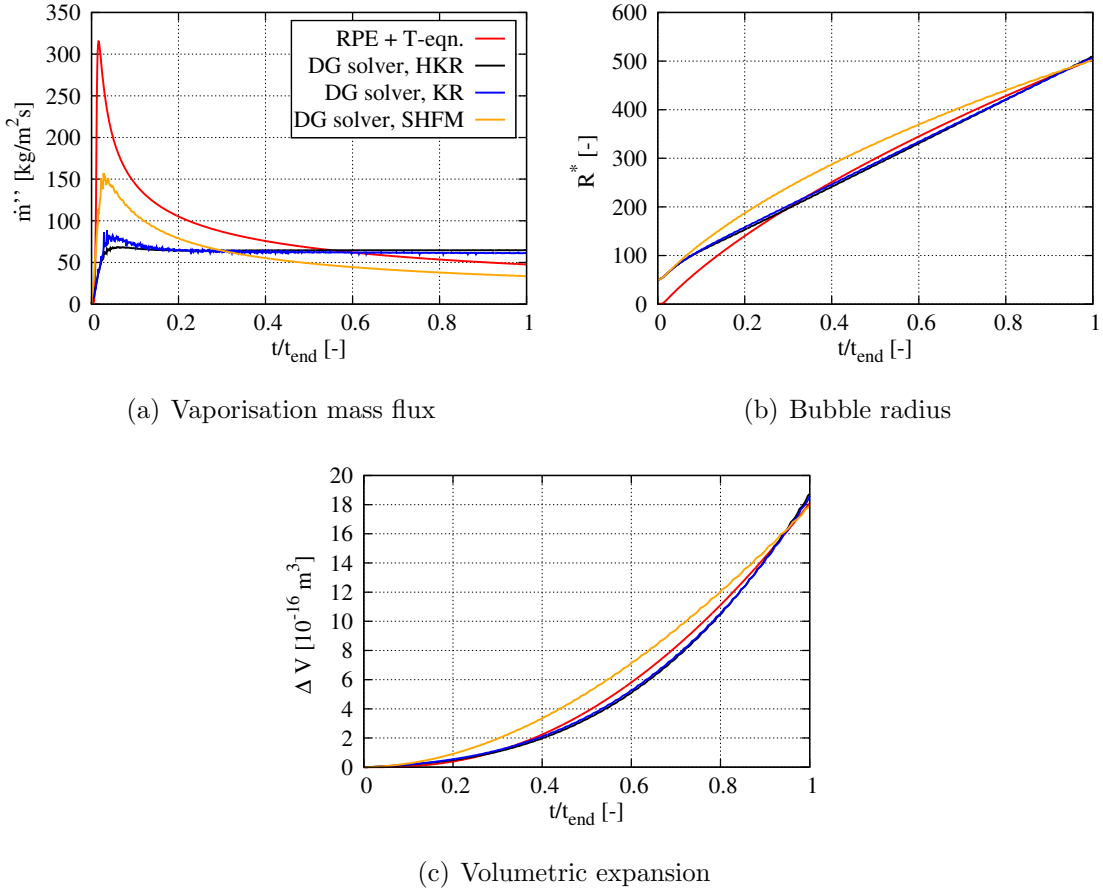


Figure 6.8: Comparison of HKR, KR and SHFM for case C5-120 and $R_0^* = 50$.

growing boundary layer thickness as it is defined by Eq. (3.24). However, the reference mass flux is underpredicted for the entire time interval. In contrast, the volumetric expansion is overpredicted because the increased radius $R_0^* = 50$ results in a larger bubble surface which allows for a faster volume expansion of the bubble (Fig. 6.8(c)). At the end of the simulation time all vaporisation models predict the volumetric expansion well. A better estimation of the boundary layer thickness δ can improve the prediction of the volumetric expansion of the SHFM for the early stages. This could be achieved by a dynamic determination of C_δ but further research would be required to find suitable models and is beyond the scope of the current work. The mesh resolution and time step size do not affect the characteristic progress of \dot{m}'' , R and ΔV . The findings discussed in Figs. 6.5-6.7 for the HKR were similarly made for the corresponding results of KR and SHFM closures.

6.2 Prediction of model coefficients

The previous sections demonstrated the validity of the present simulation strategy for a wide parameter range. The tables in Appendix D list the corresponding calibration coefficients. The main disadvantage of this approach is the need to iteratively calibrate the model coefficients for each combination of the initial parameters T_0 , R_p and R_0^* . A truly predictive simulation requires the modelling of the calibration coefficients and in this section, the relation of the model coefficients to the characteristic parameters of our study is discussed. The results follow similar trends for the different vaporisation models as subsequently exemplified for the HKR.

Figure 6.9 depicts the vaporisation coefficient λ_{vap} as function of R_0^* , R_p , T_0 , Ja , R^+ or t^+ (Figs. 6.9(a)-6.9(f), respectively). For the sake of clarity, the diagrams show the results from the bounds of the parameter ranges only, but trends for the intermediate values lie within these bounds. Subsequently, the dependencies shown in Fig. 6.9 are discussed for the individual subfigures:

- *Subfig. 6.9(a)*: For fixed physical conditions, λ_{vap} scales inversely proportional with R_0^* . The mass flux in the reference solution decreases monotonically with time/radius after its early peak (cf. Fig. 6.2). The combination of the DNS solver with the HKR closure yields - after a short transient stage at the beginning of a simulation - a constant mass flux. Depending on the growth stage λ_{vap} scales this constant mass flux such that the mean value of the reference solution is approached. At small R_0^* the coefficient λ_{vap} eventually increases because the early stage of bubble growth is highly transient with the fast increase in the reference mass flux at the beginning followed by a continuous decrease.
- *Subfig. 6.9(b)*: For small superheat ratios, no obvious relation between R_p and λ_{vap} is found. The solid and dash-dotted lines in Fig. 6.9(b) represent cases with $R_0^* = 5$ and $R_0^* = 50$, respectively. While λ_{vap} decreases with increasing R_p at low R_0^* , it increases with increasing R_p at high R_0^* . The reference growth rate increases with increasing R_p at later time intervals. Therefore, λ_{vap} also increases with increasing R_p at the high R_0^* range. At smaller R_0^* the reference growth rate also increases with increasing R_p but the differences are less pronounced. The inertia forces strongly affect the early growth stage and therefore λ_{vap} does not follow the trend obtained for higher R_0^* .

- *Subfig. 6.9(c)*: The calibrated coefficients λ_{vap} decrease with decreasing T_0 if R_0^* and R_p are fixed. With the temperature also the saturation pressure and - for a constant R_p - the ambient pressure change. Since these are key quantities in the HKR, see Eq. (3.20), the correlation between λ_{vap} and T_0 is difficult to assess. The driving pressure difference in Eq. (3.20) and therefore the resulting mass flux typically decrease for smaller temperatures. Here, we observe that the calibration of λ_{vap} further reduces the mass flux for lower temperatures.
- *Subfigs. 6.9(d)-6.9(f)*: The coefficient λ_{vap} does not correlate with either of the characteristic numbers Ja , R^+ and t^+ . Trends are observed if R_p and R_0^* are fixed (Subfig. 6.9(d)) or if R_p and T_0 are fixed (Subfigs. 6.9(e) and 6.9(f)) but in general the characteristic number can spread over several orders of magnitude for similar vaporisation coefficients.

To summarize, there is no apparent correlation of λ_{vap} with any of the characteristic quantities that would allow for an a priori estimate of the model parameter. Similar findings are made for the KR and SHFM closures as discussed in Appendix E.

An alternative modelling procedure for the calibration coefficients can be based on the reference solution (RPE). Since the results follow similar trends for the different vaporisation models we restrict this analysis to the HKR. With $\lambda_{\text{cond}} = 0.99\lambda_{\text{vap}}$, Eq. (3.20) can be rearranged to yield the vaporisation coefficient as

$$\lambda_{\text{vap,RPE}} = \frac{\dot{m}'' \sqrt{2\pi\mathcal{R}}}{\frac{p_{\text{sat}}}{\sqrt{T_{\text{liq}}}} - 0.99 \frac{p_{\text{vap}}}{\sqrt{T_{\text{vap}}}}}. \quad (6.1)$$

The reference solution provides the mass flux \dot{m}'' , the vapour pressure p_{vap} and the vapour temperature T_{vap} at $R = R_{\text{end}}$. The saturation pressure p_{sat} is determined as a function of the liquid bulk temperature $T_{\text{liq}} = T_{\infty}$. Figure 6.10(a) depicts the ratio between the calibrated coefficients $\lambda_{\text{vap,cal}}$ (Appendix D) and the coefficients $\lambda_{\text{vap,RPE}}$ from Eq. (6.1). The estimates $\lambda_{\text{vap,RPE}}$ differ from the calibrated coefficients, but the deviations are similar for constant R_0^* . For small R_0^* the mass flux in the RPE is larger than the mass flux in the DG solution. As a result $\lambda_{\text{vap,RPE}}$ is larger and $\lambda_{\text{vap,cal}}/\lambda_{\text{vap,RPE}}$ is smaller than one. The opposite applies for large R_0^* and Fig. 6.10(b) confirms this theory. The red line in Fig. 6.10(a) is a least-squares fit of the data points, which can be used to approximate $\lambda_{\text{vap,pre}}$ based on the initial estimation

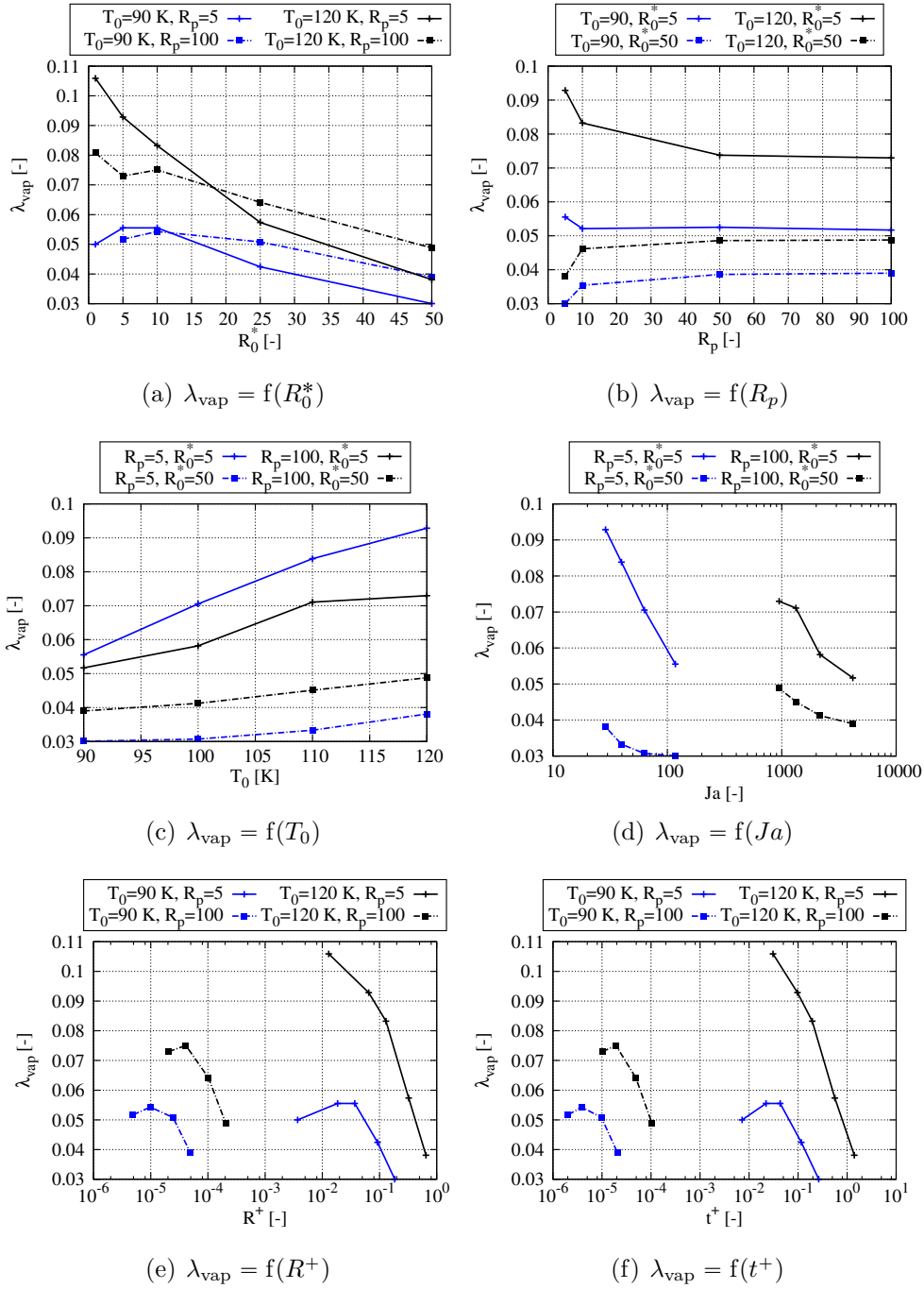


Figure 6.9: Vapourisation coefficients λ_{vap} as a function of different characteristic quantities of the investigation.

$\lambda_{\text{vap,RPE}}$ with

$$\lambda_{\text{vap,pre}} = \lambda_{\text{vap,RPE}} \cdot 1.27 \cdot (1 - \exp(-R_0^* \cdot 0.086))^{0.61}. \quad (6.2)$$

The largest deviation between $\lambda_{\text{vap,cal}}$ and $\lambda_{\text{vap,pre}}$ occurs for $R_p = 100$, $T_0 = 120$ K and $R_0^* = 5$. The predicted coefficient and the resulting volume expansion differ by approximately 45%. Figure 6.10(c) summarises these deviations for all test conditions. The error tends to decrease for increasing initial radii and Fig. 6.11 gives one possible reason for this trend. Here, the mass fluxes are normalized with the coefficient A of Eq. (5.8) and with the density of the saturated vapour in the bubble. The black lines show solutions from the RPE which converge after an initial highly transient stage into a single curve. The slope of this curve is approximately proportional to $(t^+)^{-0.5}$ and remains roughly constant within the time interval considered. The modelling of the early transients is rather complicated with the present method but the volumetric expansion (that is our target quantity) is small for these stages and the accuracy improves for the relaxed stages.

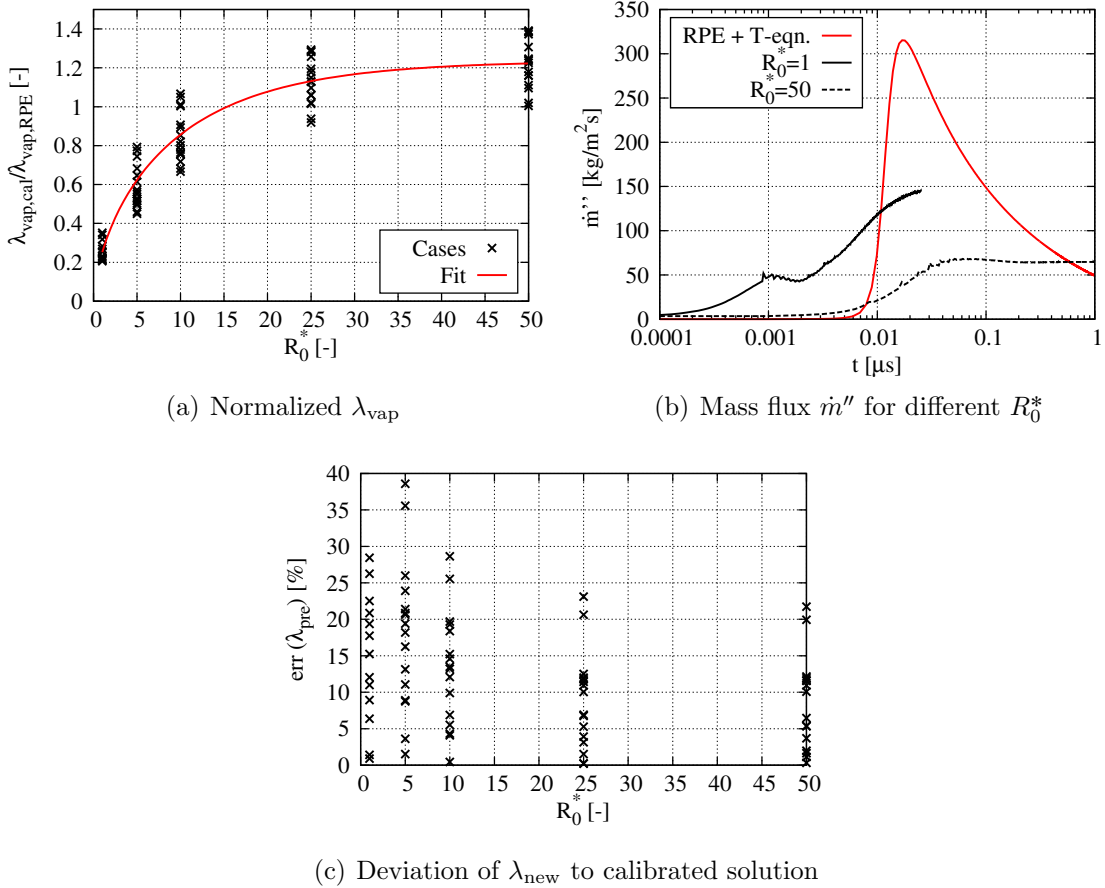


Figure 6.10: Comparison of estimated and calibrated λ_{vap} .

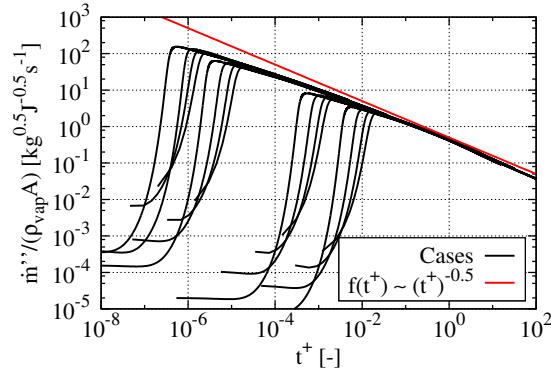


Figure 6.11: Vaporisation mass fluxes from the RPE normalized by the vapour density and the factor A in Eq. (5.8) as a function of the dimensionless time t^{+} . After an initial transient the curves for all cases approximately converge to a single curve.

6.3 Sensitivity analysis for the model coefficients and DNS results

The preceding sections discussed the dependency of the coefficients of the vaporisation models to the physical initial conditions and the initial bubble radii. This section discusses the sensitivity of the DNS results to changes in the model coefficients for fixed initial conditions.

Figure 6.12 depicts the bubble radius as a function of time for different physical parameters and vaporisation models. The red and black lines represent the calibrated results and results with a 10% change in the model coefficient, respectively. In all cases, an increase or decrease in the coefficient yields faster or slower bubble growth. The maximum difference in the bubble radii between the calibrated and the disturbed solutions lies between 2% and 10%. The difference in the radius is smaller than the change in the coefficient for some of the cases because the density of the fresh vapour also changes. An increase in the mass flux as a result of a change in the coefficient yields an increased density and the volume expansion reduces. The inverse effect is observed if the mass flux decreases. The results show that an calibration of the vaporisation models is essential to compute the bubble expansion accurately with the DNS procedure in use. At the same time, the deviation in the coefficient is not equal to the deviation in the resulting growth rate.

The result of the calibration was also compared for different numerical setups.

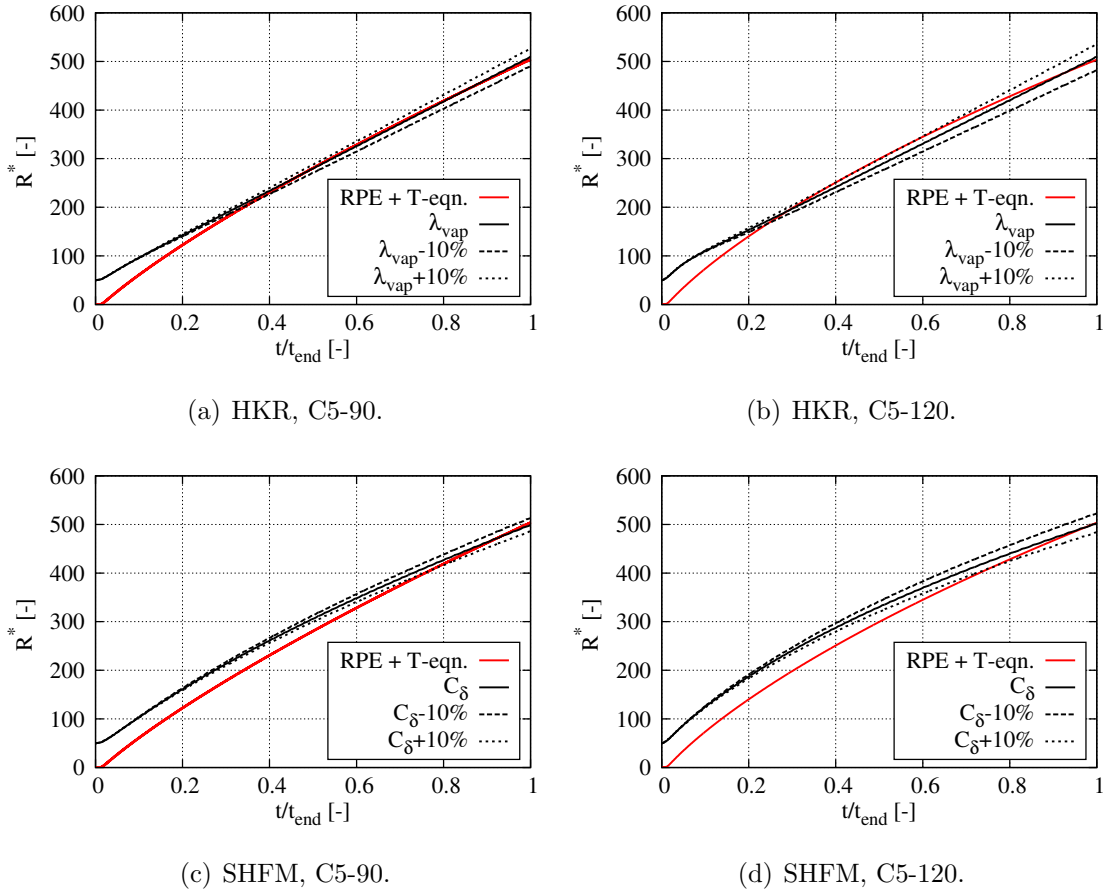


Figure 6.12: Sensitivity of the bubble radius to a 10% change in the model coefficient. All cases use $R_0^* = 50$.

The errorbars in Fig. 6.13 indicate the deviation for the calibrated coefficients of the HKR for different mesh and time resolutions. The diagram shows the errorbars for $R_0^* = 5$ and $R_0^* = 25$ as well as $R_p = 5$ and $R_p = 10$ as a function of time. The influence of the numerical parameters is small compared to the change of λ_{vap} with T_0 , R_p and R_0^* . Therefore, the calibration of the model coefficients represents an adaption with respect to the physical conditions and it is not significantly affected by the numerics.

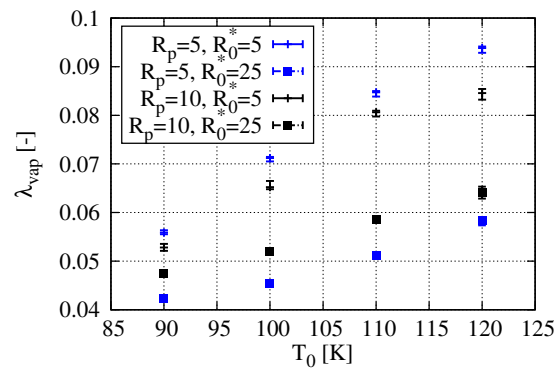


Figure 6.13: Influence of the numerical setup (mesh and time resolution, initial pressure) to the calibrated coefficients of the HKR.

CHAPTER 7

Bubble expansion in superheated jets

Chapters 5 and 6 discuss single bubble growth as the essential reference case and its simulation with the DG solver. Flash boiling is, however, a phenomenon where multiple bubbles occur. Findings based on single bubble models and simulations are not necessarily applicable to cases with multiple bubbles. Therefore, the present chapter studies the growth of interacting bubbles and compares the resulting growth rates to the cases of Ch. 6. The setups of Ch. 7 represent a section of a superheated liquid jet and are introduced in Sec. 7.1. Section 7.2 provides the results of the simulations with multiple bubbles and the comparison to the single bubble cases. Finally, Sec. 7.3 suggests closure conditions for the LES of flash boiling jets which are based on the present computations.

7.1 General setup

Section 2.1.2 discusses the role of bubble nucleation for flash boiling and summarises some of its fundamental aspects. The nucleation rate determines the bubble number density after a certain time interval. The present work does not include the nucleation process itself but uses the bubble number density as a free parameter characterising the bubble distance. The bubbles are arranged in regular arrays such that equal bubble growth of all bubbles would result in a close packing configuration at the end of the computations. The uniform bubble distance is D_{bub} and the

resulting distances in the Cartesian reference frame are¹

$$\begin{aligned} D_{x,\text{bub}} &= D_{\text{bub}}, \\ D_{y,\text{bub}} &= \frac{D_{\text{bub}}}{\sqrt{2}}, \\ D_{z,\text{bub}} &= \frac{D_{\text{bub}}\sqrt{6}}{3}. \end{aligned} \quad (7.1)$$

The distance between the bubbles is defined as a multiple of the initial radius with

$$D_{\text{bub}} = \Psi_{\text{bub}} R_0, \quad (7.2)$$

using $\Psi_{\text{bub}} = 10$. The bubble number density is directly related to the bubble distance by $N_{\text{bub,dens}} = 1/(D_{x,\text{bub}}D_{y,\text{bub}}D_{z,\text{bub}})$. The number densities can be varied by either modifying Ψ_{bub} or R_0 . Using i.e. $\Psi_{\text{bub}} < 10$ leads to jet break-up in the very early stages of bubble growth, the dynamics of the growth process itself seem less significant and modelling of the spray at the nozzle exit as droplet clouds without primary break-up may be favourable. Instead, the bubble number density is modified by varying $R_0^* = R_0/R_{\text{crit}}$ by a factor of 50 which leads to variations in bubble number densities by more than five orders of magnitude. Note that for large multiples of initial bubble radius, i.e. $\Psi_{\text{bub}} \gg 10$, the early stages of bubble growth will not increase the volume of the jet. This can be shown analytically by [26]

$$V^* = \frac{V_{\text{jet,end}}}{V_{\text{jet,0}}} = 1 + \sqrt{3} \frac{\pi}{0.75 \Psi_{\text{bub}}^3} (R^{*3} - 1)(1 - \rho^*) \quad (7.3)$$

which describes the ratio of a cylindrical volume after and before bubble growth. The derivation of this equation is given in Appendix F. Figure 7.1 depicts V^* as a function of the dimensionless bubble radius R^* for different initial bubble spacings Ψ_{bub} . Starting from the critical radius at $R_0^* = 1$ the jet volume will not increase as long as the condition $\frac{\Psi_{\text{bub}}}{R^*} > 10$ holds. This, again, supports the omission of early stages of bubble growth and justifies the variation of the bubble number density by changing R_0^* only. The parameter Ψ_{bub} is kept constant throughout this work.

¹A close-packing of spheres may be defined by an array consisting of regular tetrahedrons and the center of the spheres would be located at the vertices of the tetrahedrons. If one edge of the tetrahedron is parallel to the x-direction in a Cartesian reference frame, the distance of the vertices in y-direction can be defined as the height of a regular triangle, i.e. $D_{y,\text{bub}} = \sqrt{3}/2 D_{\text{bub}}$. Here, the distance in y-direction is $D_{y,\text{bub}} = 1/\sqrt{2} D_{\text{bub}} < \sqrt{3}/2 D_{\text{bub}}$ resulting in an increased bubble count in y-direction by 20%.

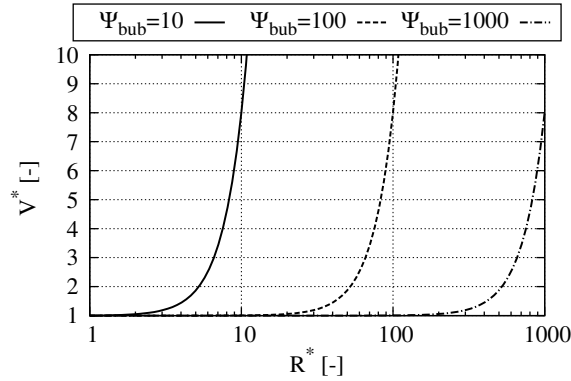


Figure 7.1: Ratio between final jet volume and initial jet volume according to Eq. (7.3). If the bubble distance is large compared to the initial radius, i.e. Ψ_{bub} is large, then the early stages of bubble growth do not contribute to the expansion of the liquid jet.

A typical nozzle diameter for the experiments at DLR [58] is $D_{\text{noz}} = 0.5$ mm. Resolving the bubbles of the critical size at $T_0 = 100$ K and $R_p = 5$ ($R_{\text{crit}} = 0.1 \mu\text{m}$) with 8 FV sub-cells across its diameter would require 20000 cells along the nozzle radius alone rendering a fully three-dimensional computation unfeasible. Therefore, the geometric configuration should be simplified and errors associated with the simplification should be assessed. As a first approximation the jet is represented by a column with one row of fully resolved bubbles in its center. Figure 7.2 shows a sketch of the computational domain. Note the orientation of the coordinate system with its origin positioned at the gas-liquid interface. Symmetry boundary conditions in the y - and z -directions as well as in the positive x -direction mimic the close packing of bubbles. In the negative x -direction a low pressure vapour reservoir allows for the expansion of the liquid column. The different fluid states are the same as described in Fig. 2.3: The liquid is superheated at state B and it contains saturated vapour bubbles at state C. The pressure in the vapour reservoir (state D) is below the saturation pressure for the local temperature. This simplified setup includes essential physical aspects of flashing flows and allows to conduct first qualitative and quantitative investigations at reduced computational cost. This setup is referred to as Setup 1 in the remainder of this work. For Setup 2 the approximation of the jet's geometry is improved. The liquid bulk is now represented by a cylindrical slice which can expand to the negative x - and y -directions, while the z -directions and the positive x - and y -directions are treated as symmetry planes, see the illustration on the top right in Fig. 7.2. This setup is expected to represent fluid within the jet and away from the leading edge. Setup 3 is depicted in the

bottom right of Fig. 7.2, it additionally allows for an expansion of the liquid to the negative z-direction and represents fluid at the leading tip. The representation of the actual jet geometry improves from Setup 1 to Setup 3 but the computational effort also increases. The deviations in the bubble growth rates for the different geometries and the suitability of Setup 1 to represent jet expansion are discussed in Sec. 7.2.2.

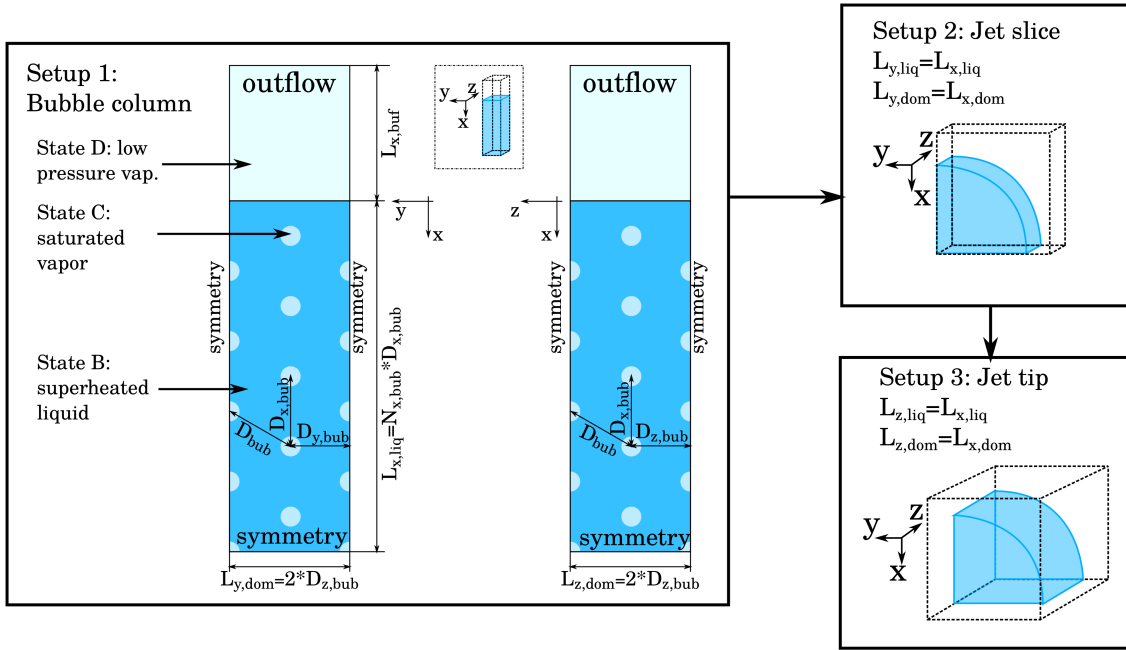


Figure 7.2: Different geometrical setups for the investigation of multiple bubble growth in superheated liquids. The fluid states B, C and D are labelled according to Fig. 2.3.

A second important aspect of the configuration is the thickness of the liquid layer, i.e. $L_{x,liq}$ in Setup 1, $L_{x,liq}$ and $L_{y,liq}$ in Setup 2 and additionally $L_{z,liq}$ in Setup 3. The thickness $L_{x,liq}$ is defined by the number of bubbles in x-direction and the bubble distance by

$$L_{x,liq} = N_{x,bub} \cdot D_{x,bub}. \quad (7.4)$$

In Setup 1, the thicknesses in y- and z-directions are given by $L_{y,liq} = 2D_{y,bub}$ and $L_{z,liq} = 2D_{z,bub}$, respectively. The dimensions of Setup 2 and 3 are set to $L_{y,liq} = L_{x,liq}$ and $L_{z,liq} = L_{y,liq} = L_{x,liq}$. The bubble column in Fig. 7.2 contains, e.g., five bubbles in x-direction. The size of the low pressure reservoir is defined by $L_{x,buf} = 0.5 \cdot L_{x,bub}$. Setup 1 is the reference for analysing the dependency of the

bubble growth rates on the thickness of the layer, i.e. on the number of bubbles resolved in a certain spatial direction. These results are also discussed in Sec. 7.2.2.

Table 7.1 summarises the default geometrical and numerical parameters. The mesh is equidistant and resolves the initial bubble radius with four FV sub-cells. Thus, the total number of cells will not depend on the physical parameters T_0 , R_p and R_0^* but only on the geometrical configuration and the number of bubble layers. A sensitivity study varying the parameters in Tab. 7.1 shows a small influence on the numerical parameters, only. An increase of the mesh resolution or of the buffer zone size changed the resulting bubble radii by less than five percent. The CFL condition has a larger effect only for very small CFL numbers. However, the smaller CFL numbers caused larger mass losses as the level-set approach and the ghost fluid method used in the interface Riemann solver are inherently not mass conserving. With $CFL = 0.1$ mass losses have been of the order of five percent while it has been around one percent with $CFL = 0.9$ and $CFL = 0.9$ is therefore used. The investigation of multiple bubble growth uses the HKR as given in Eq. (3.20) or the SHFM as in Eqs. (3.22) and (3.23) to model vaporisation. The model coefficients are taken from the investigation in Ch. 6, see also Appendix D.

Table 7.1: Geometrical and numerical parameters.

Parameter	CFL	$R_0/\Delta x$	Ψ_{buffer}	Ψ_{bub}
Value	0.9	4	0.5	10

7.2 Results

The reference test case uses an initial temperature of $T_0 = 120$ K, $R_p = 5$ and $R_0^* = 50$. Section 7.2.1 shows the corresponding results using Setup 1. Section 7.2.2 discusses two aspects. Firstly, the bubble growth is compared for Setups 1, 2 and 3 and the influence of the geometrical simplification is analysed. Secondly, the height of the liquid column $L_{x,\text{liq}}$ is varied for Setup 1 resulting in a variation of the bubble number. Bubbles at the bottom of the column (i.e. in the jet center) are assumed to grow more slowly than bubbles close to the surface. If the growth of the innermost bubbles becomes independent at a certain $L_{x,\text{liq}}$ bubble growth for bubbles located at $x > L_{x,\text{liq}}$ will be known, these bubbles do not need to be included in the computations and the domain size could be reduced in x-direction

to $x_{\max} = L_{x,\text{liq}}$. Based on the parameter studies presented in Sec. 7.2.2 the setup for the subsequent computations is chosen. This setup is then used in Sec. 7.2.3 to analyse the deviations of bubble growth within bubble clusters when compared to single bubble growth. The dependency of the results on the independent parameters T_0 , R_p and R_0^* is discussed in Sec. 7.2.4.

These studies are used to analyse the sensitivity of results on numerical parameters and physical process conditions and are conducted using the HKR only. Finally, Sec. 7.3 proposes growth correlations for bubbles in flash boiling jets. Here, the performance of the two closures for the evaporative mass flux, HKR and SHFM, is also compared.

7.2.1 Setup 1, C5-120

Figure 7.3 depicts contour plots of pressure and density at three different time steps for the bubble column configuration. The blue iso-surfaces indicate the interfaces between the bubbles and the superheated liquid. Bubbles that are closer to the low pressure reservoir at the top of the domain grow faster than bubbles at the bottom. Figure 7.3 also shows that the pressure increases towards the bottom of the bubble column. This pressure rise decreases the local evaporation rates at the bubble surface. Figure 7.4(a) depicts the mass flux at the interfaces of the outermost (top) and innermost (bottom) bubble, respectively. The mass flux for the outermost bubble is approximately 50% higher than that of the innermost bubble. This is consistent with Eq. (3.20) where an increased mass flux results from a decreasing vapour pressure. The lower pressure at the top of the bubble column (cf. Fig. 7.3) therefore yields the increased evaporative mass flux. Figure 7.4(b) depicts the corresponding density profiles. The vapour density at the bottom of the bubble column is approximately double the vapour density for the outermost bubble. The differences in the mass flux and in the vapour densities are responsible for the smaller growth rates of the outer and inner bubbles. Figure 7.5 shows the normalized bubble radius R^* as a function of the normalised position x/D_{bub} of the bubble within the column at $t = 0.5 \mu\text{s}$. The outermost bubble (close to the surface with low x/D_{bub}) grows twice as fast as the innermost bubble. In the following section these results are compared to Setup 2 and Setup 3 and to cases with an increased $L_{x,\text{liq}}$.

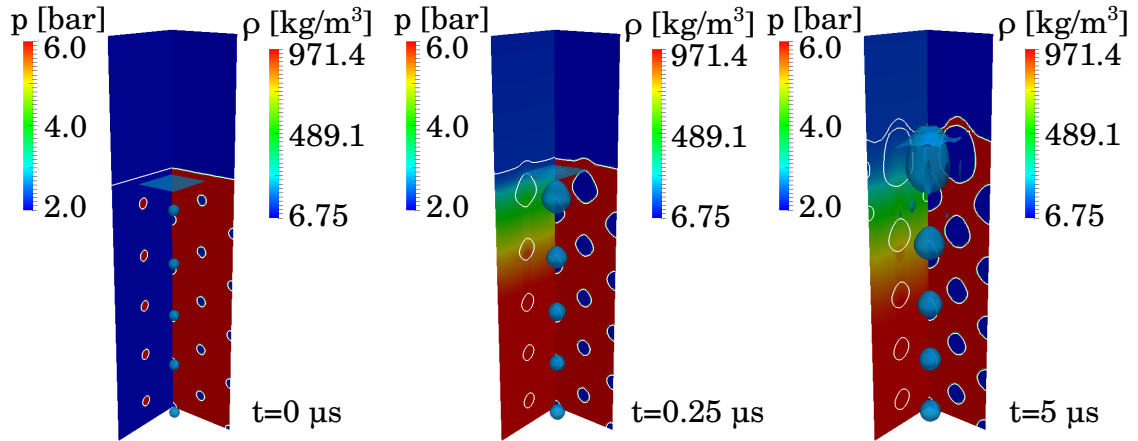


Figure 7.3: Contour plots of the bubble column test case for three different time steps with five bubble rows along the x-direction. The left plane and right plane show the time averaged pressure field and the density field, respectively. The blue coloured iso-surfaces indicate the interfaces between bubbles and superheated liquid.

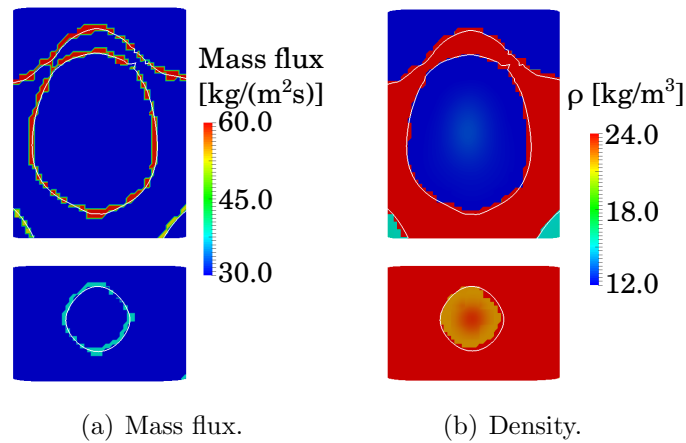


Figure 7.4: Mass flux and density contours of the outermost (top) and innermost (bottom) bubble for case C5-120 with $R_0^* = 50$ at $t = 0.5 \mu\text{s}$.

7.2.2 Geometry and bubble number variation

The reference case C5-120 with $R_0^* = 50$ is now used to compare different geometrical setups. The black, blue and red symbols in Fig. 7.6 show the normalised radii at $t = 0.35 \mu\text{s}$ for Setup 1, Setup 2 and Setup 3, respectively. Bubbles at the same distance from the "jet" interface grow more slowly for Setup 1 than for Setups 2 and 3. For the latter setups more than one bubble can exist for a given distance and due to the symmetry conditions, only few scatter exists for Setup 2. However, scatter becomes larger for Setup 3 as bubbles at the jet tip experience a different pressure field than bubbles at the jet edge (for a comparable x). Therefore,

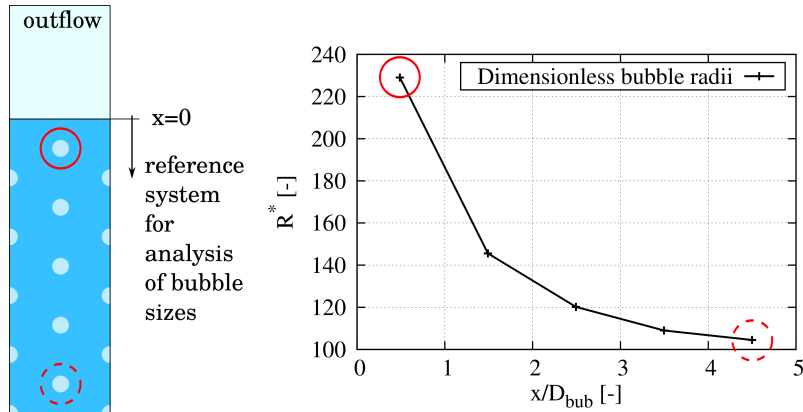


Figure 7.5: Normalised bubble radius as a function of the distance to surface.

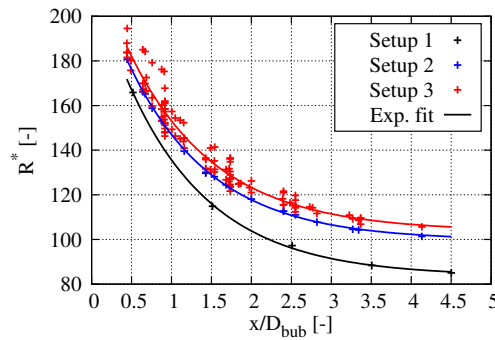


Figure 7.6: Dimensionless bubble radii for different geometries using C5-120 with $R_0^* = 50$. The black, blue and red symbols represent the numerical data for Setup 1, Setup 2 and Setup 3, respectively. The solid lines show the corresponding exponential fits.

least-squares exponential fitting functions $R^* = f(x)$ (solid lines) are introduced for guidance of the eye and for better comparison. Setup 1 deviates from Setup 3 by a maximum of 20%, while Setup 2 underestimates bubble expansion by 5% only. Computational requirements increase, however, by a factor of 4.4 when comparing Setup 3 with Setup 2. The error of 5% seems acceptable and representation of the jet configuration by Setup 2 appears sufficiently accurate as computational efficiency becomes a critical issue if the number of bubble rows needs to be large. This is discussed in the next paragraph.

Figure 7.7 shows the normalised bubble radii R^* for C5-120, $R_0^* = 50$ and Setup 1 varying the number of bubbles in x -direction. The differences are rather small for bubbles close to the bulk liquid interface but grow with increasing x . With an increasing number of bubbles these deviations become smaller. The solid lines in Fig.

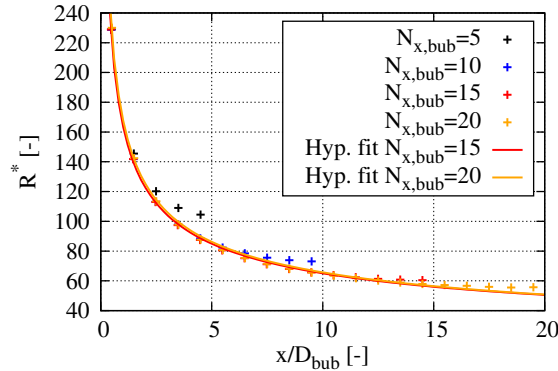


Figure 7.7: Dimensionless bubble radii for different numbers of bubbles rows using C5-120, $R_0^* = 50$ and Setup 1 at $t = 0.5 \mu\text{s}$.

7.7 show least-squares hyperbolic fitting functions for the cases using $N_{x,\text{bub}} = 15$ and $N_{x,\text{bub}} = 20$. Here, hyperbolic fits are chosen over exponential fits to improve the match for large x/D_{bub} . Bubble radii gently decrease with increasing x for $x/D_{\text{bub}} > 10$. The estimations of R^* based on the fitted functions in Fig. 7.7 compare very well deviating by less than 1% for $x/D_{\text{bub}} > 10$. It is seen that at large enough distances ($x > 15D_{\text{bub}}$), the bubble's relative location to the bulk liquid interface becomes unimportant as bubble growth rates differ little. These small differences will have negligible effect on the overall expansion rate of the jet and computations including the outer liquid jet layer of a thickness of $15D_{\text{bub}}$ will suffice to completely characterise bubble expansion of groups of bubbles and their interactions. Therefore, the remaining investigation uses Setup 2 with a layer thickness of $L_{x,\text{bub}} = L_{y,\text{bub}} = 15D_{\text{bub}}$. The resulting mesh contains 55 mio degrees of freedom and gives an acceptable compromise between accuracy and computational cost.

7.2.3 Reference case: Setup 2, C5-120

All results demonstrate that bubbles in the center of a superheated jet grow more slowly than bubbles closer to its surface. This implies that bubble growth rates within bubble clusters - at least for the majority of the bubbles - are smaller than those obtained from single bubble models and single bubble growth models will lead to significant mistakes if applied indiscriminately. In the following, bubble radii and bubble growth rates for bubbles in the cluster are compared to those of single bubble simulations and potential errors that single bubble models will induce shall be quantified. Therefore, the normalised bubble radius and the normalised growth

rate are introduced as R/R_{sb} and \dot{R}/\dot{R}_{sb} , respectively. The index *sb* refers to the results from simulations of a single bubble in Ch. 6. Moreover, a reduced radius is defined by $(R - R_0)/(R_{sb} - R_0)$. Figure 7.8(a) depicts the normalised bubble radii as a function of their position relative to the jet surface. The outermost bubbles grow 20% more slowly than a single bubble. The bubble radii decrease exponentially with increasing distance from the jet surface. The differences to the single bubble are relatively independent of time for the outermost bubbles, but increase with time for bubbles further away from the jet interface. This effect is explained with the aid of Figure 7.8(b). Here, the black symbols show the reduced bubble radius as a function of the distance to the jet surface. The inner bubbles grow extremely slowly and hardly change their sizes. This slow growth then leads to a continuous decrease of the ratio R/R_{sb} with time. Figure 7.8(b) also shows that the reduced bubble size is rather invariant with time and that bubbles at distances from the interface larger than $x/D_{bub} = 15$ will not contribute to the liquid jet expansion, justifying again the reduction of the domain suggested in Sec. 7.2.2. The black symbols in Fig. 7.8(b) include all time steps beyond an initial transient stage after an initial pressure wave has propagated through the entire liquid layer. This time limit is proportional to a characteristic time

$$\tilde{t} = \frac{D_{bub}}{c_{liq}} \quad (7.5)$$

and is defined by

$$t_{ini} = N_{x,bub}\tilde{t}. \quad (7.6)$$

The red line represents an exponential fit with

$$\frac{R - R_0}{R_{sb} - R_0} = \exp\left(-0.48\frac{x}{D_{bub}} + 0.2\right)0.042. \quad (7.7)$$

One further target quantity is the total volumetric expansion of the jet. The present setup includes 221 fully resolved bubbles (bubbles at the symmetry planes are not counted) and the expansion of the 221 bubbles, and therefore of the jet slice, is now approximated in two ways. The first option assumes a uniform expansion of all bubbles. The volume change is added for each bubble using the single bubble solution in Ch. 6. The second option takes into account the location x/D_{bub} of the individual bubbles and calibrates the single bubble solution with the aid of Eq. (7.7). Again, a summation of the volume change over all bubbles gives the total

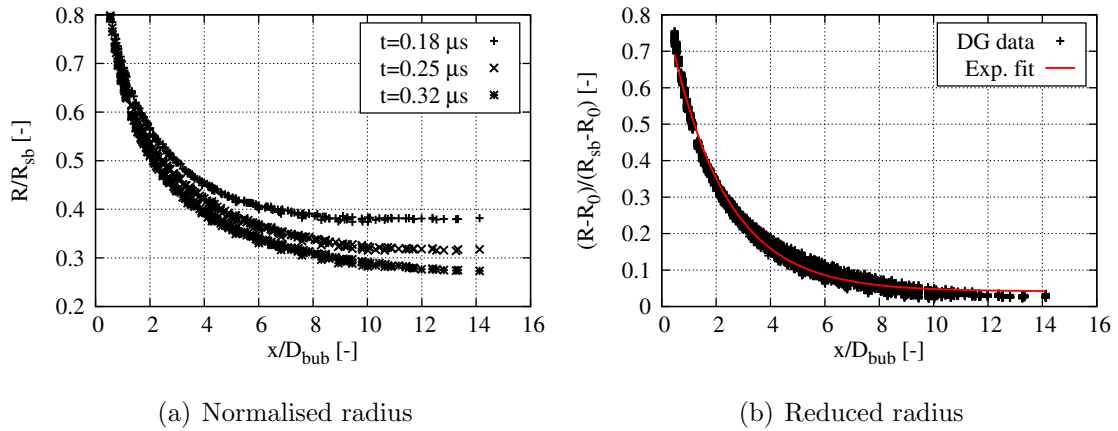


Figure 7.8: Setup 2, C5-120, $R_0^* = 50$: Comparison of the bubble radii to those of a single bubble.

volumetric expansion. Both options account for the loss of liquid volume due to vaporisation. The resulting dimensionless jet volume is depicted in Fig. 7.9 up to $0.45 \mu s$. This marks a minimum time bubbles need to grow before they merge under the present conditions. The corresponding growth factor of 5 allows to close the initial bubble distance of $10R_0$. The actual time needed will be higher, because bubbles will push each other apart and growth rates are smaller in bubble clusters. After $0.45 \mu s$ the volume of the liquid jet has increased by less than 5% using the exponentially fitted growth rates. In contrast, the single bubble model gives a volume increase of approximately 75% in the same time interval. The final volumes differ by 66%, it is identified as the the minimum error associated with the usage of the single bubble model and it will increase if bubbles coalesce at later times. This emphasizes the impact of bubble interactions on the expansion of superheated liquid jets.

The present results illustrate the dependency of the bubble radius on its location relative to the jet surface. The general goal of this investigation is the development of improved LES sub-grid models for flash boiling. Such models require closure for the phase change at a sub-grid scale and are typically formulated as mass or volume generation rates. Therefore, the growth rate \dot{R} of individual bubbles in the jet is analysed now. Figure 7.10(a) shows the normalised growth rates as a function of the relative distance to the jet surface. They decrease exponentially towards the jet center, similar to the bubble radii. For $x/D_{bub} \lesssim 3$, \dot{R}/\dot{R}_{sb} is time invariant, but it depends on time for bubbles further away from the interface. In Sec. 7.2.1 the

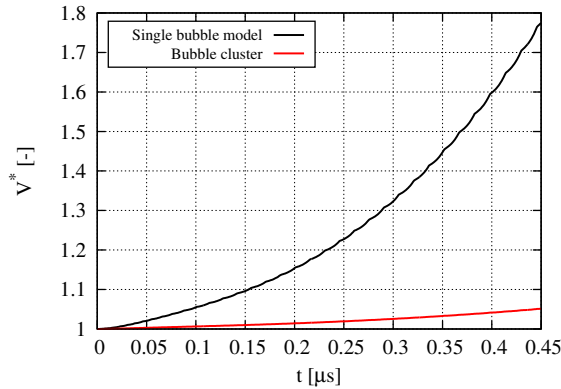


Figure 7.9: Dimensionless volume of cylindrical jet according to Eq. (7.3) with $R^* = f(t)$ given by single bubble growth rates (black line) and by Eq. (7.7).

dependency of the bubble growth rate on the local pressure field was discussed. A low liquid pressure allows for higher mass fluxes and bubbles grow faster. Figure 7.3 demonstrates that the low pressure conditions propagate towards the jet center in time. With a decrease in the local pressure the growth rate of the bubbles will increase. In contrast, the pressure rapidly converges to a relatively steady solution in the single bubble DNS, the increased pressure level is not maintained in the absence of additional interacting bubbles. Thus, \dot{R}/\dot{R}_{sb} changes as the local pressure in the jet changes. Close to the jet surface, the pressure conditions remain constant and both, \dot{R}/\dot{R}_{sb} and \dot{R} do not change in time. The innermost bubbles also face constant pressure conditions for the time interval considered, because the liquid is still pressurised. Bubbles at a medium distance face the largest change in the local pressure field and therefore, \dot{R} and \dot{R}/\dot{R}_{sb} depend on time. This temporal variation hinders adequate parametrization of growth rates for LES sub-grid closures and therefore Fig. 7.10(b) depicts the normalised bubble growth rate as a function of the local degree of superheat

$$R_{p,loc} = \frac{p_{sat}(T_{liq})}{p_{bub}}. \quad (7.8)$$

with p_{bub} defined as the average pressure in a bubble. Figure 7.10(b) shows a linear increase of \dot{R}/\dot{R}_{sb} with the local degree of superheat. The red line fits the DNS data with

$$\frac{\dot{R}}{\dot{R}_{sb}} = 0.33R_{p,loc} - 0.33. \quad (7.9)$$

This expression is time invariant and thus much better suited for the parameteriza-

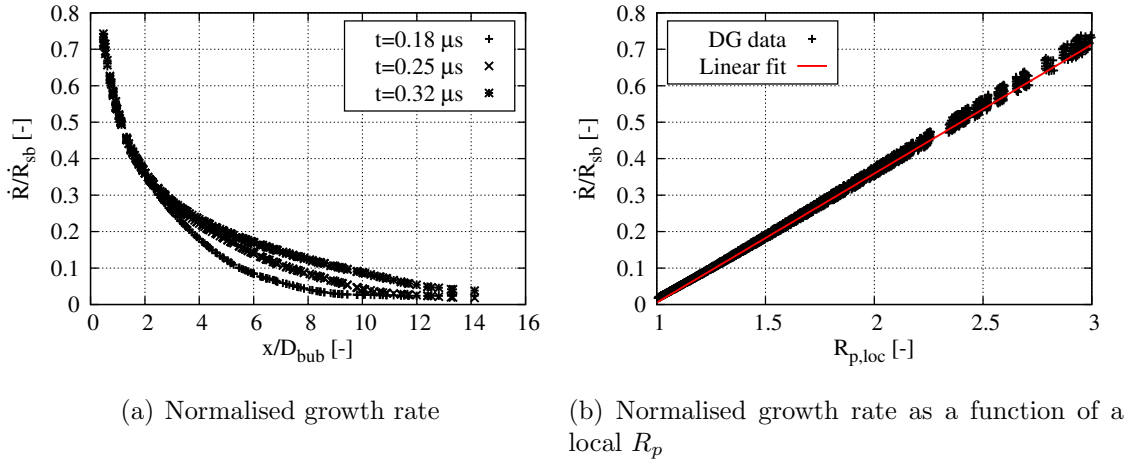


Figure 7.10: Setup 2, C5-120, $R_0^* = 50$: Comparison of the bubble growth rates to those of a single bubble.

tion of growth rates as part of modelling strategies. It may serve as the basis for the estimation of phase transfer rates in future LES simulations, where p_{bub} could be equivalent to the local pressure in one LES cell. A single LES cell will contain numerous bubbles and the local pressure would characterise the average growth rates which should - due to the linear relationship - be an adequate approximation of the vaporisation occurring at the sub-grid scales. In the following, the expressions of Eqs. (7.7) and (7.9) are compared for different initial conditions.

7.2.4 Parameter study

This section assesses the validity of the findings reported in Sec. 7.2.3 subject to a variation of the independent parameters T_0 , R_p and R_0^* . If not stated otherwise, diagrams show the DNS results and the corresponding least-square fits as black symbols and yellow solid lines, respectively. The red solid lines represent the fitting function of the reference case C5-120 with $R_0^* = 50$. Figure 7.11 compares the reduced bubble radii and the normalised growth rates for different temperatures. Subfigures 7.11(a) and 7.11(b) depict the change in the bubble radius as a function of the distance to the jet surface for $T_0 = 100$ K and $T_0 = 110$ K, respectively. Qualitatively, the results are similar across the temperature range, but the reduced radii decrease faster towards the jet center for a decreasing temperature. Within the time intervals considered $R_{p,loc}$ decreases with temperature for the same normalised distance x/D_{bub} being one indicator for the reduced bubble growth. The low-pressure condition propagates faster towards the jet center as the temperature

increases. However, a direct comparison is difficult because both, length and time scales change. Therefore, the $R_{p,loc}$ -to- T dependency is associated with a normalised time defined by $t^* = t/\tilde{t}$ using the expression in Eq. (7.5). This normalised time scale decreases with increasing temperature suggesting a faster characteristic propagation of the low pressure conditions towards the jet center. Subfigures 7.11(c) and 7.11(d) show the corresponding normalised growth rates as a function of the local degree of superheat. The linear dependency of \dot{R}/\dot{R}_{sb} on $R_{p,loc}$ also holds for $T_0 = 100$ K and $T_0 = 110$ K, but the slope increases with decreasing temperature. Note that the scatter for $T_0 = 100$ K stems from the early time steps as pressure waves propagate from the jet surface to the center.

Changing the initial pressure ratio R_p or the initial radius R_0^* confirms the present findings. Figure 7.12(a) depicts the reduced bubble radii of case C10-120. The cor-

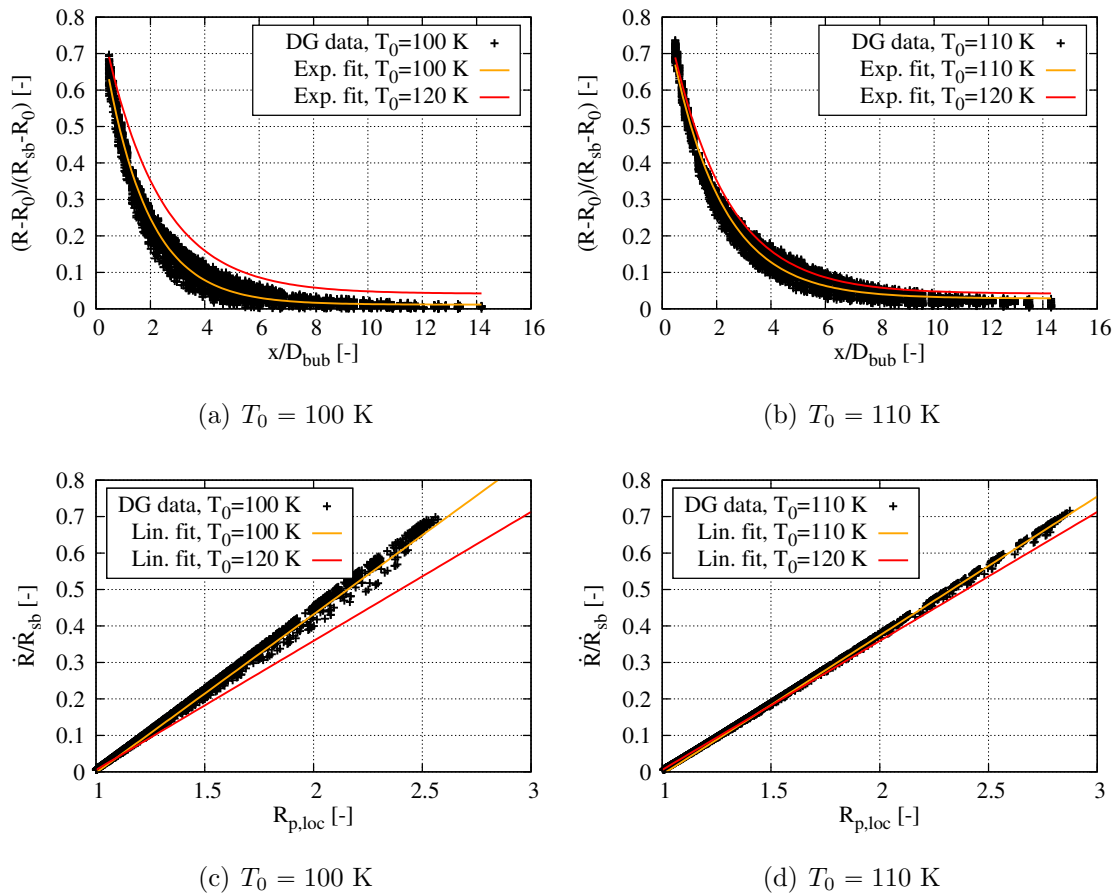


Figure 7.11: Setup 2, $R_p = 5$, $R_0^* = 50$: Normalised change of the radius and normalised growth rates.

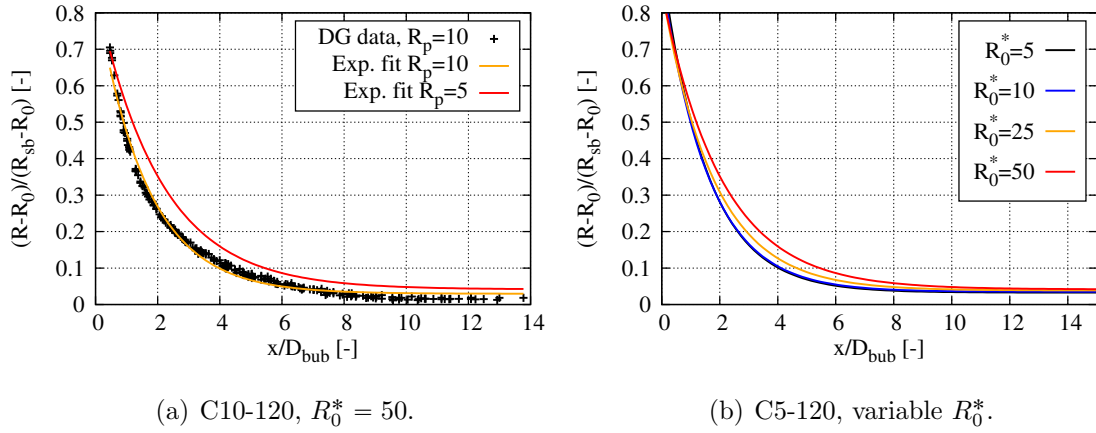


Figure 7.12: Reduced bubble radii.

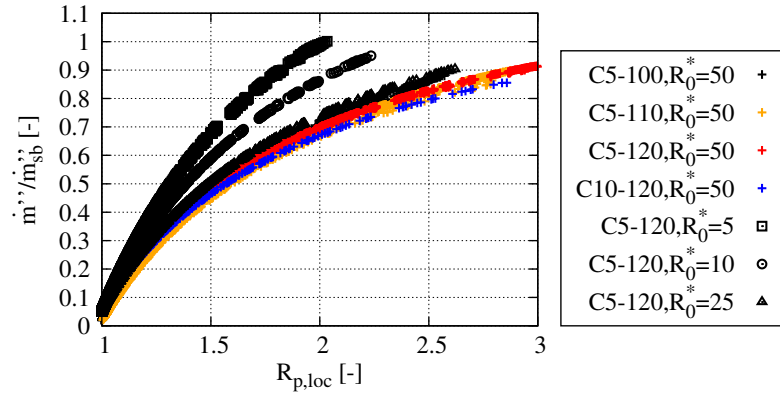


Figure 7.13: Setup 2: Normalised mass flux for different cases.

responding results with a variable R_0^* are given in Fig. 7.12(b). Here, the black, blue and yellow lines represent $R_0^* = 5$, $R_0^* = 10$ and $R_0^* = 25$, respectively. The exponential decrease of the reduced bubble radius is in a similar range for the different initial conditions. Figure 7.13 depicts the normalised mass flux as a function of $R_{p,loc}$ varying all independent parameters. While the case with the pressure ratio $R_p = 10$ shows a similar dependency of \dot{m}''/\dot{m}_{sb}'' on $R_{p,loc}$ as the cases with $R_p = 5$, differences occur if the initial radius decreases. This is associated with the increased surface tension. For the same surrounding pressure the bubble pressure is higher at smaller radii. This applies to both, the single bubble DNS and the multiple bubble DNS. Therefore, the same massflux, i.e. $\dot{m}''/\dot{m}_{sb}'' \approx 1$ is obtained for a lower $R_{p,loc}$.

The present investigation shows that bubble growth rates within liquid jets significantly deviate from single bubble models. The data base for the single bubble

growth is obtained using a constant ambient pressure. This applies also to the reference database obtained from the Rayleigh-Plesset equation. In principal, the Rayleigh-Plesset equation can also be solved with a time varying pressure field. This is done subsequently using the average liquid pressure field of the outermost and innermost bubbles for case C5-120 with $R_0^* = 50$. Figures 7.14(a) and 7.14(b) show the average liquid pressure field surrounding the outermost and innermost bubbles, respectively. The black lines show the instantaneous pressure and the red lines fit these data to exponential functions such that a smooth pressure curve is obtained. Both time profiles are used as input for the Rayleigh-Plesset equation and the resulting radii are compared in Figs. 7.14(c) and 7.14(d) for the outermost and innermost pressure field, respectively. Here, the initial radius for the Rayleigh-Plesset equation needs to be increased as well because otherwise the rapidly increasing pressure would lead to bubble collapse. In both cases, the growth rates are comparable for the DG solver and the Rayleigh-Plesset equation with time varying pressure fields. The use of the RPE as a sub-grid closure seems therefore acceptable, if it is solved on-the-fly using the local pressure of the macroscopic simulation. Bubbles would need to be tracked in a Lagrangian manner and if the bubble number is high the computational effort may increase considerably. In Sec. 2.4 the potential of the Σ - Y -model to represent different flash boiling regimes was discussed. Here, transport equations for the volume fraction and surface density are solved as Eulerian fields and individual bubbles are not tracked. Therefore, Sec. 7.3 discusses empirical correlations allowing to estimate the mass flux or the bubble growth rate without on-the-fly computation of the Rayleigh-Plesset equation.

7.3 Derivation of model equations for the LES of flash boiling jets

The correlations that have been shown in the previous sections help to assess errors associated with models based solely on single bubble expansion rates. However, they do not necessarily provide suitable LES subgrid models. Above correlations require single bubble growth as a function of conditions at the interface between the core liquid jet and the low pressure surroundings. Corrections from single bubble growth could be modeled as functions of distance from this interface. This may be cumbersome and impractical in a complex, convoluted 3-D liquid jet. Alternatively, normalised growth rates or mass fluxes may be estimated as functions of a

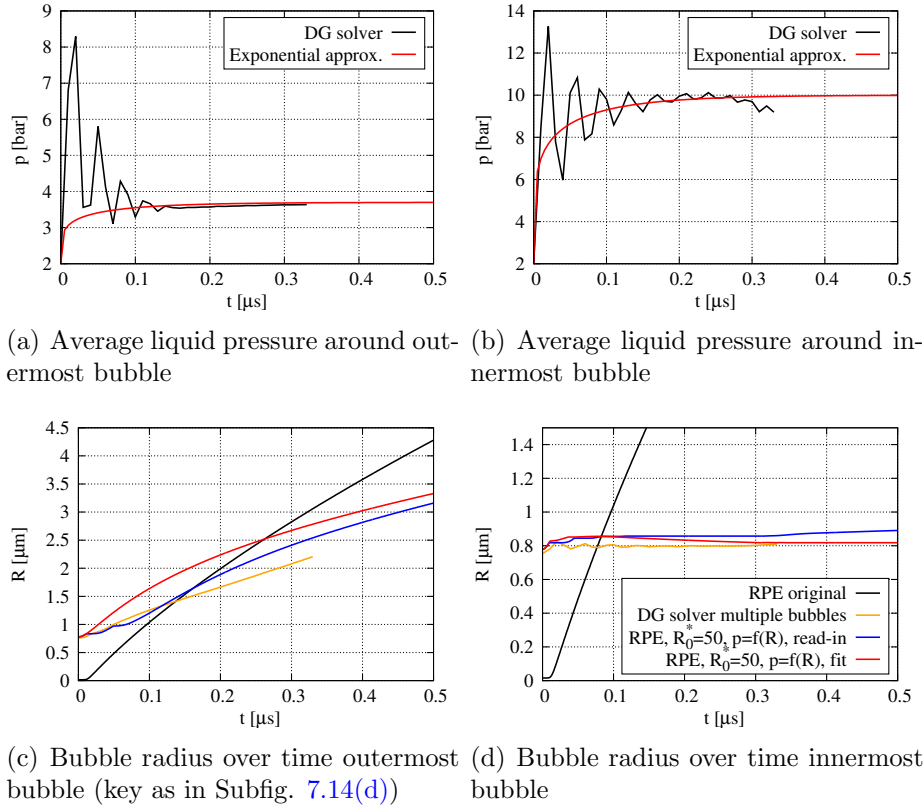


Figure 7.14: Comparison of bubble radii from the multiple bubble DNS to the Rayleigh-Plesset equation solved with a time dependent pressure field.

normalised local pressure difference, see Fig. 7.15. The dependency is similar for different initial conditions and may be approximated by the linear relation based on the solution of the single bubble model. Regarding the formulation of an LES model this approximation has two main disadvantages. Firstly, the single bubble solution needs to be determined as a function of time. In the context of a two-equation model (see Sec. 2.4.1) bubbles are not tracked and the lifetime of individual bubbles is therefore unknown. Alternatively, the single bubble data may be obtained as a function of the bubble radius. However, the mass flux given by the Rayleigh-Plesset solution peaks at small radii. Thus, the small bubbles in the center would experience unphysically strong growth. Secondly, the source terms in two-equation models such as the Σ - Y -model are needed for the surface density and the volume fraction. The mass flux can be transferred to a volumetric flux dividing it by the vapour density. In the LES only mixture properties are available in the computational cell and an estimation of the density is not straight forward. A suitable closure condition for the surface and volume production/destruction rates in a two-equation model may

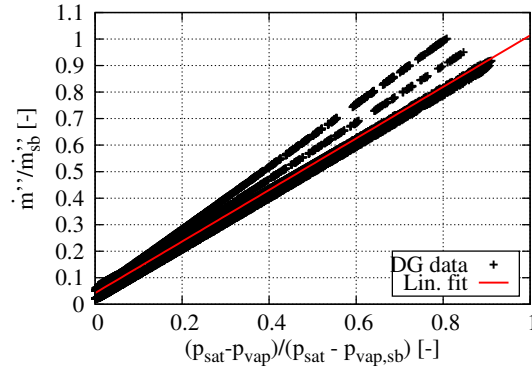


Figure 7.15: Setup 2, Normalised mass flux as a function of a normalised local pressure difference.

be based on bubble growth rates, i.e. \dot{R} , as a function of local filtered quantities.

Figure 7.16 depicts the bubble growth rate \dot{R} normalised by the bubble parameter A from Eq. (5.8) as a function of a normalised pressured difference. Here, the filtered pressure, \tilde{p}_{LES} , is represented by an average from all cells in a distance of half the initial bubble spacing ($0.5D_{bub}$) from the bubble center. The subfigures 7.16(a) and 7.16(b) show results for the HKR and the SHFM, respectively. The symbols originate from DG simulations and are the bubble growth rates of all bubbles at different times. The different cases are identified by different colours and symbols. The figures also include possible global fits using exponential (HKR) or hyperbolic (SHFM) functions that read

$$\frac{\dot{R}}{A} = 0.11\exp(1.72\Delta p^*) - 0.12 \quad (7.10)$$

and

$$\frac{\dot{R}}{A} = 0.3\sinh(1.52\Delta p^*) + \tanh(-49.42\Delta p^{*2} - 31.53) + 1.0, \quad (7.11)$$

respectively, where $\Delta p^* = \frac{p_{sat}(T_\infty) - \tilde{p}_{LES}}{p_{sat}(T_\infty) - p_\infty}$. A functional dependence of \dot{R} on $(p_{sat} - \tilde{p}_{LES})$ has two advantages: Firstly, the phase transfer is expressed as a bubble growth rate allowing for a straight forward estimation of vaporisation source terms. The bubble growth rates can be obtained from simple computations and do not require fits from experimental data that are usually not available. Secondly, the growth rates are expressed in terms of a locally filtered quantity as it is typically available in LES. It is apparent that each case correlates well with the pressure difference but one

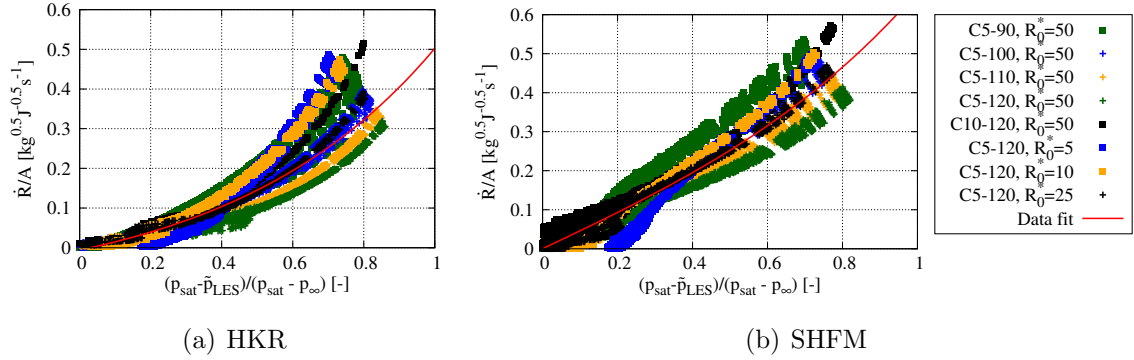


Figure 7.16: Bubble growth rate normalised by the bubble parameter $A = \sqrt{\frac{2}{3} \frac{h_{fg} \rho_{vap} (T_{\infty} - T_{sat})}{\rho_{liq} T_{sat}}}$ as a function of a normalised pressure difference.

single function cannot capture all physics involved in bubble growth. Some scatter around this single fit exists and bubble growth cannot solely be parameterized by the pressure difference. This is to be expected because not all information that determine \dot{R} in the DG simulations as presented in previous sections are available in the LES. A simple fitted function that captures an average growth rate and provides a qualitative subgrid closure for flash evaporation may, however, be more accurate than existing models that relate the growth to the deviation from equilibrium conditions and typically use data from a single existing experiment (known as Moby Dick experiment [88]) despite different setups, conditions and fluids.

Equations (7.10) and (7.11) allow to derive approximated source terms for a two-equation model with the volume fraction and surface density as model equation. A precondition is that the mean bubble radii and the bubble number can be derived from the volume fraction and surface density within a computational cell. For each cell the bubble radius R^n at time step n and the bubble number N_{bub} must be known. The change in the vapour volume and in the interface area due to bubble growth is then

$$V^{n+1} - V^n = N_{\text{bub}} \frac{4}{3} \pi \left([R^n + \dot{R} \Delta t]^3 - [R^n]^3 \right) \quad (7.12)$$

and

$$A^{n+1} - A^n = N_{\text{bub}} \frac{4}{\pi} \left([R^n + \dot{R} \Delta t]^2 - [R^n]^2 \right), \quad (7.13)$$

respectively. Equations (7.12) and (7.13) can then be incorporated into the source

terms of the Σ - Y model. This is a first attempt to model the growth of multiple bubble as sub-grid scale process for the Σ - and Y -equations. Therefore, the present approximation is subject to the following limitations.

7.3.1 Limitations of the proposed SGS-model

1. The most obvious limitation is the scatter in \dot{R}/A for different parameters. Depending on the conditions Eqs. (7.10) and (7.11) may over- or underpredict the actual growth rates and only a qualitative dependency on Δp^* is obtained.
2. The phase change mechanism at the bubble interface is not explicitly accounted for by the HKR. The heat flux at the interface will also increase if the vapour pressure and therefore the interface temperature is decreased. However, the influence of the boundary layer thickness is not considered. For increasing time the temperature boundary layer increases and the mass flux decreases even if the vapour pressure is low.
3. The present model equation only considers the expansion of bubble clusters but other flow pattern, such as slug flow (see Sec. 2.3), are not accounted for.
4. Most setups for the computation of multiple bubbles use $R_0^* = 50$. This affects the least-square approximation of Eqs. (7.10) and (7.11). Therefore, the coefficients of the present equation may slightly change if larger data sets are available.
5. The numerical simulations last until the outermost bubble is about to break through the outer liquid layer. If this layer becomes too thin, simulations become unstable presumably as a consequence of poorly resolved pressure waves. The validity of the correlations in Eqs. (7.10) and (7.11) cannot be guaranteed if bubble break-up and droplet formation occurs. This is one possible extension for future work. Moreover, a simulation of the entire process from bubble growth to droplet formation can be used to assess time scales for the break-up of the jet from the surface to the center.

CHAPTER 8

Conclusion & Outlook

The present study contains comprehensive investigations of fully compressible numerical simulations of vapour bubble growth in the context of flash boiling of cryogenic oxygen. This final chapter summarises the most important findings and conclusions regarding the DNS of compressible multiphase flows with phase change and the macroscopic simulation of flash boiling. A short summary of the resulting challenges and ideas for future research projects complete this work.

8.1 Conclusion

The first goal of the present investigation was the simulation of single vapour bubble growth with a fully compressible two-phase solver. It is based on the HLLP Riemann solver coupled to a discontinuous Galerkin method and a third order Runge-Kutta scheme to discretise the Navier-Stokes equations in space and time, respectively. The solver preserves a sharp interface between the liquid and vapour. Three different models to estimate the vaporisation mass flux are compared. The first model is the Hertz-Knudsen relation (HKR) which is based on the difference between saturation pressure and vapour pressure. The second approach uses a kinetic relation (KR) according to the original formulation of the HLLP Riemann solver. It estimates the mass flux depending on the deviation of the local entropy to the saturation entropy. The last approach determines the vaporisation mass flux based on a sub-grid scale heat flux and is denoted as sub-grid heat flux model (SHFM). Here, a parabolic temperature profile within the liquid boundary layer is assumed and the temperature gradient is defined by the first derivative at the interface. These models are calibrated to match the bubble radius of a reference solution for a wide pressure, temperature and time range. The

operating conditions are characteristic for superheated cryogenic oxygen issuing into combustion chambers near vacuum.

The HKR and the KR yield similar results. The instantaneous character of the reference mass flux is not captured but the volumetric expansion of bubbles and the total vaporised mass are well predicted. Uncertainties appear only at the smallest time scales. Typical length and time scales vary a lot within the parameter range and the calibrated model coefficients change accordingly. For an increasing temperature the calibration promotes vaporisation but a general dependency on the time scales or pressure ranges is not obvious. The SHFM qualitatively matches the reference solution for the mass flux well. However, the bubble radius and the volumetric expansion match the reference case only during the last part of a simulation. A more sophisticated representation of the model coefficient may improve the results for the volumetric expansion and offers potential for an explicit model without a priori calibration.

The second - and major - objective of the present investigation is the analysis of bubble growth rates in superheated liquid jets. Here, multiple bubbles can interact and single bubble models overpredict the actual growth rates. In this investigation, the HKR determines the vaporisation mass flux and the bubble growth rates are compared to the corresponding results of the single bubble computations. At first the suitability of different geometries to approximate the expansion rates of liquid jets issuing into a vacuum has been evaluated. Each setup resolves multiple vapour bubbles and a low pressure reservoir allows for an expansion of the liquid bulk as a result of bubble growth. The most simplified setup uses a single bubble row which is interpreted as a radial column within a cylindrical jet. In a second and third setup this domain is extended in the circumferential and axial directions, respectively. The number of bubbles in radial direction is also varied. The presence of many vaporising bubbles prevents a sudden and large pressure drop at the jet center and bubbles located away from the jet interface grow very little. A reduced domain size covering approximately 15 bubbles from the jet interface to the jet center suffices to investigate bubble growth. The final setup resolves 15 bubble rows in the radial direction of a cylindrical jet slice. These conditions give an acceptable trade-off between computational cost and accuracy. The growth rates of individual bubbles decrease from the jet surface to its center. When bubbles begin to grow and interact, the liquid is compressed. While the jet surface permanently

faces the low pressure reservoir a pressure gradient from jet surface towards the center develops. The resulting pressure increase is responsible for the deviation of vaporisation rates - and hence bubble growth rates - along the radial direction. For a fixed time step, bubble radii decrease exponentially towards the jet center. The differences to the single bubble results are large and up to 70% in the center of the jet for the time intervals considered. The growth rates of the outermost bubbles differ constantly by approximately 20% from the single bubble simulations. The deviation of the bubble radii to radii from single bubble simulations can be fitted by an exponential function and be parameterized by the distance to the jet surface. An analytical solution for the total volume expansion of a cylindrical jet based on single bubble growth rates is compared with the volumetric expansion of a jet with interacting bubbles, where the corresponding growth rates are obtained from a functional dependence fitted to the DNS data. The final volumes after a minimum growth time needed for bubble merging differ by 66%. These results are similar for a wide range of initial conditions. If the single bubble model is fed with a time variable pressure field the results compare well to those of multiple bubble DNS. It can be concluded that - in the context of macroscopic simulations of flash boiling - the growth process of vapour bubbles needs to be included as a sub-scale model and needs to account for deviations from single bubble growth. In principal, the single bubble reference solution can be solved on-the-fly using the local increased pressure as the back pressure. This requires an additional computation and may increase the total computational effort if numerous bubbles have to be solved independently. Therefore, on the basis of the present DNS an empirical correlation is proposed, which estimates bubble growth rates with respect to the local pressure field. A database for single bubble growth can then be pre-tabulated based on the initial conditions and the derived vaporisation mass fluxes can be adapted with a simple analytical function.

8.2 Outlook

The findings of the present investigation suggest various follow-up studies in both, the field of compressible multi-phase DNS and in the field of LES of flash boiling.

One major restriction of the present work is the need to pre-calibrate the coefficients in the vaporisation models. Here, not only the physical initial conditions are

important but also the relevant time scale. One reason is that the HLLP Riemann solver does not resolve the evaporative cooling. Combined with the HKR or KR, this leads to an almost steady vaporisation process that is in conflict with the highly transient character of single vapour bubble growth. The SHFM improves the qualitative representation of the mass flux. Yet, the model coefficient still requires an a priori calibration for different physical conditions and time ranges. An improvement of the estimation of the boundary layer thickness in the model equation or a dynamic determination of the model coefficient during run time could potentially improve the results and allow for a fully predictive simulation without a priori calibration. Moreover, the HLLP Riemann solver can be extended such that heat diffusion across the interface and evaporative cooling are directly accounted for. This would allow for the omission of any additional model for the vaporisation mass flux and the computations would solely rely on the numerically approximated physics at the interface. However, since boundary layer thicknesses are typically small for the present operating conditions, the computational effort would strongly increase and few bubbles could be resolved only. A third challenge in the computation of compressible bubble growth is the break-up of the liquid layer between the low-pressure chamber and the outermost bubbles. Here, instability occurred whenever the liquid bridge was resolved with less than four FV sub-cells. Underresolved pressure waves in the liquid are identified as a possible reason for the instabilities. A stable simulation of the rupture of the bulk liquid would allow to estimate time scales for the propagation of the jet break-up from the surface to the center.

In the context of the macroscopic simulation of flash boiling enhanced models can be developed on the basis of two-equation models. Here, a volume fraction and a surface density equation are solved allowing to compute average bubble (or droplet) sizes and therefore explicitly distinguish between different flashing regimes. Yet, there is no known study accounting for the bubble expansion within such a two-equation model. The correlations derived in the present work can serve as a basis for the development of sub-scale models to estimate the volume and surface generation by bubble growth. The present correlation would cover the external flashing mode and the internal flashing mode originating from bubbly nozzle flow (see Fig. 2.5). Extended models which also account for slug nozzle flow need to be developed, e.g. using further DNS similar to those of the present study. In other flashing modes, either arising from annular nozzle flow or the fully flashing mode, the expansion of

the jet by vapour bubbles or larger vapour pockets is less important and alternative closure conditions are required.

Appendix A

Derivation of the Hertz-Knudsen relation and the kinetic relation

Hertz-Knudsen relation

If a liquid is in equilibrium with its saturated vapour, the number of molecules per time unit changing from liquid into vapour must be equal to those changing from vapour into liquid [54]. In this case the rate of molecules that transition from a liquid state into a vapour state is known to be the upper limit of vaporisation [44, 54]. The first equation for this limit originates from the work of Hertz [44] and it can be derived assuming a Maxwell-Boltzmann velocity distribution of the vapour molecules at the interface [76, 99]. The mass flux from the interface into the vapour is [99]

$$\dot{m}''_{lv} = \int_{-\infty}^{\infty} \int_{-\infty}^{\infty} \int_0^{\infty} m_{\text{mol}} U f_{\text{vap,sat}} dU dV dW \quad (\text{A.1})$$

with the gas distribution function

$$f_{\text{vap,sat}} = n_{\text{vap,sat}} \frac{\beta_{\text{sat}}^3}{\pi^{3/2}} e^{-\beta_{\text{vap,sat}}^3 ([U-\bar{U}]^2 + [V-\bar{V}]^2 + [W-\bar{W}]^2)}. \quad (\text{A.2})$$

Here, m_{mol} , (U, V, W) and n are the molecule mass, the molecular velocities and the number density of molecules, respectively. Equation (A.2) uses the definition

$$\beta = \sqrt{M/(2\mathcal{R}_g T)} \quad (\text{A.3})$$

with the molar mass M and the specific gas constant \mathcal{R}_g . Inserting Eq. (A.2) in Eq.

(A.1) gives

$$\dot{m}''_{lv} = \rho_{\text{vap,sat}} \left(\frac{\beta_{\text{sat}}^3}{\pi^{3/2}} \right) \left(\frac{1}{2\beta_{\text{sat}}^2} \right) \left(\frac{\pi^{1/2}}{\beta_{\text{sat}}} \right) \left(\frac{\pi^{1/2}}{\beta_{\text{sat}}} \right) \quad (\text{A.4})$$

which is

$$\dot{m}''_{lv} = \rho_{\text{vap,sat}} \left(\frac{\sqrt{\mathcal{R}T_{\text{sat}}}}{\sqrt{2\pi}} \right). \quad (\text{A.5})$$

Applying the ideal gas law $p = \rho\mathcal{R}T$ the mass flow rate from the interface into the gas phase becomes

$$\dot{m}''_{lv} = p_{\text{sat}} \left(\frac{1}{\sqrt{2\pi\mathcal{R}T_{\text{sat}}}} \right). \quad (\text{A.6})$$

Knudsen extended this equation to account for the deviation from the theoretical maximum [54, 55]. He introduced the calibration coefficient λ_{vap} yielding [55]

$$\dot{m}''_{lv} = p_{\text{sat}} \left(\frac{\lambda_{\text{vap}}}{\sqrt{2\pi\mathcal{R}T_{\text{sat}}}} \right) \quad (\text{A.7})$$

with $\lambda_{\text{vap}} \leq 1$. Equation (A.7) is valid only if the liquid vaporises into pure vacuum [31]. In a realistic case the vapour propagating away from the interface will generate a back pressure p_{vap} . Therefore, the Hertz-Knudsen relation combines the mass flux from the interface into the vapour \dot{m}''_{lv} with the corresponding flux from the vapour to the interface [31, 76]:

$$\dot{m}'' = \frac{1}{\sqrt{2\pi\mathcal{R}}} \left(\lambda_{\text{vap}} \frac{p_{\text{sat}}}{\sqrt{T_{\text{liq}}}} - \lambda_{\text{cond}} \frac{p_{\text{vap}}}{\sqrt{T_{\text{vap}}}} \right). \quad (\text{A.8})$$

The kinetic relation

The derivation of the kinetic relation follows the work of Fechter et. al [35]. It is based on an entropy balance at the interface where the entropy production is defined by

$$\eta = \left[\dot{m}''(s_{\text{vap}} - s_{\text{liq}}) + \left(\frac{q_{\text{vap}}}{T_{\text{vap}}} - \frac{q_{\text{liq}}}{T_{\text{liq}}} \right) \right]. \quad (\text{A.9})$$

Assuming that η is zero the difference between the heat fluxes is approximated by

$$q_{\text{vap}} - q_{\text{liq}} \approx -\dot{m}''T_{\text{ref}}(s_{\text{vap,sat}} - s_{\text{liq,sat}}). \quad (\text{A.10})$$

With $T_{\text{liq}} \approx T_{\text{vap}} = T_{\text{ref}}$ the combination of Eqs. (A.9) and (A.10) gives

$$\eta = \dot{m}'' [(s_{\text{vap}} - s_{\text{liq}}) - (s_{\text{vap,sat}} - s_{\text{liq,sat}})]. \quad (\text{A.11})$$

Fechter et al. use the constitutive law [35] $\eta T_{\text{ref}} = c_{\text{ent}} \dot{m}''$ to derive the final model equation

$$\dot{m}'' = \frac{1}{c_{\text{ent}}} T_{\text{ref}} [s - s_{\text{sat}}]. \quad (\text{A.12})$$

The model coefficient c_{ent} needs to be adapted for different fluids or process conditions.

Appendix B

Analytical equations for the HLLP Riemann solver

The approximated intermediate states in the HLLP Riemann solver are determined by the following expressions given by Fechter et al. [36]:

Left star state $\mathbf{v}_L^* = (\rho_L^*, v_L^*, e_L^*, p_L^*)^T$:

$$\begin{aligned} \rho_L^* = & (2S_L\rho_L^2v_L + \rho_Lv_L\rho_Rv_R - S_{\text{int}}\rho_Lv_L + S_{\text{int}}\rho_Rv_R - S_L^2\rho_L^2 \\ & + S_L\rho_L S_R\rho_R + S_{\text{int}}S_L\rho_L - S_{\text{int}}S_R\rho_R - \rho_Lv_L S_R\rho_R - \rho_L^2v_L^2 \\ & - S_L\rho_L\rho_Rv_R)/(-\rho_Lv_L^2 + \rho_Rv_R^2 - \rho_L S_L^2 + S_{\text{int}}S_L - S_{\text{int}}S_R - S_R\rho_Rv_R \\ & + 2S_L\rho_Lv_L + p_R - p_L - \Delta p - S_L\rho_Rv_R + S_L S_R\rho_R) \end{aligned} \quad (\text{B.1})$$

$$\begin{aligned} v_L^* = & (-S_R\rho_Rv_R\rho_Lv_L + S_R\rho_Rv_R S_L\rho_L + p_L S_L\rho_L + \Delta p S_L\rho_L + 2\rho_L^2v_L^2 S_L \\ & - \rho_Lv_L S_{\text{int}}S_R + S_{\text{int}}S_L\rho_Rv_R + S_L\rho_L S_{\text{int}}S_R - p_L\rho_Lv_L - S_L^2\rho_L^2v_L \\ & + \rho_Lv_L\rho_Rv_R^2 - \rho_L^2v_L^3 - S_L\rho_L\rho_Rv_R^2 - \rho_Lv_L\Delta p + \rho_Lv_L p_R - S_L\rho_L p_R \\ & - S_L S_R\rho_R S_{\text{int}})/(2S_L\rho_L^2v_L + \rho_Lv_L\rho_Rv_R - S_{\text{int}}\rho_Lv_L + S_{\text{int}}\rho_Rv_R \\ & - S_L^2\rho_L^2 + S_L\rho_L S_R\rho_R + S_{\text{int}}S_L\rho_L - S_{\text{int}}S_R\rho_R - \rho_Lv_L S_R\rho_R \\ & - \rho_L^2v_L^2 - S_L\rho_L\rho_Rv_R) \end{aligned} \quad (\text{B.2})$$

$$p_L^* = p_L + (\rho_Lv_L^2 - \rho_L^*(v_L^*)^2) - S_L(\rho_Lv_L - \rho_L^*v_L^*) \quad (\text{B.3})$$

$$e_L^* = \frac{1}{\rho_L^*(v_L^* - S_L)}(-S_L\rho_L e_L + v_L(\rho_L e_L + p_L) - v_L^* p_L^*) - \frac{1}{2}(v_L^*)^2 \quad (\text{B.4})$$

Right star state $\mathbf{v}_R^* = (\rho_R^*, u_R^*, e_R^*, p_R^*)^T$:

$$\begin{aligned} \rho_R^* = & (\rho_L v_L S_R \rho_R - S_{\text{int}} \rho_L v_L - \rho_L v_L \rho_R v_R - S_L \rho_L S_R \rho_R + S_{\text{int}} S_L \rho_L \\ & + S_L \rho_L \rho_R v_R - 2S_R \rho_R^2 v_R + S_R^2 \rho_R^2 - S_{\text{int}} S_R \rho_R + S_{\text{int}} \rho_R v_R + \rho_R^2 v_R^2) / \\ & (-\rho_L v_L^2 + S_L \rho_L v_L + \rho_L v_L S_R - \rho_L S_L S_R + S_R^2 \rho_R - 2S_R \rho_R v_R - p_L + \rho_R v_R^2 \\ & - \Delta p + S_{\text{int}} S_L - S_{\text{int}} S_R + p_R) \end{aligned} \quad (\text{B.5})$$

$$\begin{aligned} v_R^* = & (S_R^2 \rho_R^2 v_R - \rho_L v_L S_{\text{int}} S_R + S_{\text{int}} S_L \rho_R v_R + S_L \rho_L S_{\text{int}} S_R - 2\rho_R^2 v_R^2 S_R \\ & - p_R S_R \rho_R + p_R \rho_R v_R - S_L S_R \rho_R S_{\text{int}} - \rho_L v_L^2 \rho_R v_R + \rho_R^2 v_R^3 + S_L \rho_L v_L \rho_R v_R \\ & - S_L \rho_L v_L S_R \rho_R + \Delta p S_R \rho_R + p_L S_R \rho_R - p_L \rho_R v_R - \Delta p \rho_R v_R + \rho_L v_L^2 S_R \rho_R) / \\ & (\rho_L v_L S_R \rho_R - S_{\text{int}} \rho_L v_L - \rho_L v_L \rho_R v_R - S_L \rho_L S_R \rho_R + S_{\text{int}} S_L \rho_L \\ & + S_L \rho_L \rho_R v_R - 2S_R \rho_R^2 v_R + S_R^2 \rho_R^2 - S_{\text{int}} S_R \rho_R + S_{\text{int}} \rho_R v_R + \rho_R^2 v_R^2) \end{aligned} \quad (\text{B.6})$$

$$p_R^* = p_R + (\rho_R v_R^2 - \rho_R^* (v_R^*)^2) - S_R (\rho_R v_R - \rho_R^* v_R^*) \quad (\text{B.7})$$

$$\begin{aligned} e_R^* = & \frac{1}{\rho_R^* (v_R^* - S_{\text{int}})} (\Delta p S_{\text{int}} - S_{\text{int}} \rho_L^* e_L^* - v_R^* p_R^* + v_L^* (\rho_L^* e_L^* + p_L^* \\ & - \rho_L^* (S_{\text{int}} - v_L^*) \Delta h_{\text{lat}}) - \frac{1}{2} (v_R^*)^2) \end{aligned} \quad (\text{B.8})$$

Appendix C

Derivation of the Rayleigh-Plesset equation

The following derivation follows the derivation in [14]. Initially an arbitrary function $F(t) = u(r, t) \cdot r^2$ is considered, where u , r and t are velocity, radius and time respectively. Without any mass transfer at the liquid-vapour interface, the velocity at the interface with the bubble radius R is

$$u(R, t) = \frac{dR}{dt} = \frac{F(t)}{R^2}, \quad (\text{C.1})$$

which gives

$$F(t) = R^2 \frac{dR}{dt}. \quad (\text{C.2})$$

In case vaporisation takes place, the vaporisation rate \dot{m}_v can be estimated as

$$\dot{m}_v = \rho_v \dot{V} = \rho_v \frac{d}{dt} \left(\frac{4}{3} \pi R^3 \right) = \rho_v 4\pi R^2 \frac{dR}{dt}, \quad (\text{C.3})$$

with ρ_v and \dot{V} being the vapour density and volume flow rate, respectively. Considering the liquid side, the mass flow rate due to vaporisation is

$$\dot{m}_l = \rho_l A u_l \quad (\text{C.4})$$

where A and u_l are the surface of the bubble and the relative speed between bubble wall and liquid (the speed at which the interface moves due to the vaporised “vanished” liquid volume). Setting both mass flow rates equal gives for the relative

velocity

$$u_l = \frac{\rho_v}{\rho_l} \frac{dR}{dt} \quad (\text{C.5})$$

and the flow velocity at the bubble wall is then

$$u(R, t) = \frac{dR}{dt} - u_l = \left(1 - \frac{\rho_v}{\rho_l}\right) \frac{dR}{dt}. \quad (\text{C.6})$$

If the density ratio between gas phase and liquid phase is high, the contribution of u_l can be neglected. With the initially defined auxiliary function $F(t)$ the radially defined velocity field is

$$u(r, t) = \frac{R^2}{r^2} \frac{dR}{dt}. \quad (\text{C.7})$$

The momentum balance in the liquid in spherical coordinates reads

$$\rho_l \left(\frac{\partial u}{\partial t} + u \frac{\partial u}{\partial r} \right) = -\frac{\partial p}{\partial r} + \mu_l \left(\frac{1}{r^2} \frac{\partial}{\partial r} \left[r^2 \frac{\partial u}{\partial r} \right] - \frac{2u}{r^2} \right). \quad (\text{C.8})$$

Dividing the whole equation by ρ_l and inserting Eq. (C.7) in Eq. (C.8) gives

$$\begin{aligned} & \frac{\partial}{\partial t} \left(\frac{R^2}{r^2} \frac{dR}{dt} \right) + \frac{R^2}{r^2} \frac{dR}{dt} \frac{\partial}{\partial r} \left(\frac{R^2}{r^2} \frac{dR}{dt} \right) - \\ & \nu_l \left(\frac{1}{r^2} \frac{\partial}{\partial r} \left[r^2 \frac{\partial}{\partial r} \left\{ \frac{R^2}{r^2} \frac{dR}{dt} \right\} \right] - \frac{2R^2}{r^4} \frac{dR}{dt} \right) = -\frac{1}{\rho_l} \frac{\partial p}{\partial r} \end{aligned} \quad (\text{C.9})$$

Further analysis considering product rule, chain rule etc., the previous equation can be summarized to

$$\frac{1}{r^2} \left(2R \left[\frac{dR}{dt} \right]^2 + R^2 \frac{d^2 R}{dt^2} \right) - \frac{2R^4}{r^5} \left(\frac{dR}{dt} \right)^2 = -\frac{1}{\rho_l} \frac{\partial p}{\partial r}. \quad (\text{C.10})$$

An integration from $r = R$ to $r = \infty$ defined as

$$\int_{r=R}^{\infty} \left\{ \frac{1}{r^2} \left(2R \left[\frac{dR}{dt} \right]^2 + R^2 \frac{d^2 R}{dt^2} \right) - \frac{2R^4}{r^5} \left(\frac{dR}{dt} \right)^2 \right\} dr = -\frac{1}{\rho_l} \int_{p(R)}^{p(\infty)} dp. \quad (\text{C.11})$$

then gives

$$\left[-\frac{1}{r} \left(2R \left(\frac{dR}{dt} \right)^2 + R^2 \frac{d^2R}{dt^2} \right) + \frac{2R^4}{4r^4} \left(\frac{dR}{dt} \right)^2 \right]_R^\infty = \frac{p(R) - p(\infty)}{\rho_l}. \quad (\text{C.12})$$

Inserting the limits of the integral we get

$$0 - \left[-\frac{1}{R} \left(2R \left(\frac{dR}{dt} \right)^2 + R^2 \frac{d^2R}{dt^2} \right) + \frac{2R^4}{4R^4} \left(\frac{dR}{dt} \right)^2 \right] = \frac{p(R) - p(\infty)}{\rho_l}. \quad (\text{C.13})$$

If the velocity is defined as $\dot{R} = dR/dt$ and the acceleration as $\ddot{R} = d^2R/dt^2$ the Rayleigh equation is obtained:

$$\frac{3}{2} \dot{R}^2 + R\ddot{R} = \frac{p(R) - p(\infty)}{\rho_l}. \quad (\text{C.14})$$

It has to be noted here that the viscous terms cancel out during analysis. Frictional effects as well as the contribution of the surface tension are taken into account via the boundary condition at the interface:

$$p(R) = p_b - \frac{2\sigma}{R} - \frac{4\mu}{R} \dot{R} \quad (\text{C.15})$$

where p_b is the pressure inside the bubble which finally leads to the Rayleigh-Plesset equation:

$$R\ddot{R} + \frac{3}{2} \dot{R}^2 = \frac{1}{\rho_l} \left(p_b - p(\infty) - \frac{2\sigma}{R} - \frac{4\mu}{R} \dot{R} \right) \quad (\text{C.16})$$

Appendix D

Coefficients of the different vaporisation models

This section lists the calibrated coefficients for the HKR, the KR and the SHFM for each combination of T_0 , R_p and R_0^* . If no value is given, no stable solution was obtained.

Table 4.1: λ_{vap} for $R_p = 5$ and $R_p = 10$.

R_0^*	C5- 90	C5- 100	C5- 110	C5- 120	C10- 90	C10- 100	C10- 110	C10- 120
1	0.050	0.071	0.093	0.110	0.045	0.064	0.084	0.093
5	0.056	0.071	0.084	0.093	0.052	0.065	0.080	0.083
10	0.056	0.064	0.075	0.083	0.055	0.065	0.076	0.082
25	0.042	0.045	0.050	0.057	0.047	0.052	0.058	0.063
50	0.030	0.031	0.033	0.038	0.035	0.037	0.042	0.046

Table 4.2: λ_{vap} for $R_p = 50$ and $R_p = 100$.

R_0^*	C50- 90	C50- 100	C50- 110	C50- 120	C100- 90	C100- 100	C100- 110	C100- 120
1	-	0.058	0.075	0.082	-	-	0.073	0.081
5	0.053	0.064	0.072	0.074	0.052	0.058	0.071	0.073
10	0.054	0.065	0.074	0.076	0.054	0.059	0.073	0.075
25	0.050	0.055	0.059	0.064	0.051	0.054	0.060	0.064
50	0.039	0.041	0.045	0.049	0.039	0.041	0.045	0.049

Table 4.3: c_{ent} for $R_p = 5$ and $R_p = 10$.

R_0^*	C5- 90	C5- 100	C5- 110	C5- 120	C10- 90	C10- 100	C10- 110	C10- 120
1	3793	907.0	278.2	119.2	4279	1012	333.7	139.3
5	4448	1115	425.0	193.1	4844	1340	476.1	231.9
10	4529	1251	495.7	224.8	4796	1375	503.6	256.3
25	5612	1886	747.0	350.8	5807	1881	724.5	340.5
50	8186	2747	1207	554.0	8152	2555	1085.5	507.3

Table 4.4: c_{ent} for $R_p = 50$ and $R_p = 100$.

R_0^*	C50- 90	C50- 100	C50- 110	C50- 120	C100- 90	C100- 100	C100- 110	C100- 120
1	-	-	375.0	-	-	-	386.4	-
5	5262	1481	555.8	296.5	5370	1659	562.7	303.3
10	5193	1468	576.0	288.3	5160	1639	585.2	294.9
25	5684	1826	721.4	368.9	5628	1884	768.7	372.2
50	7667	2603	1032.6	524.9	7685	2612	1036.0	531.1

Table 4.5: C_δ for $R_p = 5$ and $R_p = 10$.

R_0^*	C5- 90	C5- 100	C5- 110	C5- 120	C10- 90	C10- 100	C10- 110	C10- 120
1	0.993	1.074	1.288	1.826	1.367	1.495	1.774	2.620
5	0.175	0.221	0.305	0.437	0.218	0.281	0.400	0.607
10	0.088	0.121	0.174	0.248	0.103	0.141	0.208	0.307
25	0.050	0.074	0.102	0.139	0.052	0.081	0.113	0.162
50	0.037	0.055	0.076	0.103	0.039	0.057	0.080	0.113

Table 4.6: C_δ for $R_p = 50$ and $R_p = 100$.

R_0^*	C50- 90	C50- 100	C50- 110	C50- 120	C100- 90	C100- 100	C100- 110	C100- 120
1	1.750	1.942	2.367	3.524	1.801	2.336	2.454	3.640
5	0.289	0.374	0.514	0.810	0.299	0.419	0.525	0.845
10	0.130	0.178	0.246	0.389	0.130	0.190	0.255	0.397
25	0.062	0.089	0.127	0.190	0.062	0.092	0.128	0.193
50	0.041	0.061	0.087	0.129	0.042	0.062	0.088	0.132

Appendix E

Dependency of c_{ent} and C_δ on initial conditions and characteristic numbers

Figure 5.1 depicts the dependencies of the coefficient c_{ent} in the KR on R_0^* , R_p , T_0 , Ja , R^+ and t^+ . Equation (3.21) shows that the mass flux scales inversely proportional to c_{ent} . Subsequently, the individual subfigures of Fig. 5.1 are discussed:

- *Subfig. E.1(a)*: With increasing R_0^* the model coefficient increases such that the asymptotic mass flux decreases. As discussed in Sec. 6.2 this results from the transient decrease of the reference mass flux with time/radius.
- *Subfig. E.1(b)*: The model coefficient depends only weakly on the superheat ratio R_p . Again, the trends and conclusions are similar to those of the HKR in Sec. 6.2 considering the inverse proportionality of the mass flux on c_{ent} .
- *Subfig. E.1(c)*: We observe a decrease of the coefficient with increasing temperature if R_0^* and R_p are fixed. As observed for the HKR, the model coefficient scales such that vaporisation is enhanced for an increase in temperature. However, the entropy as the key quantity in Eq. (3.21) also changes with T_0 and a direct correlation is not apparent.

Figure 5.2 shows the resulting correlations for the SHFM. In general, an increase in C_δ yields a decrease in the mass flux. However, the SHFM yields a similar transient behaviour as the reference solution and the correlations of C_δ in Fig. 5.2 deviate from those obtained for the HKR and the KR, respectively. This is a consequence

of the R -dependency of the mass flux given by Eqs. (3.22), (3.23) and (3.24). Subsequently, the individual dependencies of C_δ are discussed

- *Subfig. E.2(a)*: Eqs. (3.23) and (3.24) show that the mass flux decreases with increasing R_0^* . The high coefficients observed in Fig. E.2(a) at small R_0^* avoid an overprediction of the mass flux when the radii and approximated boundary layer thicknesses are rather small.
- *Subfigs. E.2(b) and E.2(c)*: The trends $C_\delta = f(R_p)$ and $C_\delta = f(T_0)$ are explained by the same physical effects. Figures E.2(b) and E.2(c) show that C_δ increases with R_p and T_0 , respectively. This particularly applies for small R_0^* (solid lines). Both, for increasing T_0 and increasing R_p , the temperature difference $\Delta T = T_{\text{liq}} - T_{\text{sat}}(p_\infty)$ increases. According to Fig. 6.3 the pressure in the bubble rapidly approaches the ambient pressure such that $\Delta T = T_{\text{liq}} - T_{\text{sat}}(p_\infty)$ reasonably approximates the temperature difference in Eq. (3.23). Thus, an increase in T_0 and R_p would result in an increase of \dot{m}'' . At the same time, the bubble radius and accordingly the boundary layer estimation decrease with increasing T_0 and R_p which, again, allows for higher mass fluxes. The increase of C_δ avoids nonphysically high mass fluxes.

Both, the KR and the SHFM do not reveal a clear correlation between the coefficients and the characteristic parameters R^+ , t^+ and Ja .

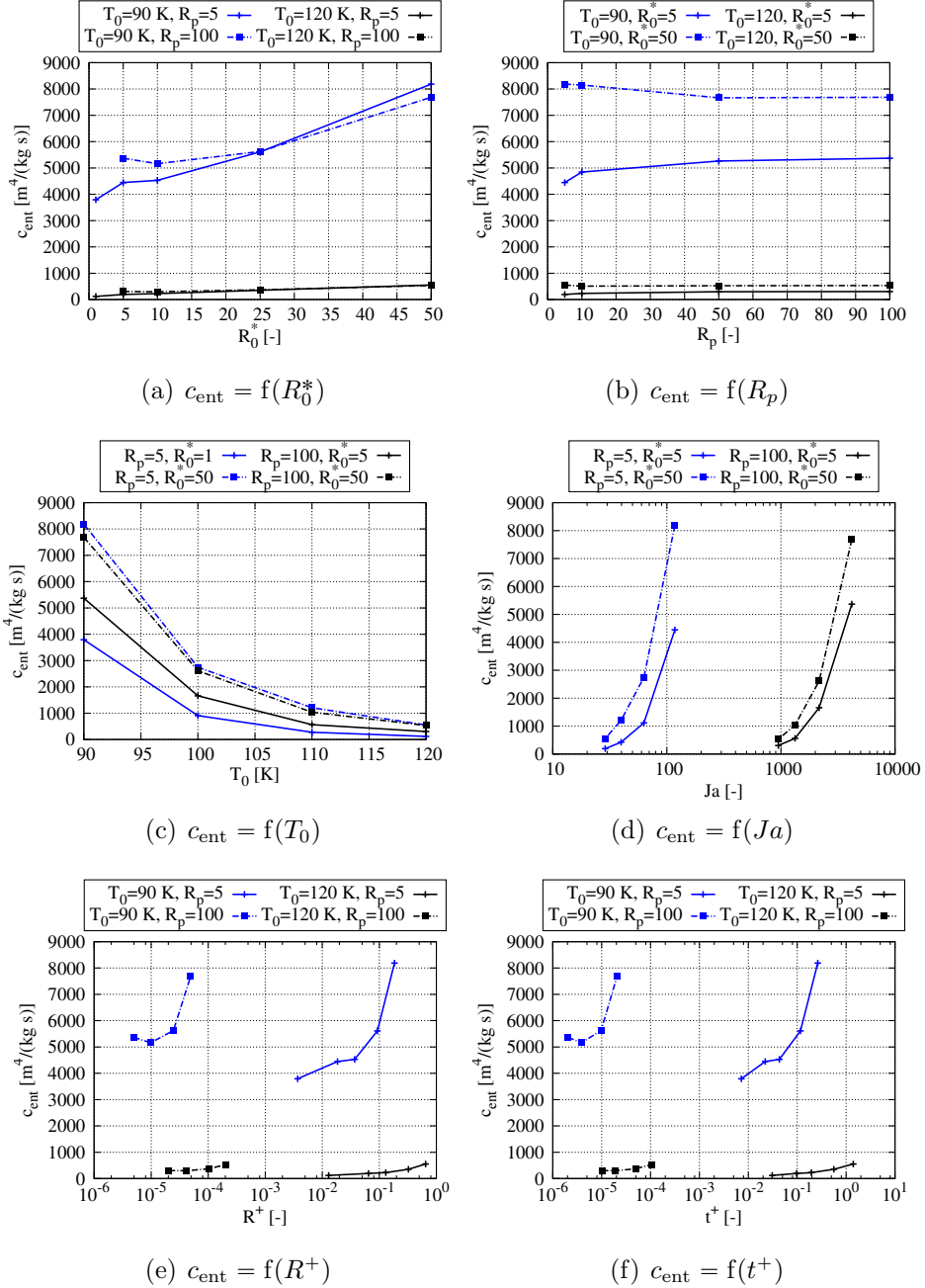


Figure 5.1: Vapourisation coefficients c_{ent} as a function of different characteristic quantities of our investigation.

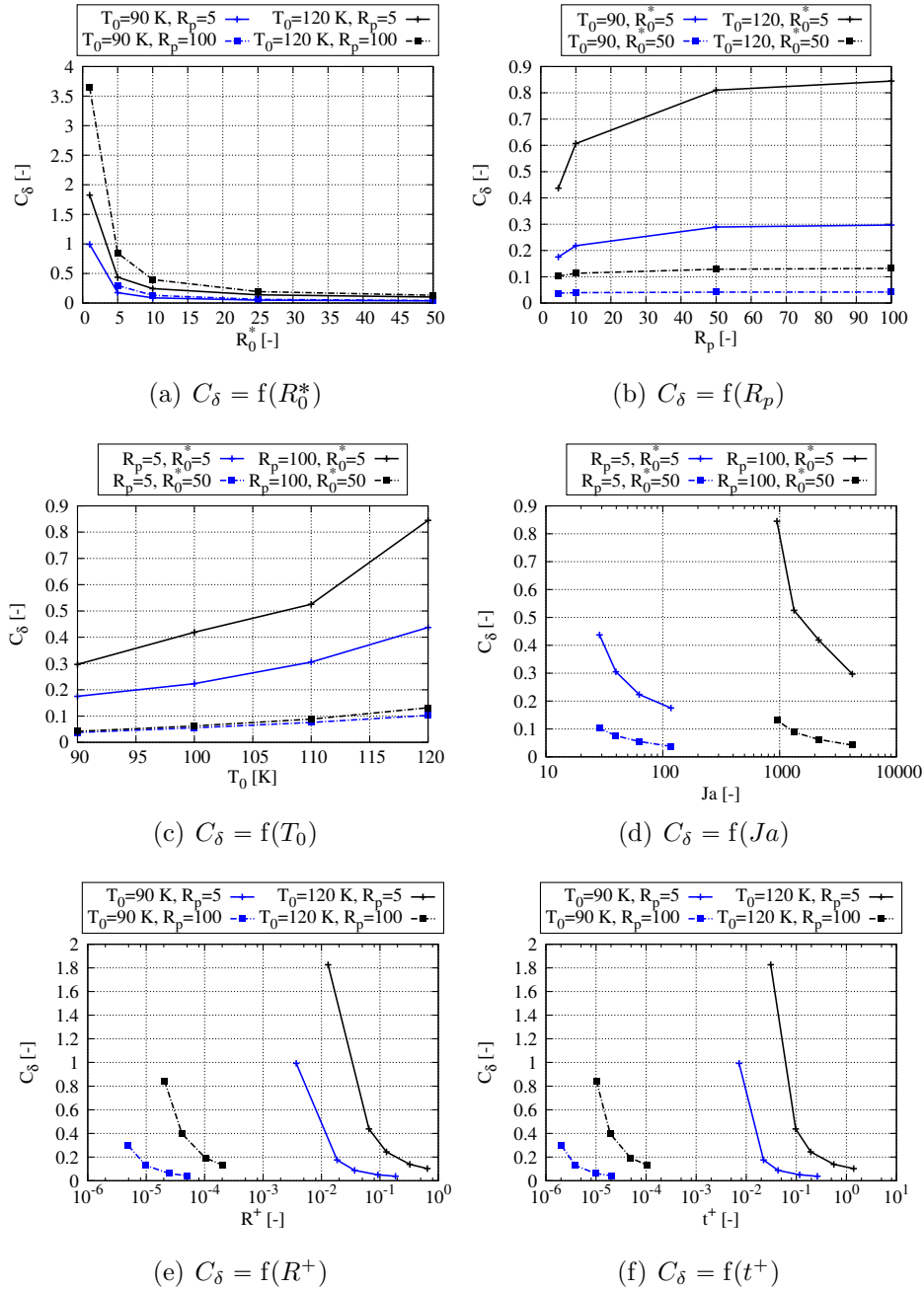


Figure 5.2: Vaporisation coefficients C_δ as a function of different characteristic quantities of our investigation.

Appendix F

Derivation of the expansion equation for cylindrical volumes containing spherical bubbles.

The present analysis uses the following assumptions and definitions:

- The dimensionless distance of the bubbles is

$$\Psi_{\text{bub}} = \frac{D_{\text{bub}}}{R_0}. \quad (\text{F.1})$$

- The bubbles are distributed in a close-packing of spheres.
- The cylindrical volume is defined by the cylinder radius R_{noz} and its length L_{jet} .
- The ratio between vapour density and liquid density is

$$\rho^* = \frac{\rho_{\text{bub}}}{\rho_{\text{liq}}}. \quad (\text{F.2})$$

- The ratio between final jet volume and initial jet volume is

$$V^* = \frac{V_{\text{end,jet}}}{V_{0,\text{jet}}}. \quad (\text{F.3})$$

One-fourth of the cylindrical jet with the initial volume

$$V_{0,\text{jet}} = 0.25\pi R_{\text{noz}}^2 L_{\text{jet}} \quad (\text{F.4})$$

is considered. The number of resolved bubbles in the three-dimensional domain is the product of bubble numbers in the x -, y - and z -direction. As we consider a cylindrical geometry in the x - y -plane the product of the bubble numbers in these directions is scaled with $\pi/4$. We consider the densest possible package of spheres following the bubble distances from Eq. (7.1). The resulting number of bubbles is

$$N_B = \frac{L_{\text{jet}}}{D_{\text{bub}}} \left(\frac{R_{\text{noz}}}{D_{\text{bub}}} \right)^2 \sqrt{2} \frac{3}{\sqrt{6}} \frac{\pi}{4} \quad (\text{F.5})$$

The generated vapour volume is equal to the product of number of bubbles and the volume increase of a single bubble,

$$\Delta V_{\text{vap}} = N_B \frac{4}{3} \pi ([R^* \cdot R_{\text{crit}}]^3 - R_{\text{crit}}^3) = N_B \frac{4}{3} \pi R_{\text{crit}}^3 (R^{*3} - 1). \quad (\text{F.6})$$

Combining Eqs. (F.1),(F.5) and (F.6) with $R_0 = R_{\text{crit}}$ gives

$$\Delta V_{\text{vap}} = \sqrt{3} \frac{\pi^2}{3} L_{\text{jet}} R_{\text{noz}}^2 \frac{1}{\Psi_{\text{bub}}^3} (R^{*3} - 1). \quad (\text{F.7})$$

The liquid volume, which is evaporated is

$$\Delta V_{\text{liq}} = \Delta V_{\text{vap}} \cdot \rho^* \quad (\text{F.8})$$

The final volume of the liquid jet is

$$V_{\text{end,jet}} = V_{0,\text{jet}} + \Delta V_{\text{vap}} - \Delta V_{\text{liq}} = V_{0,\text{jet}} + \Delta V_{\text{vap}}(1 - \rho^*) \quad (\text{F.9})$$

Using Eqs. (F.4) and (F.9) the volume ratio of the final and initial jet is derived as

$$\begin{aligned} V^* &= \frac{V_{\text{jet,end}}}{V_{\text{jet,0}}} = 1 + \frac{\Delta V_{\text{vap}}(1 - \rho^*)}{V_{\text{jet,0}}} \\ &= 1 + \sqrt{3} \frac{(\pi^2/3) L_{\text{jet}} R_{\text{noz}}^2 \frac{1}{\Psi_{\text{bub}}^3} (R^{*3} - 1)(1 - \rho^*)}{0.25 \pi L_{\text{jet}} R_{\text{noz}}^2} \\ &= 1 + \sqrt{3} \frac{\pi}{0.75} \frac{1}{\Psi_{\text{bub}}^3} (R^{*3} - 1)(1 - \rho^*). \end{aligned} \quad (\text{F.10})$$

Appendix G

Data storage

Table 7.1: Case and code used to produce results of paper on single bubble growth by Dietzel et al. [27]. The main directory on the data storage is `ITV-PUBLICATIONS/GIT/2019_Dietzel_IJMF/Rayleigh-Plesset-Data`. The corresponding code repository is `GITLAB/itv-mitarbeiter/Dietzel/rayleigh-plesset`

2019-Dietzel-IJMF-DNS-SB		
Data on storage	Case	Code
heat-diffusion	Single bubble growth using algorithm of Lee&Merte [62] for various R_p and T_0 .	"master" on GIT SHA: c713b48d
no-heat-diffusion	Single bubble growth using algorithm of Lee&Merte [62] for various R_p and T_0 neglecting heat-diffusion and evaporative cooling cooling	"no_heat-diffusion" on GIT SHA: 6c59c6ca

Table 7.2: Case and code used to produce results of paper on single bubble growth by Dietzel et al. [27]. The main directory on the data storage is ITV-PUBLICATIONS/GIT/2019_Dietzel_IJMF/DG-Data. The corresponding code repository is GITLAB/TwoPhaseDG/StruktiTwoPhase

2019-Dietzel-IJMF-DNS-SB		
Data on storage	Case	Code
HKR_DEFAULT	Various R_p , T_0 and R_0^* ; HLLP solver [36]; HKR, default setup	"master" on GIT SHA: 596ab101
HKR_CFL	Various R_p , T_0 and R_0^* ; HLLP solver [36]; HKR, decreased CFL number	"master" on GIT SHA: 596ab101
HKR_MESH	Various R_p , T_0 and R_0^* ; HLLP solver [36]; HKR, mesh study	"master" on GIT SHA: 596ab101
HKR_PRESS	Various R_p , T_0 and R_0^* ; HLLP solver [36]; HKR, study initial bub. pres.	"master" on GIT SHA: 596ab101
KR	Various R_p , T_0 and R_0^* ; HLLP solver [36]; KR	"master" on GIT SHA: 596ab101
SHFM	Various R_p , T_0 and R_0^* ; HLLP solver [36]; SHFM	"master" on GIT SHA: 596ab101

Table 7.3: Case and code used to produce results of paper on single bubble growth by Dietzel et al. [27]. The main directory on the data storage is ITV-PUBLICATIONS/GIT/2019_Dietzel_IJMF/DG-Data. The corresponding code repository is GITLAB/TwoPhaseDG/ILASS17Flexi

2019-Dietzel-IJMF-DNS-SB		
Data on storage	Case	Code
HKR_3D_Rp-5_T0-120	Fully 3D simulation using the reference conditions	"master" on GIT SHA: 71fff548

Table 7.4: The following codes are generally used for pre- and postprocessing of the 3D simulations

Pre- and post processing for the 3D simulations		
GITLAB repo	Usage	Code
GITLAB/TwoPhaseDG/EOS	Generation of EOS tables Read-in of table	"master" on GIT SHA: 33d0462a
GITLAB/TwoPhaseDG/HOPR	Mesh generation	"master" on GIT SHA: a08deca9
GITLAB/TwoPhaseDG/Posti	Post processing tool, i.a. generation of paraview files (*.vtu)	"master" on GIT SHA: 88afd1ac
GITLAB/TwoPhaseDG/ Eval_Bubble_Growth	Post processing tool, i.a. for evaluation of growth rates and filtered quantities	"master" on GIT SHA: 95612315

Table 7.5: Case and code used to produce results of paper on multiple bubble growth. Here, cases of the bubble column are considered. The main directory on the data storage is ITV-PUBLICATIONS/GIT/2019_Dietzel_IJMF-2/DG-Data/bubble_column. The corresponding code repository is GITLAB/TwoPhaseDG/ILASS17Flexi

2019-Dietzel-IJMF-DNS-MB		
Data on storage	Case	Code
Rp-5_T0-120_R0STAR-50/ Nx Bub-05	Five fully resolved bubbles, Sec. 5.1 in paper	"master" on GIT SHA: 71fff548
Rp-5_T0-120_R0STAR-50/ Nx Bub-10	Ten fully resolved bubbles, Sec. 5.2 in paper	"master" on GIT SHA: 71fff548
Rp-5_T0-120_R0STAR-50/ Nx Bub-15	15 fully resolved bubbles, Sec. 5.2 in paper	"master" on GIT SHA: 71fff548
Rp-5_T0-120_R0STAR-50/ Nx Bub-20	20 fully resolved bubbles, Sec. 5.2 in paper	"master" on GIT SHA: 71fff548

Table 7.6: Case and code used to produce results of paper on multiple bubble growth. Here, cases of the jet slice are considered. The main directory on the data storage is `ITV-PUBLICATIONS/GIT/2019_Dietzel_IJMF-2/DG-Data/jet_slice`. The corresponding code repository is `GITLAB/TwoPhaseDG/ILASS17Flexi`

2019-Dietzel-IJMF-DNS-MB		
Data on storage	Case	Code
Rp-5_T0-120_R0STAR-50/ NxBub-05	Five fully resolved bubbles, in radial direction Sec. 5.2 in paper	"master" on GIT SHA: 71fff548
Rp-5_T0-120_R0STAR-50/ NxBub-15	15 fully resolved bubbles, in radial direction, reference conditions Sec. 5.3 in paper	"master" on GIT SHA: 71fff548
Rp-*_T0-*_R0STAR-*/*	Parameter study on R_p , T_0 and R_0^* , Sec. 5.4 in paper	"master" on GIT SHA: 71fff548
Rp-*_T0-*_R0STAR-* _SHFM/*	Corresponding parameter, study with SHFM, Sec. 5.5 in paper	"master" on GIT SHA: 71fff548

Bibliography

- [1] UCS satellite database. <https://www.ucsusa.org/nuclear-weapons/space-weapons/satellite-database#.W-BbMBRRdoA>, August 2018. Accessed: 2018-11-05.
- [2] UCS satellite database: Database (excel format). https://s3.amazonaws.com/ucs-documents/nuclear-weapons/sat-database/8-10-18-update/UCS_Satellite_Database_5-1-2018.xlsx, August 2018. Accessed: 2018-11-05.
- [3] B. Abramzon and W. Sirignano. Droplet vaporization model for spray combustion calculation. *International Journal of Heat and Mass Transfer*, 32:1605–1618, 1989.
- [4] D. Adalsteinsson and J.A.Sethian. The fast construction of extension velocities in level set methods. *Journal of Computational Physics*, 148:2–22, 1999.
- [5] T.D. Aslam. A partial differential equation approach to multidimensional extrapolation. *Journal of Computational Physics*, 193:349–355, 2003.
- [6] A.A. Avdeev and Y.B. Zudin. Inertial-thermal governed vapor bubble growth in highly superheated liquid. *Heat and Mass Transfer*, 41:855–863, 2005.
- [7] H.D. Baehr and S. Kabelac. *Thermodynamik*. Springer-Vieweg, 2016.
- [8] T. Bar-Kohany and M. Levy. State-of-the-art review of flash-boiling atomization. *Atomization and Sprays*, 26(12):1259–1305, 2016.
- [9] F. Bassi and S. Rebay. A high-order accurate discontinuous finite element method for the numerical solution of the compressible Navier-Stokes equations. *Journal of Computational Physics*, 131(2):267–279, 1997.

- [10] F. Bassi, S. Rebay, G. Mariotti, S. Pedinotti, and M. Savini. A high-order accurate discontinuous finite element method for inviscid and viscous turbomachinery flows. In R. Decuyper and G. Dibelius, editors, *Proceedings of the 2nd European Conference on Turbomachinery, Fluid Dynamics and Thermodynamics*, pages 99–108. Antwerpen, Belgium, 1997.
- [11] I.H. Bell, J. Wronski, S. Quoilin, and V. Lemort. Pure and pseudo-pure fluid thermophysical property evaluation and the open-source thermophysical property library CoolProp. *Industrial & Engineering Chemistry Research*, 53:2498–2508, 2014.
- [12] Z. Bilicki and J. Kestin. Physical aspects of the relaxation model in two-phase flow. *Proceedings of the Royal Society of London A*, 428:379–397, 1990.
- [13] M. Blander and J.L. Katz. Bubble nucleation in liquids. *A.I.Ch.E. Journal*, 21(5):833–848, 1975.
- [14] C.E. Brennen. *Cavitation and bubble dynamics*. Oxford University Press, 1995.
- [15] R. Brown and J.L. York. Sprays formed by flashing liquid jets. *A.I.Ch.E. Journal*, 8:149–153, 1962.
- [16] V.P. Carey. *Liquid-vapor phase-change phenomena*. Hemisphere, 1992.
- [17] C.-H. Chang, X. Deng, and T.G. Theofanous. Direct numerical simulation of interfacial instabilities: A consistent, conservative, all-speed, sharp interface method. *Journal of Computational Physics*, 242:946–990, 2013.
- [18] J. Chesnel, J. Réveillon, T. Ménard, and F.X. Demoulin. Large eddy simulation of liquid jet atomization. *Atomization and Sprays*, 21(9):711–736, 2011.
- [19] V. Cleary, P. Bowen, and H. Witlox. Flashing liquid jets and two-phase droplet dispersion I. Experiments for derivation of droplet atomization correlations. *Journal of Hazardous Materials*, 142:786–796, 2007.
- [20] B. Cockburn, S. Hou, and C.-W. Shu. TVB Runge-Kutta local projection discontinuous Galerkin finite element method for conservation laws II: General framework. *Mathematics of Computation*, 52(186):411–435, 1989.
- [21] B. Cockburn, S. Hou, and C.-W. Shu. The Runge-Kutta local projection discontinuous Galerkin finite element method for conservation laws IV: The multidimensional case. *Mathematics of Computation*, 54(190):545–581, 1990.

- [22] B. Cockburn, S.-Y. Lin, and C.-W. Shu. TVB Runge-Kutta local projection discontinuous Galerkin finite element method for conservation laws III: One-dimensional systems. *Journal of Computational Physics*, 84:90–113, 1989.
- [23] B. Cockburn and C.-W. Shu. The Runge-Kutta local projection p^1 -discontinuous Galerkin finite element method for scalar conservation laws. *M²AN*, 25(3):337–361, 1991.
- [24] B. Cockburn and C.-W. Shu. The Runge-Kutta local projection discontinuous Galerkin finite element method for conservation laws V: Multidimensional systems. *Journal of Computational Physics*, 141:199–224, 1998.
- [25] R. Courant, K. Friedrichs, and H. Lewy. Über die partiellen Differenzgleichungen der mathematischen Physik. *Mathematische Annalen*, 100(1):32–74, 1928.
- [26] D. Dietzel, T. Hitz, C.-D. Munz, and A. Kronenburg. Numerical simulation of the growth and interaction of vapour bubbles in superheated liquid jets. *International Journal of Multiphase Flows*, 121:103112, 2019.
- [27] D. Dietzel, T. Hitz, C.-D. Munz, and A. Kronenburg. Single vapour bubble growth under flash boiling conditions using a modified HLLC Riemann solver. *International Journal of Multiphase Flows*, 116:250–269, 2019.
- [28] P. Downar-Zapolski, Z. Bilicki, L. Bolle, and J. Franco. The non-equilibrium relaxation model for one-dimensional flashing liquid flow. *International Journal of Multiphase Flows*, 22(3):473–483, 1996.
- [29] R.Q. Duan, S.Y. Jiang, S. Koshizuka, Y. Oka, and A. Yamaguchi. Direct simulation of flashing liquid jets using the MPS method. *International Journal of Heat and Mass Transfer*, 49:402–205, 2006.
- [30] R.Q. Duan, S. Koshizuka, S.Y. Jiang, Y. Oka, A. Yamaguchi, and T. Takata. Numerical analyses of flashing jet structure and droplet size characteristics. *Journal of Nuclear Science and Technology*, 43(3):285–294, 2006.
- [31] I.W. Eames, N.J. Marr, and H. Sabir. The evaporation coefficient of water: A review. *International Journal of Heat and Mass Transfer*, 40(13):2963–2973, 1997.

- [32] S. Fechter. *Compressible multi-phase simulations at extreme conditions using a discontinuous Galerkin scheme*. PhD thesis, Universität Stuttgart, 2015.
- [33] S. Fechter, F. Jaegle, and V. Schleper. Exact and approximate Riemann solvers at phase boundaries. *Computers & Fluids*, 75:112–126, 2013.
- [34] S. Fechter and C.-D. Munz. A discontinuous Galerkin-based sharp-interface method to simulate three-dimensional compressible two-phase flow. *International Journal of Numerical Methods in Fluids*, 78:413–435, 2015.
- [35] S. Fechter, C.-D. Munz, C. Rohde, and C. Zeiler. A sharp interface method for compressible liquid-vapor flow with phase transition and surface tension. *Journal of Computational Physics*, 336:347–374, 2017.
- [36] S. Fechter, C.-D. Munz, C. Rohde, and C. Zeiler. Approximate Riemann solver for compressible liquid vapor flow with phase transition and surface tension. *Computers & Fluids*, 169:169–185, 2018.
- [37] F. Föll, T. Hitz, C. Müller, C.-D. Munz, and M. Dumbser. On the use of tabulated equations of state for multi-phase simulations in the homogeneous equilibrium limit. *Shock Waves*, 29:769–783, 2019.
- [38] U. Fritsching. Spray systems. In C.T. Crowe, editor, *Multiphase Flow Handbook*, pages 8.1 – 8.100. CRC Press, Taylor & Francis Group, Boca Raton, 2006.
- [39] J.W. Gärtner. Evaluation of a single-equation model for the numerical simulation of flash boiling in OpenFOAM. Master’s thesis, Universität Stuttgart, 2018.
- [40] T. Gemci, K. Yakut, N. Chigier, and T.C. Ho. Experimental study of flash atomization of binary hydrocarbon liquids. *International Journal of Multiphase Flow*, 30:395–417, 2004.
- [41] S. Gopalakrishnan. *Modeling of thermal non-equilibrium in superheated injector flows*. PhD thesis, University of Massachusetts, 2010.
- [42] A. Günther and K.-E. Wirth. Evaporation phenomena in superheated atomization and its impact on the generated spray. *International Journal of Heat and Mass Transfer*, 64:952–956, 2013.

- [43] A. Harten, P.D. Lax, and B. van Leer. On upstream differencing and Godunov-type schemes for hyperbolic conservation laws. *Society for Industrial and Applied Mathematics*, 25(1):35–61, 1983.
- [44] H. Hertz. Ueber die Verdunstung der Flüssigkeiten, insbesondere des Quecksilbers, im luftleeren raume. *Annalen der Physik und Chemie*, 253:177–193, 1882.
- [45] F. Hindenlang. *Mesh curving techniques for high order parallel simulations on unstructured meshes*. PhD thesis, Universität Stuttgart, 2014.
- [46] F. Hindenlang, G.J. Gassner, C. Altmann, A. Beck, M. Staudenmaier, and C.-D. Munz. Explicit discontinuous Galerkin methods for unsteady problems. *Computers & Fluids*, 61:86–93, 2012.
- [47] C.W. Hirt and B.D. Nichols. Volume of fluid (VOF) methods for the dynamics of free boundaries. *Journal of Computational Physics*, 39:201–225, 1981.
- [48] R.W. Houim and K.K. Kuo. A ghost fluid method for compressible reacting flows with phase change. *Journal of Computational Physics*, 85:865–900, 2013.
- [49] X.Y. Hu, N.A. Adams, and G. Iaccarino. On the HLLC Riemann solver for interface interaction in compressible multi-fluid flow. *Journal of Computational Physics*, 228:6572–6589, 2009.
- [50] M. Ishii and T. Hibiki. *Thermo-fluid dynamics for two-phase flow*. Springer, 2011.
- [51] I.K. Karathanassis, P. Koukouvinis, and M. Gavaises. Comparative evaluation of phase-change mechanisms for the prediction of flashing flows. *International Journal of Multiphase Flows*, 95:257–270, 2017.
- [52] D. Kawano, H. Ishii, H. Suzuki, Y. Goto, M. Odaka, and J. Senda. Numerical study on flash-boiling spray of multicomponent fuel. *Heat Transfer - Asian Research*, 35(5):369–385, 2006.
- [53] Y. Kitamura, H. Morimitsu, and T. Takahashi. Critical superheat for flashing of superheated liquid jets. *Industrial & Engineering Chemistry Fundamentals*, 25:206–211, 1986.
- [54] M. Knudsen. Die maximale Verdampfungsgeschwindigkeit des Quecksilbers. *Die Annalen der Physik*, 353(13):697–708, 1915.

-
- [55] M. Knudsen. *Kinetic theory of gases*. London Methuen, 1950.
- [56] D.A. Kopriva. *Implementing spectral methods for partial differential equations*. Springer Science + Business Media B.V., 2009.
- [57] C. Kunkelmann. *Numerical modeling and investigation of boiling phenomena*. PhD thesis, Technische Universität Darmstadt, 2011.
- [58] G. Lamanna, H. Kamoun, B. Weigand, C. Manfretti, A. Rees, J. Sender, M. Oswald, and J. Steelant. Flashing behavior of rocket engine propellants. *Atomization and Sprays*, 25(10):837–856, 2015.
- [59] G. Lamanna, H. Kamoun, B. Weigand, and J. Steelant. Towards a unified treatment of fully flashing sprays. *International Journal of Multiphase Flow*, 58:168–184, 2014.
- [60] E. Lauer, X.Y. Hu, S. Hickel, and N.A. Adams. Numerical modelling and investigation of symmetric and asymmetric cavitation bubble dynamics. *Computers & Fluids*, 69:1–19, 2012.
- [61] R. Lebas, T. Menard, P.A. Beau, A. Berlemont, and F.X. Demoulin. Numerical simulation of primary break-up and atomization: DNS and modelling study. *International Journal of Multiphase Flow*, 35(3):247–260, 2009.
- [62] H.S. Lee and Jr H. Merte. Spherical vapor bubble growth in uniformly superheated liquids. *International Journal of Heat and Mass Transfer*, 39:2427–2447, 1996.
- [63] J. Lee, R. Madabhushi, C. Fotache, S. Gopalakrishnan, and D.P. Schmidt. Flashing flow of superheated jet fuel. *Proceedings of the Combustion Institute*, 32:3215–3222, 2009.
- [64] J. Lee and G. Son. A sharp-interface level-set method for compressible bubble growth with phase change. *International Communications in Heat and Mass Transfer*, 86:1–11, 2017.
- [65] K.G. Lyras, S. Dembele, and J.X. Wen. Numerical simulation of flashing jets atomisation using a unified approach. *International Journal of Multiphase Flows*, 113:45–58, 2019.

- [66] L. Ma and D. Roekaerts. Modeling of spray jet flame under MILD condition with non-adiabatic FGM and a new conditional droplet injection model. *Combustion & Flame*, 165:402–423, 2016.
- [67] C. Manfretti. Laser ignition of an experimental cryogenic reaction and control thruster: Pre-ignition conditions. *Journal of Propulsion and Power*, 30(4):925–933, 2014.
- [68] O. Le Métayer and R. Saurel. The Noble-Able stiffened-gas equation of state. *Physics of Fluids*, 28(046102):1–23, 2016.
- [69] B.B. Mikic, W.M. Rohsenow, and P. Griffith. On bubble growth rates. *International Journal of Heat and Mass Transfer*, 13(4):657–666, 1970.
- [70] S. Navarro-Martinez. Large eddy simulation of spray atomization with a probability density function method. *International Journal of Multiphase Flow*, 63:11 – 22, 2014.
- [71] K.D. Neroorkar. *Modeling of flash boiling flows in injectors with gasoline-ethanol fuel blends*. PhD thesis, University of Massachusetts, 2011.
- [72] D.W. Oxtoby and R. Evans. Nonclassical nucleation theory for the gas-liquid transition. *Journal of Chemical Physics*, 89(12):7521–7530, 1988.
- [73] R.D. Oza. On the mechanism of flashing injection of initially subcooled fuels. *Journal of Fluids Engineering*, 106:105–109, 1984.
- [74] B.S. Park and S.Y. Lee. An experimental investigation of the flash atomization mechanism. *Atomization & Sprays*, 4:159–179, 1994.
- [75] J.N. Pelton, S. Madry, and S. Camacho-Lara. Satellite application handbook: The complete guide to satellite communications, remote sensing navigation, and meteorology. In J.N. Pelton, S. Madry, and S. Camacho-Lara, editors, *Handbook of Satellite Application*, pages 3–19. Springer International Publishing Switzerland, New York, 2017.
- [76] A.H. Persad and C.A. Ward. Expressions for the evaporation and condensation coefficients in the Hertz-Knudsen relation. *Chemical Reviews*, 116:7727–7767, 2016.

-
- [77] P.-O. Persson and J. Peraire. Sub-cell shock capturing for discontinuous Galerkin methods. In *Proceedings of the 44th AIAA Aerospace Sciences Meeting and Exhibit*.
- [78] M.S. Plesset. The dynamics of cavitation bubbles. *Journal of Applied Mechanics*, 16:277–282, 1949.
- [79] M.S. Plesset and A. Prosperetti. Bubble dynamics and cavitation. *Annual Review of Fluid Mechanics*, 9:145–185, 1977.
- [80] M.S. Plesset and S.A. Zwick. The growth of vapor bubbles in superheated liquids. *Journal of Applied Physics*, 25(4):493–500, 1954.
- [81] A. Prosperetti. Vapor bubbles. *Annual Review of Fluid Mechanics*, 49:221–248, 2017.
- [82] A. Prosperetti and M.S. Plesset. Vapour-bubble growth in a superheated liquid. *Journal of Fluid Mechanics*, 85:349–368, 1978.
- [83] S.K. Rachakonda, Y. Wang, and D.P. Schmidt. Flash-boiling initialization for spray simulations based on parametric studies. *Atomization and Sprays*, 28(2):111–140, 2018.
- [84] T. H. Ramcke. *Simulation der Flash-Verdampfung bei der kryogenen Einspritzung von in-Orbit Raketentriebwerken*. PhD thesis, Universität der Bundeswehr München, 2017.
- [85] L. Rayleigh. On the pressure developed in a liquid during the collapse of a spherical cavity. *Philosophical Magazine and Journal of Science*, 34:94–98, 1917.
- [86] W.H. Reed and T.R. Hill. Triangular mesh methods for then the neutron transport equation. (LA-UR-73-479), 1973.
- [87] R.D. Reitz. A photographic study of flash-boiling atomization. *Aerosol Science and Technology*, 12:561–569, 1990.
- [88] M. Reocreux. *Contribution à l'étude des débits critiques en écoulement diphasique eau-vapeur*. PhD thesis, Université Scientifique et Médicale de Grenoble, 1974.

-
- [89] W. Rider and T. Kothe. Reconstructing volume tracking. *Journal of Computational Physics*, 141:112–152, 1998.
- [90] A.J. Robinson and R.L. Judd. The dynamics of spherical bubble growth. *International Journal of Heat and Mass Transfer*, 47:5101–5113, 2004.
- [91] P.L. Roe. Approximate Riemann solvers, parameter vectors and difference schemes. *Journal of Computational Physics*, 43:357–372, 1981.
- [92] K. Saha, S. Som, M. Battistoni, Y. Li, S. Quan, and P.K. Senecal. Modelling of internal and near-nozzle flow for a gasoline direct injection fuel injector. *Journal of Engineering for Gas Turbines and Power*, 136(092603):1–10, 2014.
- [93] R. Saurel, P. Boivin, and O. Le Metayer. A general formulation for cavitating, boiling and evaporating flows. *Computers & Fluids*, 128:53–64, 2016.
- [94] R. Saurel, F. Petitpas, and R. Abgrall. Modelling phase transition in metastable liquids: Application to cavitating and flashing flows. *Journal of Fluid Mechanics*, 607:313–350, 2008.
- [95] S.S. Sazhin. *Droplets and sprays*. Springer, 2014.
- [96] J. Schlottke and B. Weigand. Direct numerical simulation of evaporating droplets. *Journal of Computational Physics*, 227:5215–5237, 2008.
- [97] D.P. Schmidt, M.L. Corradini, and C.J. Rutland. A two-dimensional, non-equilibrium model of flashing nozzle flow. In *3rd ASME/JSME Joint Fluids Engineering Conference*, 1999.
- [98] D.P. Schmidt, S. Gopalakrishnan, and H. Jasak. Multi-dimensional simulation of thermal non-equilibrium channel flow. *International Journal of Multiphase Flow*, 36:284–292, 2010.
- [99] R.W. Schrage. *A theoretical study of interphase mass transfer*. Columbia University Press, New York, 1953.
- [100] J. Senda, Y. Hojyo, and H. Fojimoto. On the pressure developed in a liquid during the collapse of a spherical cavity. *JSAE Review*, 15:291–296, 1994.
- [101] P.K. Senecal, D.P. Schmidt, I. Nouar, C.J. Rutland, R.D. Reitz, and M.L. Corradini. Modeling high-speed viscous liquid sheet atomization. *International Journal of Multiphase Flow*, 25(6):1073–1097, 1999.

- [102] E. Sher, T. Bar-Kohany, and A. Rashkovan. Flash-boiling atomization. *Progress in Energy and Combustion Science*, 34:417–439, 2008.
- [103] E. Sher and C. Elata. Spray formation from pressure cans by flashing. *Ind. Eng. Chem., Process Des. Dev.*, 16(2):237–242, 1977.
- [104] M. Shusser, T. Ytrehus, and D. Weihs. Kinetic theory analysis of explosive boiling of liquid droplet. *Fluid Dynamics Research*, 27:353–365, 2000.
- [105] M. Sonntag. *Shape derivatives and shock capturing for the Navier-Stokes equations in discontinuous Galerkin methods*. PhD thesis, Universität Stuttgart, 2017.
- [106] M. Sonntag and C.-D. Munz. Shock capturing for discontinuous Galerkin methods using finite volume subcells. In J. Fuhrmann, M. Ohlberger, and C. Rohde, editors, *Finite Volumes for Complex Applications VII-Elliptic, Parabolic and Hyperbolic Problems*, pages 945–953, Cham, 2014. Springer International Publishing.
- [107] M. Sussman, P. Smereka, and S. Osher. A level set approach for computing solutions to incompressible two-phase flow. *Journal of Computational Physics*, 114:146–159, 1994.
- [108] N. Tanaka, K. Furukawa, S. Suemori, T. Matsuo, M. Nishida, and A. Yasutake. The greening of spacecraft reaction control systems. *Mitsubishi Heavy Industries Technical Review*, 48(4):44–50, 2011.
- [109] T.G. Theofanous and P.D. Patel. Universal relations for bubble growth. *International Journal of Heat and Mass Transfer*, 19(4):425–429, 1976.
- [110] A.S. Thompson and S.D. Heister. Flashing behavior of rocket engine propellants. *Atomization and Sprays*, 26(7):633–658, 2016.
- [111] E.F. Toro. *Riemann solvers and numerical methods for fluid dynamics*. Springer-Verlag Berlin Heidelberg, 2009.
- [112] A. Vallet and R. Borghi. Modélisation eulerienne de l’atomisation d’un jet liquide. *Comptes Rendus de l’Académie des Sciences - Series IIB - Mechanics-Physics-Astronomy*, 327(10):1015 – 1020, 1999.
- [113] A. Vallet, A.A. Burluka, and R. Borghi. Development of a Eulerian model for the atomization of a liquid jet. *Atomization and Sprays*, 11(6), 2001.

-
- [114] H.K. Versteeg and W. Malalasekera. *An introduction to computational fluid dynamics - The finite volume method*. Pearson Education Limited, 2007.
- [115] D. Weber. *Flash Boiling bei Ottomotoren mit Benzindirekteinspritzung: Experimentelle Untersuchung, Modellierung und numerische Simulation*. PhD thesis, Technische Universität Darmstadt, 2016.
- [116] J.H. Williamson. Low-storage Runge-Kutta schemes. *Journal of Computational Physics*, 35:48–56, 1980.
- [117] H. Witlox, M. Harper, P. Bowen, and V. Cleary. Flashing liquid jets and two-phase droplet dispersion II. Comparison and validation of droplet size and rainout formulations. *Journal of Hazardous Materials*, 142:797–809, 2007.
- [118] R. Huang G. Hong Y. Huang, S. Huang. Explicit discontinuous Galerkin methods for unsteady problems. *Energy Conversion and Management*, 108:68–77, 2016.
- [119] G.H. Yeoh and J. Tu. *Computational techniques for multi-phase flows*. Elsevier Ltd., 2010.
- [120] A. Zein, M. Hantke, and G. Warnecke. Modeling phase transition for compressible two-phase flows applied to metastable liquids. *Journal of Computational Physics*, 229:2964–2998, 2010.
- [121] Y. Zeng and C.-F. F. Lee. An atomization model for flash boiling sprays. *Combustion Science and Technology*, 165(1):45–67, 2001.
- [122] B. Zuo, A.M. Gomes, and C.J. Rutland. Modelling superheated fuel sprays and vaporization. *International Journal of Engine Research*, 1(4):321–336, 2000.

List of Figures

2.1	Vapour pressure diagram for different regimes.	6
2.2	Principal sketch for liquid jets injected into gas atmosphere.	9
2.3	Simplified setup for a flash boiling jet. A sub-cooled liquid (state A) will be injected into a low-pressure environment (state D). The liquid will expand to a superheated state B allowing for spontaneous bubble nucleation at state C.	11
2.4	Photographies of the jet disintegration of water jets for different regimes taken from Kitamura et al. [53].	12
2.5	Different flow modes for flash boiling, according to [15, 73, 74, 102].	13
2.6	The volume fraction α represents the relative amount of liquid in a computational cell.	16
3.1	Aspects of the sub-grid scale heat flux model.	30
4.1	Discretization of a one-dimensional domain by DG cells with a sub-cell resolution defined by a third order polynomial.	39
4.2	The extrapolation of the physical state U from the left and right cell to the common face yields the different states U^L and U^R , respectively.	43
4.3	Discretization of a one-dimensional domain in the DG cells and a sub-cell resolution defined by a third order polynomial. Cells in the vicinity of the liquid-vapour interface are treated as FV cells.	45
4.4	Riemann wave fan for the HLLC approximation according to Toro [111].	49
4.5	Riemann wave fans for two-phase problems with phase transition. Adapted from [36].	51
5.1	Configuration of a shock tube test case with one open end.	58
5.2	Solid lines: initial conditions of the shock tube. Dashed lines: results after $t = 0.2$ ms.	60

5.3	Solid line: initial temperature field of the shock tube. Dashed lines: temperature after $t = 5.0$ ms.	61
5.4	Pressure wave propagation in the liquid phase.	61
5.5	Results for the shock tube when a considerable amount of mass has vaporised.	63
5.6	Mass flux over time for the shock tube test case.	64
5.7	Mass flux over time for shock tube.	64
5.8	Initial conditions for the present setup. State B indicates a metastable superheated liquid. State C indicates a vapour bubble which nucleates within the liquid. We assume an isothermal nucleation with the vapour bubble being saturated. The resulting pressure gap is balanced by the surface tension.	66
5.9	Bubble radius over time for different temperatures	70
5.10	Thickness and resolution of the boundary layer for different temperatures and $R_p = 100$	70
5.11	Bubble radius and boundary resolution for case C100-120 using different mesh resolutions.	72
5.12	Bubble radius for different mesh resolutions without initial delay.	73
5.13	Dimensionless bubble radius over time for different combinations of T_0 and R_p , respectively. The dashed line defines the analytical solution in the inertia controlled range. The dash-dotted line indicates the analytical solution in the heat diffusion controlled range.	74
5.14	Reference solution for case C100-90 with (solid lines) and without (dashed-lines) coupling of the temperature equation 5.6. Black lines show the dimensionless radius R^+ and blue lines show the instantaneous mass flux.	75
5.15	Results obtained from the RPE coupled to the temperature equation for different temperatures (colours) at $R_p = 5$	76
5.16	The black, red and yellow lines show the bubble pressure, the surface tension and the viscous terms in the Rayleigh-Plesset equation for C5-120. The blue line represents the liquid pressure at the bubble wall defined by Eq. (5.12)	77
5.17	Geometrical setup for single bubble growth.	79
5.18	Results of C5-120 with different domain sizes ($L/2, L, 2L$) for $N_{\text{bub}} = 10$	81
5.19	Results of C5-120 with different bubble resolutions N_{bub} and with $CFL = 0.45$ using the domain size L	82

5.20	Results of C5-120 with different bubble resolutions N_{bub} for $L = L_2$.	83
5.21	Pressure fields of C5-120 with $R_0^* = 50$ with different initial conditions for the pressure field.	84
5.22	Interface velocity for C5-120 and $R_0^* = 50$ with different initial conditions for the pressure.	84
5.23	Comparison between CoolProp data and NASG approximation for the vapour phase at three different pressures.	86
5.24	Comparison between CoolProp data and NASG approximation for the liquid phase at three different pressures.	87
5.25	Results of C5-90 with different EOS approximations.	87
5.26	Results of C5-120 with different EOS approximations.	88
5.27	Normalized bubble radius R^* over time for C5-120 with $R_0^* = 50$. The DG simulation with the 1D solver (black line) and the 3D solver (blue crosses) match the reference solution (red line).	88
5.28	Three-dimensional representation of the bubble growth.	89
5.29	Mass and energy conservation.	90
6.1	Normalized bubble radius R^* over time of case C5-120 with $R_0^* = 50$.	93
6.2	Vaporisation mass flux \dot{m}'' of case C5-120 with $R_0^* = 50$.	93
6.3	Pressure field of C5-120 and $R_0^* = 50$ at different time steps.	94
6.4	Integrated quantities of C5-120 and $R_0^* = 50$.	94
6.5	Normalized bubble radius R^* over time for different length scales.	95
6.6	Total vaporised mass and volume change of C5-120 for different R_0^* .	95
6.7	Volumetric expansion for $R_0^* = 50$ under different physical conditions.	96
6.8	Comparison of HKR, KR and SHFM for case C5-120 and $R_0^* = 50$.	97
6.9	Vaporisation coefficients λ_{vap} as a function of different characteristic quantities of the investigation.	100
6.10	Comparison of estimated and calibrated λ_{vap} .	101
6.11	Vaporisation mass fluxes from the RPE normalized by the vapour density and the factor A in Eq. (5.8) as a function of the dimensionless time t^+ . After an initial transient the curves for all cases approximately converge to a single curve.	102
6.12	Sensitivity of the bubble radius to a 10% change in the model coefficient. All cases use $R_0^* = 50$.	103
6.13	Influence of the numerical setup (mesh and time resolution, initial pressure) to the calibrated coefficients of the HKR.	104

7.1	Ratio between final jet volume and initial jet volume according to Eq. (7.3). If the bubble distance is large compared to the initial radius, i.e. Ψ_{bub} is large, then the early stages of bubble growth do not contribute to the expansion of the liquid jet.	107
7.2	Different geometrical setups for the investigation of multiple bubble growth in superheated liquids. The fluid states B, C and D are labelled according to Fig. 2.3.	108
7.3	Contour plots of the bubble column test case for three different time steps with five bubble rows along the x-direction. The left plane and right plane show the time averaged pressure field and the density field, respectively. The blue coloured iso-surfaces indicate the interfaces between bubbles and superheated liquid.	111
7.4	Mass flux and density contours of the outermost (top) and innermost (bottom) bubble for case C5-120 with $R_0^* = 50$ at $t = 0.5 \mu\text{s}$	111
7.5	Normalised bubble radius as a function of the distance to surface.	112
7.6	Dimensionless bubble radii for different geometries using C5-120 with $R_0^* = 50$. The black, blue and red symbols represent the numerical data for Setup 1, Setup 2 and Setup 3, respectively. The solid lines show the corresponding exponential fits.	112
7.7	Dimensionless bubble radii for different numbers of bubbles rows using C5-120, $R_0^* = 50$ and Setup 1 at $t = 0.5 \mu\text{s}$	113
7.8	Setup 2, C5-120, $R_0^* = 50$: Comparison of the bubble radii to those of a single bubble.	115
7.9	Dimensionless volume of cylindrical jet according to Eq. (7.3) with $R^* = f(t)$ given by single bubble growth rates (black line) and by Eq. (7.7).	116
7.10	Setup 2, C5-120, $R_0^* = 50$: Comparison of the bubble growth rates to those of a single bubble.	117
7.11	Setup 2, $R_p = 5$, $R_0^* = 50$: Normalised change of the radius and normalised growth rates.	118
7.12	Reduced bubble radii.	119
7.13	Setup 2: Normalised mass flux for different cases.	119
7.14	Comparison of bubble radii from the multiple bubble DNS to the Rayleigh-Plesset equation solved with a time dependend pressure field.	121
7.15	Setup 2, Normalised mass flux as a function of a normalised local pressure difference.	122

7.16	Bubble growth rate normalised by the bubble parameter $A = \sqrt{\frac{2}{3} \frac{h_{fg} \rho_{\text{vap}} (T_{\infty} - T_{\text{sat}})}{\rho_{\text{liq}} T_{\text{sat}}}}$ as a function of a normalised pressure difference. . .	123
5.1	Vaporisation coefficients c_{ent} as a function of different characteristic quantities of our investigation.	145
5.2	Vaporisation coefficients C_{δ} as a function of different characteristic quantities of our investigation.	146

List of Tables

5.1	Initial conditions for the shock tube test case.	58
5.2	Default numerical parameters and physical models for the shock tube test case.	59
5.3	Initial conditions for bubble growth parametric study. Densities are given in [kg/m ³], pressures are given in [bar], critical radii in [μ m] and temperatures in [K]. The Jakob number Ja is dimensionless.	68
5.4	Default numerical and geometrical parameters as well as physical models for single bubble test case C5-120 with $R_0^* = 50$	79
5.5	Relative computational time for different R_0^* in percent.	80
5.6	Parameters for domain size sensitivity study. The default length L is given by Eq. (5.14).	81
5.7	Parameters for cell size sensitivity study.	81
5.8	Coefficients for the NASG-EOS given in Eqs. (3.25)-(3.28).	85
7.1	Geometrical and numerical parameters.	109
4.1	λ_{vap} for $R_p = 5$ and $R_p = 10$	141
4.2	λ_{vap} for $R_p = 50$ and $R_p = 100$	141
4.3	c_{ent} for $R_p = 5$ and $R_p = 10$	142
4.4	c_{ent} for $R_p = 50$ and $R_p = 100$	142
4.5	C_δ for $R_p = 5$ and $R_p = 10$	142
4.6	C_δ for $R_p = 50$ and $R_p = 100$	142
7.1	Case and code used to produce results of paper on single bubble growth by Dietzel et al. [27]. The main directory on the data storage is <code>ITV-PUBLICATIONS/GIT/2019_Dietzel_IJMF/Rayleigh-Plesset-Data</code> . The corresponding code repository is <code>GITLAB/itv-mitarbeiter/Dietzel/rayleigh-plesset</code>	149

7.2	Case and code used to produce results of paper on single bubble growth by Dietzel et al. [27]. The main directory on the data storage is <code>ITV-PUBLICATIONS/GIT/2019_Dietzel_IJMF/DG-Data</code> . The corresponding code repository is <code>GITLAB/TwoPhaseDG/StruktiTwoPhase</code>	150
7.3	Case and code used to produce results of paper on single bubble growth by Dietzel et al. [27]. The main directory on the data storage is <code>ITV-PUBLICATIONS/GIT/2019_Dietzel_IJMF/DG-Data</code> . The corresponding code repository is <code>GITLAB/TwoPhaseDG/ILASS17Flexi</code>	150
7.4	The following codes are generally used for pre- and postprocessing of the 3D simulations	151
7.5	Case and code used to produce results of paper on multiple bubble growth. Here, cases of the bubble column are considered. The main directory on the data storage is <code>ITV-PUBLICATIONS/GIT/2019_Dietzel_IJMF-2/DG-Data/bubble_column</code> . The corresponding code repository is <code>GITLAB/TwoPhaseDG/ILASS17Flexi</code>	151
7.6	Case and code used to produce results of paper on multiple bubble growth. Here, cases of the jet slice are considered. The main directory on the data storage is <code>ITV-PUBLICATIONS/GIT/2019_Dietzel_IJMF-2/DG-Data/jet_slice</code> . The corresponding code repository is <code>GITLAB/TwoPhaseDG/ILASS17Flexi</code>	152